School of Applied Chemistry

The Mechanism of Gibbsite Crystal Growth in Bayer Liquor

Mei-yin Lee

This thesis is presented as part requirement for
the award of the Degree of Doctor of Philosophy
of the
Curtin University of Technology

April 1998

Pooh knew what he meant, but, being a Bear of Very Little Brain,

couldn't think of the words

TheHouse at Pooh Corner

A. A. Milne

To my family Kim, Mary, Su and Ken.

Eeyore was saying to himself.

"This writing business. Pencils and what-not. Over-rated, if you ask me. Silly stuff.

Nothing in it."

Winnie-the-Pooh

A. A. Milne

ACKNOWLEDGMENT

First I would like to acknowledge the guidance of my supervisors. To Professor Gordon Parkinson for his continual encouragement, advice, patience and support, and to Dr Andrew Rohl for his advice and guidance, especially in molecular modelling. To Dr Frank Lincoln, thank you for the encouragement and advice during the initial stages of my PhD.

Special thanks also goes to Dr Katsuo Tsukamoto for his expertise in rapid dynamic light scattering and also for his hospitality during my visit to Japan. To those involved in AMIRA project P380A - Module 2/3, Dr Helen Watling and Dr Peter Smith from CSIRO Division of Minerals and representatives of my industrial sponsors, Drs Steven Rosenberg and Stephen Grocott, thank you for the helpful discussions.

I gratefully acknowledge the staff and students of Centre of Microscopy and Microanalyses and CSIRO Division of Minerals for all their help and the use of their facilities.

I would like to thank AMIRA, AJ Parker CRC for Hydrometallurgy and SRCAMMP who supported me financially with scholarships during this period.

Appreciation of support also goes to the members of the Crystallization group. It was nurturing environment working with a group with such high levels of expertise and enthusiasm. To Dr Tony McKinnon, for "inviting" me to share his office, proof reading and all the helpful advice.

Finally, I would like to thank Richard Hecker, for his continuous pats during these trying times, as well as, for those Tim Tams and coffees.

ABSTRACT

Although the precipitation of aluminium trihydroxide as gibbsite, via the Bayer process has been widely studied, the mechanism of crystal growth is poorly understood. This work focus on the morphology of gibbsite and the relative growth rates of individual crystal faces.

Initial work was carried out to characterize aluminium trihydroxide and it was found that bayerite, another polymorph, precipitated at temperatures below 50°C and its morphology depended on the method of precipitation. Gibbsite however, precipitated above this temperature and its morphology depended on the type of alkali aluminate solutions used. The method of precipitation does not affect the morphology, only the size of the precipitate formed. The morphology of gibbsite can be altered by the addition of organic compounds which are known to inhibit gibbsite precipitation. Some of these compounds were found to selectively inhibit the growth of individual crystal faces, thus altering the overall morphology of gibbsite. Boehmite, a polymorph of aluminium hydroxide, can be produced by partial dehydration of gibbsite at 300°C. The morphology of boehmite consisted of diamond shaped crystals.

The influence of cation incorporation on the morphology of gibbsite was studied experimentally and computationally (molecular modelling). These studies showed that there is a linear relationship between the amount of cation incorporated and atomic radii and between the amount of cation incorporated and the defect energy calculated. The equilibrium morphology of gibbsite predicted in the absence of media matched the morphology of gibbsite grown slowly from sodium aluminate, implying that the amount of sodium incorporation is low in these crystals.

The growth rates of individual crystal faces were measured *in situ*, and found to be a function of supersaturation squared for the prismatic faces, possibly indicating that

growth occurs by spiral growth mechanism. The growth of the basal face was found to follow the spiral growth mechanism below a relative supersaturation of 0.815 and the birth and spread mechanism above this level. The activation energies and kinetic coefficients for the individual prismatic faces were also determined.

Growth rate dispersion was observed in these microscopic studies, but the question of size dependency remains unanswered.

The overall growth rates of gibbsite crystal, determined using rapid dynamic light scattering, was found to be an exponential function of supersaturation indicative of a birth and spread growth mechanism.

TABLE OF CONTENT

CHAPTER 1: INTRODUCTION

CHAPTER 3 : THE MORPHOLOGY OF GIBBSITE

CHAPTER 5 : THE GROWTH RATE OF GIBBSITE

LIST OF FIGURES

Chapter 1: Introduction

Chapter 2: Characterization of Aluminium Trihydroxide

Chapter 3: The Morphology of Gibbsite

Chapter 4: Assessment of Various Techniques for the Study of Crystal Growth

Chapter 5: The Growth Rate of Gibbsite

LIST OF TABLES

Chapter 5: The Growth Rate of Gibbsite

TERMINOLOGY

Following the North American alumina industry terminologies, the aluminate solution compositions are expressed as follows:

- Aluminium concentration (A), as g/L Al_2O_3
- Sodium hydroxide or caustic concentration (C) expressed as g/L Na_2CO_3
- Total alkali concentration (S) expressed as g/L Na_2CO_3
- A/C refers to the alumina to caustic ratio

A typical solution composition for green liquor is given in Table A expressed using the North American alumina industry nomenclature, and in Table B expressed in molarities.

Table A: Green Liquor Composition (g/L)

	A	C	S	A/C
Green Liquor	120-150	180-220	220 - 260	0.600 - 0.750

Table B: Green Liquor Composition (M)

	Al	NaOH	Na_2CO_3
Green Liquor	1.2 - 1.5	3.4 - 4.2	0.4 - 0.8

The relative supersaturation of aluminate solutions, σ, may be defined using Equation I From this, it can be seen that at constant caustic concentration and temperature, the *A/C* ratio may be used as an indicator of the level of supersaturation.

$$\sigma = \frac{A/C - (A/C)^*}{(A/C)^*} \qquad \text{(I)}$$

where A = *Aluminium concentration as g/L* Al_2O_3

C = *Sodium hydroxide concentration as g/L* Na_2CO_3

A^* = *Equilibrium aluminium concentration as g/L* Al_2O_3

C^* = *Equilibrium sodium hydroxide concentration as g/L* Na_2CO_3

Chapter 1

Introduction

1.1. Aluminium and its Industry in Australia

Aluminium is the most abundant metallic element in the Earth's crust and is found in many common minerals, with bauxite ($AlO_x(OH)_{3-2x}$, ($0 \leq x \leq 1$)) being the most important commercially. Bauxite, first discovered in 1821 and named after the French district *Les Baux* can be found in all the continents in the world, with the largest economic resource found in Australia. The main minerals in bauxite are gibbsite ($Al(OH)_3$) and two polymorphs of AlOOH; boehmite and diaspore, with bauxite ore referring to bauxite that contains high levels of aluminium species, and sufficiently low levels of iron oxides and silica to be economically viable (A.C.T.E.D. Chemicals in Australia, 1997).

The development of the Australian aluminium export industry is mainly due to the discovery of large reserves of bauxite ore in Western Australia and Queensland during the 1950s. With accessible raw materials, large and low cost energy resources and low infrastructure cost, processing low alumina content (30 - 40% as Al_2O_3) and high organic content bauxite became economically viable. In 1995, Australia mined 42 million tonnes of bauxite to produce 12 million tonnes of alumina, of which Western Australia produced 8 million tonnes of alumina valued at approximately 2 billion dollars, representing over 25% of world production. Australia produces about 40% of world bauxite and over 35% of world alumina, making it the largest producer of bauxite and alumina (A.C.T.E.D. Chemicals in Australia, 1997).

1.2. The Bayer Process

Bauxite is now almost universally treated by the Bayer process, introduced by Karl Bayer in 1888, to obtain alumina. The process is based on the dissolution of aluminium bearing material in highly caustic conditions and its precipitation as

gibbsite, and can be described by a simple equilibrium reaction (1). Gibbsite is one of the three polymorphs of aluminium hydroxide (see Section 1.2.4) (Wefers and Misra, 1987).

$$Al(OH)_3 + OH^- \xleftrightarrow{NaOH} Al(OH)_4^- \qquad (1)$$

The Bayer process (Figure 1.1) is a continuous process which may be separated into four simple steps : hydrothermal digestion, where the bauxite is heated in hot caustic soda solutions to dissolve the aluminium bearing minerals; clarification, where separation of the aluminium-rich solutions and undissolved components of bauxite (red mud) occurs; crystallization, where recovery of aluminium occurs as gibbsite; and calcination, where gibbsite is heated to form alumina (Minerals Council of Australia, 1997). Several other side processes exist within the Bayer process, such as desilication, where dissolution and crystallization of silicates occur prior to the digestion process; causticization, where lime is added to recover the caustic lost during the process and oxalate removal where the major impurity of the process is removed.

The production of aluminium from alumina is based on the Heroult-Hall smelting process, in which the aluminium and oxygen are separated by electrolysis (Minerals Council of Australia, 1997). The alumina sold to smelters has to meet certain requirements, and these requirements impose a minimum specification for the product quality of the gibbsite produced.

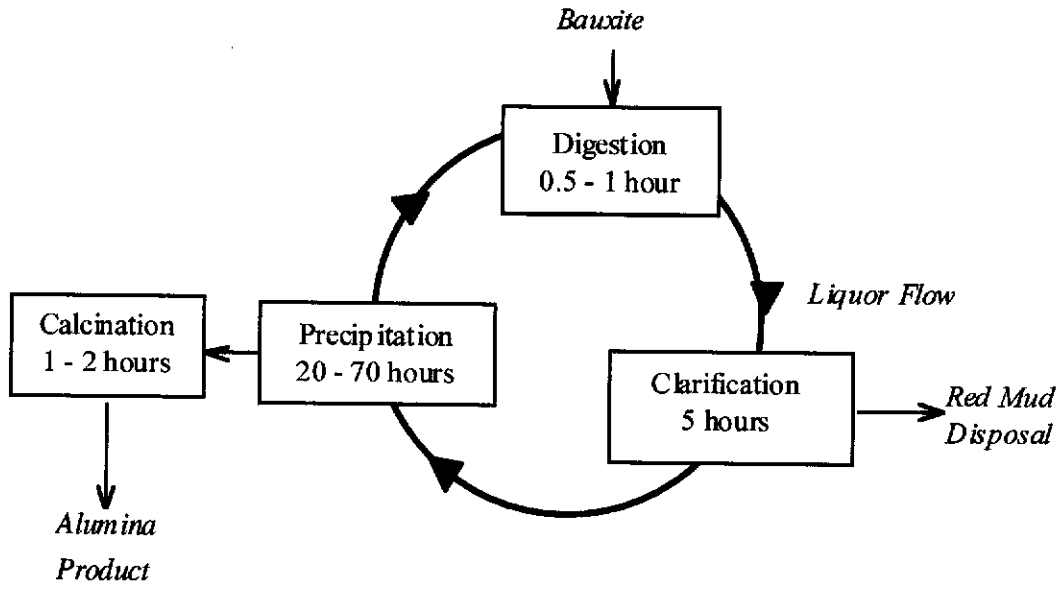

Figure 1.1 Simplified Schematic of the Bayer Process

1.2.1 Hydrothermal Digestion and Clarification

Bauxite is mined in an open cut mine, crushed and milled to below 20 - 30 mm, depending on the refinery, before the digestion process. The ground bauxite is then digested in aqueous sodium hydroxide solutions at temperatures between 130°C and 270°C (forward reaction of Equation 1). The digestion temperature depends on the mineralogy of the bauxite being processed, with gibbsitic bauxite dissolving at lower temperatures than the boehmite or diaspore bauxite (Debney, 1993; Hinde and Marantelli, 1993; Skiba, 1993).

After digestion, the slurry of aluminium-rich liquor and undissolved bauxite components, principally iron bearing minerals and desilication product, progress to the clarification process, where separation of liquid and solid occurs at greater than 100°C. This stage usually involves three steps, with the first step being the removal of coarse material or sand (greater than 100 μm), while the second stage involves the removal of the finer fraction (Debney, 1993; Gouma and Bhasin, 1993). These steps

are followed by several counter current washing steps to recover caustic soda. The final step in the clarification process is the filtration of the aluminium_rich liquor - *green liquor* - to remove any remaining solid. The green liquor is then sent to the crystallization step, while all the residue is disposed of in the red mud lakes.

1.2.2 Crystallization and Calcination

The crystallization of gibbsite, like most industrial crystallizations, is carried out in a continuous seeded crystallization system (reverse reaction of Equation 1). Seed is added to the clarified liquor at the beginning of the crystallization process which is at a temperature of 80°C. The liquor is then cooled in stages to approximately 60°C. This step-wise decrease in temperature is an attempt to control the crystallization process in order to obtain desirable product size, purity, strength and morphology. During the final stage of crystallization, the product is classified and washed. The coarse fraction progresses to the next stage of the process, calcination, while the fine fraction is recycled as seed crystals. The liquor is recycled back to the digestion process (Debney, 1993; Ghouma and Bhasin, 1993; Newchurch, Galloway and Moretto, 1993; Skiba, 1993).

The time spent in the crystallization process accounts for up to 40 hours of the approximately 50 hour process. The rate of gibbsite crystallization is an extremely slow process (linear growth rate of 1-2 μm/hour) (Misra and White, 1971), which accounts for the high residence time in the industrial crystallizers. Furthermore, the mechanism of gibbsite crystallization is not well understood, and hence there are many difficulties encountered in regulating the product quality.

The final product of the Bayer process is obtained by heating the precipitated gibbsite between 970°C and 1125 °C to obtain α-alumina in the calcination process (2) (Debney, 1993; Ghouma and Bhasin, 1993; Newchurch, Galloway and Moretto, 1993; Skiba, 1993).

$$Al(OH)_3 \xrightarrow{\Delta} Al_2O_3 + 3H_2O \qquad (2)$$

1.2.3 Bayer Liquor Composition and Speciation

Industrial Bayer liquor is a complex sodium aluminate matrix containing a wide range of impurities. Impurities enter the process primarily as constituents of the raw materials used. Due to the cyclic nature of the process, there is a build up in the level of impurities, which can affect the crystallization yield and product quality. Table 1.1 shows the major impurities found in the Bayer liquor and their origin and concentration at the start of the crystallization cycle. It has been shown that the presence of these inorganic and organic impurities increases the apparent solubility of the aluminate solution, hence decreasing liquor productivity (Bird, 1983).

The exact nature of the aluminate ion in solution is not clear. Electrochemical (Sipos *et al.*, 1997) and spectroscopic investigations (Watling, 1996) have shown the presence of a tetrahedral $Al(OH)_4^-$ ion to be the major species. The presence of aluminate polymers has been suggested; however, no conclusive evidence has been found. One current theory is that the formation of a more ordered species, for example $Al_2(OH)_7^-$ as suggested by King (1973), is the rate determining step in the crystallization process.

Table 1.1 Impurities in the Bayer Liquor (Sato et al., 1982; Tucker et al, 1986; Grocott, 1988; Rosenberg and Healy, 1996)

Compound	Origin	Concentration
Na_2CO_3	From reaction between carbon dioxide from the air and carbonates in bauxite with caustic	10 - 60 g/L
NaCl	As impurity in wash water and caustic	3 - 30 g/L
Na_2SO_4	As constituent of bauxite and added lime.	0 - 60 g/L
$Na_2C_2O_4$	From organic compounds in bauxite and its degradation	0.5 - 5 g/L
Ga_2O_3	Reaction of caustic and Ga_2O_3 in bauxite	120 mg/L
As_2O_5	From reaction of caustic and arsenic bearing minerals	40 - 400 mg/L
CaO	Added to the process in the cautisization step.	15 mg/L
V_2O_5	As a constituent of bauxite	500 mg/L
Organics	From the organic compounds in bauxite and their partial degradation products	2 - 45 g/L (as C)

1.2.4 Properties of Gibbsite

Gibbsite is one of three polymorphs of aluminium trihydroxide, the others being bayerite and nordstrandite. The crystal habit of natural gibbsite is usually pseudohexagonal tabular, while gibbsite precipitated in the Bayer process consists of agglomerates of hexagonal and diamond shaped crystals, and the crystal habit of synthetic gibbsite produced in the laboratory is determined by the crystallization conditions used. The major crystal faces of gibbsite have been identified to be (001) basal, and (110) and (100) prismatic (Figure 1.2) (Deer, Howie and Zussman, 1977).

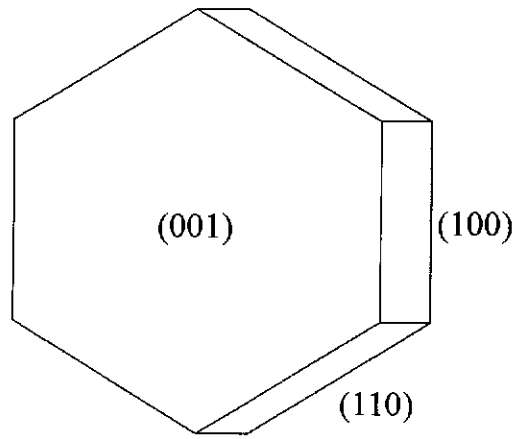

Figure 1.2 Major Gibbsite Crystal Faces

The three polymorphs of aluminium hydroxide have closely related structures, the difference between them being the stacking order of their $[Al_2(OH)_6]_n$ double layers (Figure 1.3). Bayerite is known to be thermodynamically more stable (Wefers, 1967), while gibbsite is naturally more abundant. It is believed that the inclusion of foreign ions such as those of alkali metals may affect the stacking sequence of the double layers, hence stabilizing gibbsite with respect to bayerite (Wefers, 1962; Saalfeld, 1968). The structural properties of aluminium trihydroxide are given in Table 1.2.

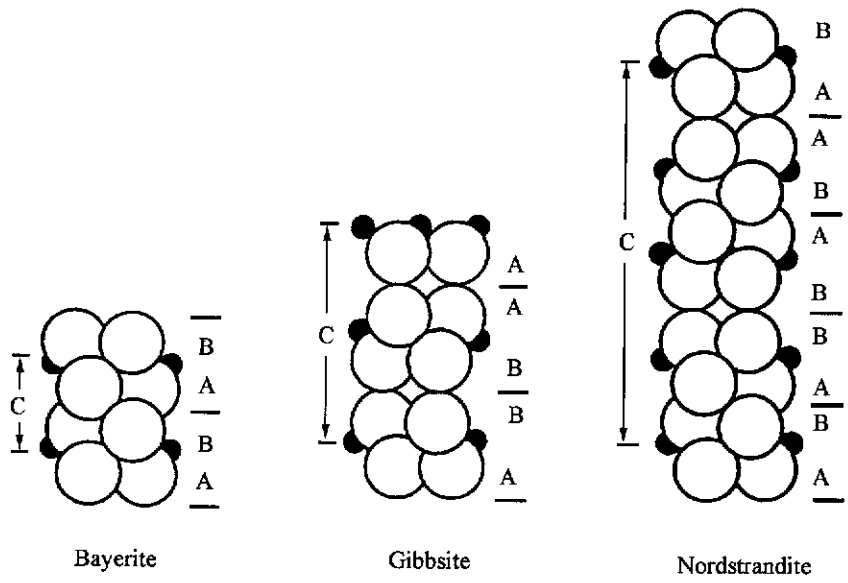

Figure 1.3 Layer Stacking of $Al(OH)_3$. (From Wefers and Misra, 1987)

Table 1.2 Structural Properties of Gibbsite (Saalfeld and Wedde, 1974), Bayerite (Rothbauer, Zingan and O'Daniel, 1967) and Nordstrandite (Bosmans, 1970)

	Gibbsite	Bayerite	Nordstrandite
Crystal System	Monoclinic	Monoclinic	Triclinic
Space Group	C_{2h}^5	C_{2h}^5	C_1^1
Molecules per unit cell	4	2	2
Unit Cell Parameters			
a (Å)	8.686	5.062	5.114
b (Å)	5.078	8.671	5.082
c (Å)	9.136	4.713	5.127
α			70.26°
β	94.57°	90.45°	74.00°
γ			58.47°

1.3. Crystallization Theory

Crystallization is widely used for the separation and purification of solids, and is a major processing step in hydrometallurgy. In the Bayer process, crystallization in an industrial crystallizer occurs through secondary nucleation and crystal growth. The processes of agglomeration and attrition also occur in the crystallizers. (Parkinson, 1996).

Secondary nucleation is the major source of new crystals in an industrial crystallizer, while crystal growth is responsible for the enlargement of pre-existing crystals.

There are several possible mechanisms for secondary nucleation and these include initial breeding, dendritic breeding, shear breeding and contact nucleation (van der Heijden and van Rosmalen, 1994). Initial breeding refers to the process when crystalline dust or fine fragments of the initial crystals are swept off when the seed crystals are introduced to a crystallizer, and act as nuclei, while dendritic breeding occurs when very high supersaturation results in the growth of dendrites or needles that can be removed under hydrodrynamic flows. Hydrodynamic forces can also cause the attrition of parent crystals. This process is known as shear breeding. The collision of the seed crystals with impeller blades, crystallizer walls as well as other seed crystals may result in the formation of nuclei, and this is known as contact nucleation.

Agglomeration is the process where two or more particles form an aggregate, which are then cemented with the precipitation of new material, while attrition refers to fragmentation of the crystal. Attrition differs from breakage in that, in attrition, the initial crystal size remains approximately the same and the formation of a number of

fragments results, while breakage results in the complete destruction of the initial crystal.

The work in this thesis is focussed on the crystal growth of gibbsite and the mechanisms of crystal growth will be discussed in Section 1.3.2

1.3.1 Driving Force and Supersaturation

The driving force in crystallization can be defined as the difference between the chemical potential of the crystallizing substances in solution (liquid, L) and the crystal (solid, S) (1). This chemical potential may be defined with a standard Nerst equation (2) where R is the gas constant, T the temperature and a is the activity of the solution related to the concentration (C), via the activity coefficient γ (3).

$$\Delta\mu = \Delta\mu_L - \Delta\mu_S \tag{1}$$

$$\mu = \mu_o - RTlna \tag{2}$$

$$a = \gamma C \tag{3}$$

Quantification of the driving force relies on a well defined supersaturation term. Supersaturation may be defined in a number of ways. Most simply supersaturation, ΔC, may be defined as the difference between the concentration of solute in the solution, C, and its equilibrium solubility concentration, C^*, (4). The value of this, however, depends on the units used in the concentration measurements. Supersaturation ratio, β, is an indicator independent of the concentration units and is expressed by Equation 7, while relative supersaturation, σ, is expressed by Equation 8.

$$\Delta C = C - C^* \tag{4}$$

$$\beta = C/C^* \tag{5}$$

$$\begin{aligned} \sigma &= \frac{C - C^*}{C^*} \\ &= \beta - 1 \end{aligned} \tag{6}$$

These expressions are only valid for ideal solutions and do not take into account the solute-solvent interactions. In real solutions, the difference between concentration and activity may be accounted for by relating the concentration of the solution via the activity coefficient. From the expressions for supersaturation and driving force, a dimensionless driving force for crystallization can be expressed as follows (7) (Mullin, 1994):

$$\begin{aligned} \frac{\Delta\mu}{RT} &= ln\frac{a}{a^*} \\ &= ln\frac{\gamma C}{\gamma^* C^*} \\ &= ln\left(\beta\frac{\gamma}{\gamma^*}\right) \end{aligned} \tag{7}$$

The accuracy of the supersaturation value depends strongly on the accuracy of the solubility data. Where experimental solubility data are not available, they may be calculated. Several models exist for determining the solubility of gibbsite in aqueous sodium hydroxide solutions as a function of temperature and caustic concentration (Pearson, 1955; Overbey and Scott, 1978; McCoy and Dewey, 1982; Moretto and Power, 1991).

Rosenberg and Healy (1996) have developed a thermodynamic model based on the dissolution of gibbsite in sodium hydroxide (Equation 1), taking into account the effect of impurities such as sulphate, chloride and organic carbon, and their interactions in the solution. The activity based equilibrium constant for the dissolution equation is given by Equation 10.

$$K_{eq} = \frac{\gamma_{Al(OH)_4^-}\left[Al(OH)_4^-\right]}{\gamma_{(OH)^-}\left[(OH)^-\right]} = e^{\frac{\Delta G_{rxn}}{RT}} \tag{10}$$

where

K_{eq} = *equilibrium constant at temperature T (K)*

R = *molar gas constant*

$\left[Al(OH)_4^-\right]$ *and* $\left[(OH)^-\right]$ = *concentration in molarity*

ΔG_{rxn} = *Gibbs energy for dissolution*

A simple Debye-Hückel equation was used to described the activity of an aluminate solution (Equation 11), while additional ionic strength terms were included to account for the hydroxyl ions (Equation 12). In calculating the ionic strength, several correction terms were included to account for the interaction between ionic sodium and impurity anions (Equation 13).

$$\log_{10} \gamma_{Al(OH)_4^-} = \frac{\alpha_1 \sqrt{I}}{1+\sqrt{I}} \tag{11}$$

$$\log_{10} \gamma_{OH^-} = \frac{\alpha_2 \sqrt{I}}{1+\sqrt{I}} + \alpha_3 I + \alpha_4 I^{\frac{3}{2}} \qquad (12)$$

$$I = 0.01887C + \frac{k_1[NaCl]}{58.44} + \frac{k_2[Na_2CO_3]}{105.99} + \frac{k_3[Na_2SO_4]}{142.04} + k_4 0.01887TOC$$

where TOC refers to the total organic content in g/L and (13)
C refers to the caustic concentration expressed in industrial terminology
The α terms refer to correction factors given in Table 1.3

Allowing for the notation and units used industrially, and rearranging the equations, results in an expression for calculating the equilibrium solubility of gibbsite which is given by Equation 14. Table 1.3 gives values for the correction factors and constants used.

$$A = \frac{0.96197\,C}{1 + \frac{10^{\frac{\alpha_o \sqrt{I}}{1+\sqrt{I}} - \alpha_3 I - \alpha_4 I^{\frac{3}{2}}}}{e^{\frac{\Delta G_{rxn}}{RT}}}} \qquad (14)$$

Table 1.3 Constants Used in the Rosenberg and Healy Model of Gibbsite Solubility

α_0	α_3	α_4	k_1	k_2	k_3	k_4	ΔG (kJ/mol)
-9.2082	-0.8743	0.2149	0.9346	2.0526	2.1714	1.6734	-30960

In this work, the above model will be used for calculating the equilibrium concentration, and hence supersaturation values of the solutions.

1.3.2 Crystal Growth

Crystal growth, in general, may be thought of as a two step process, with the first step being the transportation of the growth units to the crystal surface, followed by the integration of these units into the crystal. The relative importance of each of these will determine into which of the overall mechanisms of growth, a particular crystallization may be classified : - *diffusion controlled* or *integration controlled.* In the case of very concentrated solutions, heat and mass transport may play a part in the mechanism of crystal growth. Other factors such as the back diffusion of products of incorporation may also contribute to the rate of crystallization and hence affect the mechanism of growth.

1.3.2.1 Diffusion controlled crystal growth

This theory, first described by Noyes and Whitney (1897), assumes that the rate of crystallization is dependent upon the diffusion of growth units to the crystal surface, and is applicable mainly to materials with high solubility. Crystallization in these cases is considered to be the reverse of a dissolution reaction. In the case of gibbsite, although there is a high concentration of aluminium in solution, the concentration of gibbsite in solution is low, the integration of the growth unit is considered to be the growth controlling step (Parkinson, 1996), hence its crystallization is believed to follow one or more of the integration controlled growth mechanisms.

1.3.2.2 Integration controlled crystal growth

The integration of growth units onto the crystal surface is undoubtedly related to the atomic structure of the crystal surface and this structure can be affected by its surrounding solution, temperature, supersaturation and impurities (van der Heijden and van Rosmalen, 1994). The mechanism of crystal growth can be broadly classified

into rough growth or layer growth, and in both cases, all of the factors will affect the growth mechanism to some degree.

1.3.2.2.1 Rough Growth

Roughening of a crystal results when the difference in energy between a species in solution and when it is incorporated into the crystal lattice is small (van der Heijden and van Rosmalen, 1994). This implies that it does not matter at which surface position the incorporation of growth units occurs. In contrast, in smooth or layer growth, the incorporation of growth units is preferred at an edge of a step, resulting in flat crystal surfaces. Rough growth can result in the formation of curved crystal faces, dendrites and fractals.

There exists a *roughening temperature*, above which the transition from smooth growth to rough growth occurs. The roughening temperature is governed by the interaction between surface species with the solution species. Above the roughening temperature, the edge free energy on the crystal surface is zero which implies that the growth units can be incorporated on all surface sites because it makes no difference to free enthalpy. In contrast, below the roughening temperature, the edge free energy is greater than zero. Growth units may be either incorporated in the form of islands on the crystal surface, so the gain in free energy by crystallzation is larger than the cost to form the edges in the island, or be incorporated into the crystal at existing steps. (van der Eerden, 1994; Bennema, 1994).

The formation of islands on the crystal surface - two dimensional nucleation - can also result in surface roughening. This is known as *kinetic roughening*. In this case, the supersaturation or driving force must exceed that required for the formation of a growth unit or two dimensional nucleus, hence the need to grow with a layer mechanism is removed, and the surface will roughen. The growth rates in both

thermal roughening and kinetic roughening are proportional to the supersaturation (Parkinson, 1996).

1.3.2.2.2 Layer growth

According to classical crystal growth theories as first introduced by Kossel (1934), the growth of flat surfaces occurs by the preferential incorporation of growth units at kinks. These units are adsorbed on the terrace of the crystals, and move to the steps and kinks via surface diffusion. The stability of the growth units adsorbed on the surface of the crystal depends on the number of adjacent adsorption faces, which means that adsorption into the kinks is more stable than adsorption at steps or on terraces. (Figure 1.4).

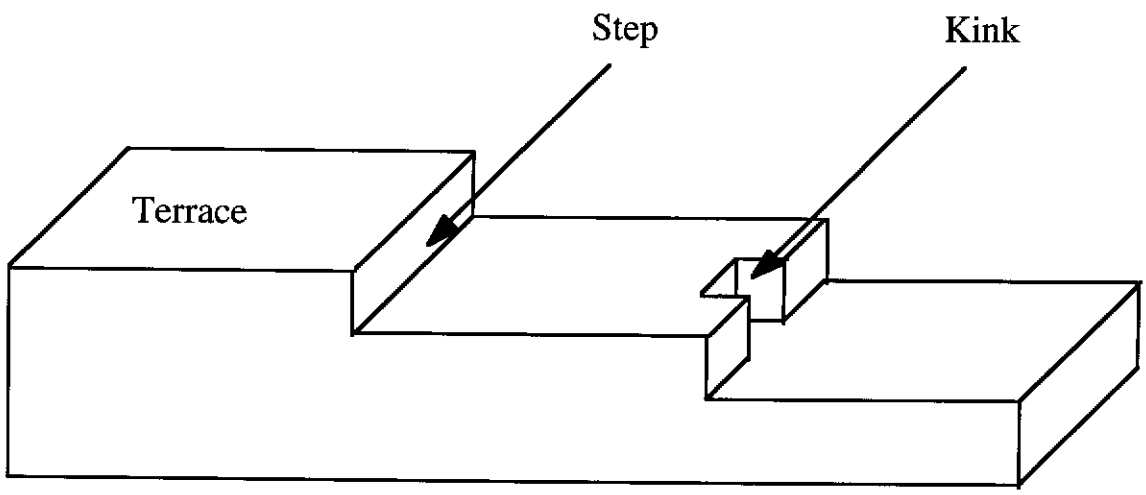

Figure 1.4 Surface Structure with Terrace, Step and Kink

The implication of this model is that the growth process will slow down or stop when a perfectly smooth surface is formed as the layers grow out, and thus the question of step formation needs to be addressed.

For a perfectly smooth surface, two dimensional nucleation acts as a source of steps. Several growth models based on two dimensional nucleation have been developed by O'Hara and Reid. (1973), and van der Eerden *et al.* (1978). The two dimensional nucleation mechanism is best described by the *birth and spread model* (Figure 1.5). The formation of a new layer occurs when the two dimensional nucleation barrier is exceeded, resulting in the formation of two dimensional nuclei. These islands or new layers spread along the crystal surface during the growth process. The simultaneous formation of multiple nuclei before the complete spread of existing layers, and the formation of nuclei on top of existing layers is also possible. These are known as polynuclear processes. The birth and spread model predicts a growth rate (*GR*) dependence on supersaturation that is given by Equation 15 (O'Hara and Reid, 1973; van der Eerden, Bennema and Cherepanova, 1978). Several models exist for predicting the growth rate dependence on supersaturation for the polynuclear process and these will be given in Section 1.4 and Section 5.2.3.4.

$$GR = A_1 \sigma^{5/6} \exp\left(A_2/\sigma\right) \tag{15}$$

where A_i are system related constants
and σ is the relative supersaturation

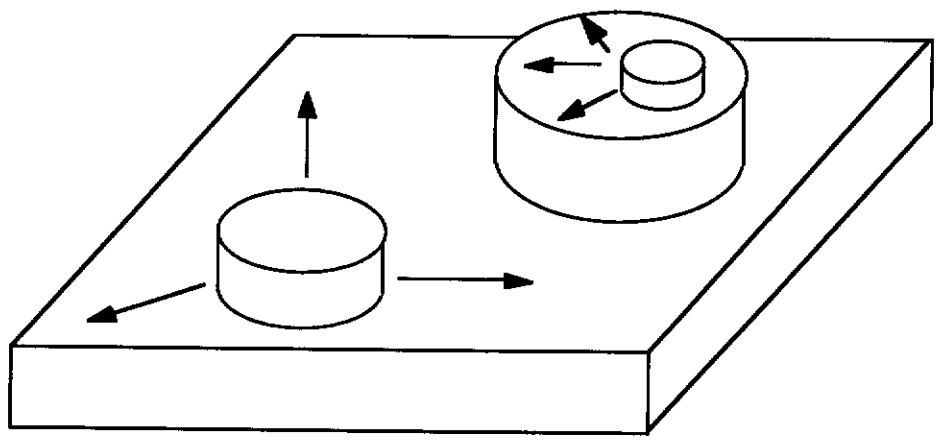

Figure 1.5 Birth and Spread Model

Most crystals are not perfect. Frank (1949) recognised this and showed that a screw dislocation terminating at a crystal surface can act as a continuous source of steps. The growth of these steps results in a formation of *spirals* (Figure 1.6) which will continue to act as further source of steps or preferred growth sites. Since a completely smooth surface never appears under these conditions, surface nucleation is not necessary and the growth continues uninterrupted. The theory describing the growth rate dependence on supersaturation for spiral growth was derived by Burton, Cabrera and Frank (1951) and is termed the BCF theory. The BCF model is expressed by Equation 16.

$$GR = A_1\sigma^2 \tanh\left(A_2/\sigma\right) \tag{16}$$

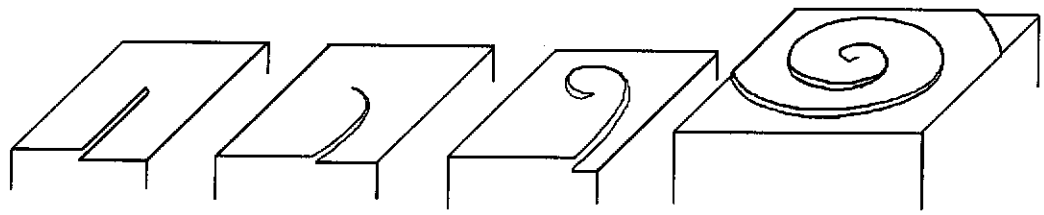

Figure 1.6 Screw Dislocation Leading to Spiral Growth

At low supersaturation, the BCF equation approximates to $GR \propto \sigma^2$, and at high supersaturations $GR \propto \sigma$. From the above equations, and the growth rate equation for the birth and spread model, a generalised growth rate equation may be expressed as:

$$GR \propto \sigma^n \tag{17}$$

1.3.3 Growth Rate Determination

Many techniques have been used to determine the growth rates of crystals. Measurements made on crystal size and population are useful in determining mass transfer and mass deposition rates, as well as in observing size dependent growth (Mullin, 1994). Experimentally, these are carried out in either batch or continuous crystallizers, and the overall growth rates are calculated from changes in particle size distribution and particle numbers, or from measurement of desupersaturation rates.

For more mechanistic information, single crystal growth techniques focussing on the growth of single faces are more suitable. Microscopic techniques, either *in situ* or *ex situ*, can be used to obtain information about the surface of the crystal faces and their behaviour during the growth process. Different crystal faces can grow at different rates under identical environments, due to the difference in the interaction between the growth unit and the crystal face, with the high index faces generally growing faster than the low index faces. This has implications for the morphology of the crystals, since the fastest growing faces are often eliminated by growing out. Changes in the relative growth rates of the crystal faces will therefore result in changes in the morphology (refer to Section 1.3.5).

An assessment of various techniques which have been employed to study crystal growth is given in Chapter 4.

1.3.3.1 Size Dependent Growth Rates and Growth Rate Dispersion

The effects of initial crystal size on the overall growth rate have been debated by many researchers (Garside and Davey, 1980; Ristic *et al.*, 1991). The effect of initial seed size is of particular importance when determining the overall growth rate in a crystallizer. In 1929, McCabe showed that all geometrically similar crystals of the same material will grow at the same growth rate (McCabe, 1929). This is now commonly known as the McCabe ΔL Law and states that the growth rate is independent of seed crystal size.

However, experimentally it has been shown that the growth rates of individual crystals do vary and this may be for a number of reasons. First, the hydrodynamics of the crystallizer needs to be considered. In an agitated crystallizer, the larger particles have a higher velocity than the smaller ones, hence will grow faster if diffusion is dominant in the growth mechanism. Furthermore, even in well agitated crystallizers, smaller particles may be caught in virtually stagnant regions, and hence have a lower growth rate.

Another reason for size dependent growth is that smaller crystals may have a lower local supersaturation. This is explained with the higher solubility of the smaller particles in solution, hence the slower growth rate. This is known as the *Gibbs - Thompson* effect (van der Heijden and van Rosmalen; 1994).

Oswald ripening also describes the tendency for smaller particles to dissolve and the solute subsequently depositing on the large particles causing them to grow larger. The driving force for the ripening process is the difference between the solubility of the small and large particles (Gibbs - Thompson effect) and results in the minimization of total surface free energy of the solid phase (Mullin, 1994).

On a microscopic level, the difference in growth rates may be due to the fact that larger crystals may tend to have more areas which show mechanical stress, dislocations and surface damage. This may result in a faster growth rate due to the faster integration kinetics (Ristic *et al.*, 1991).

The presence of mechanical stress, dislocations and surface damage may also lead to a reduction in growth rates (Ristic *et al.*, 1991). In addition, different crystals may have different strains, dislocation densities and amount of impurities adsorbed, resulting in differences being observed in the growth rates (Chernov, 1990; Ristic *et al.*, 1991). The phenomenon, *growth rate dispersion*, describes the variations in growth rates observed for apparently identical crystals under identical conditions as a result of the above mentioned factors.

1.3.4 The Effect of Impurities

The presence of various impurities in the system is known to affect crystallization. Some impurities, even at very low concentration have been found to inhibit or enhance the crystal growth process. There are several ways by which the impurity can act. First, the presence of an impurity may alter the solution speciation, thereby altering the supersaturation or solubility, and hence the crystallization driving force. Secondly, the impurity may be adsorbed onto the growth sites, preventing the incorporation of growth units onto these sites. The amount of impurity required depends on its preferential adsorption at kinks, steps or terraces, hence complete coverage of a crystal face may not be required before inhibition is observed (Davey and Mullin, 1976).

Impurities that act via surface adsorption often preferentially adsorb at particular crystal faces. The selectivity of the impurity depends on the mechanism by which it is incorporated or adsorbed onto a particular crystal face; hence, structural compatibility is required. Many impurities block crystal growth via two methods. First, by being structurally compatible with the crystal face and secondly by acting as a repellent for the further addition of growth units (Mullin, 1994).

Retardation of certain growth faces may enhance the relative growth of others and hence will alter the crystal habit (Mullin, 1994).

The use of additives to alter the relative growth rates and hence the morphology of the crystals has been reported by Davey, Polywka and Magini (1991) and Popowitz-Biro *et al.* (1991).

1.3.5 Miller Indices

All the faces of a crystal can be described and numbered in terms of their crystallographic axes intercepts. Miller (1839) showed that each crystal face may be represented by the indices *h*, *k* and *l*, obtained from the values of their intercepts at X, Y, and Z axes respectively. The Miller indices, represented by (*hkl*) for a crystal face or lattice plane, are inversely proportional to its axial intercepts, and negative intercepts are represented with a bar on the number, for example $(11\bar{1})$ representing a negative Z axis intercept. Figure 1.7 shows two simple crystals, with their crystal faces idexed using Miller indices.

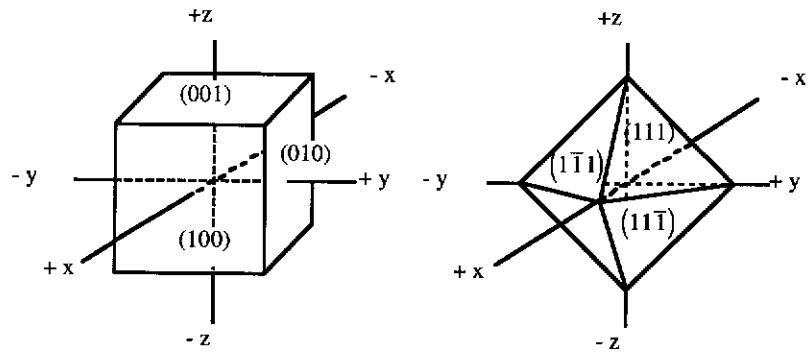

Figure 1.7 Two Crystals with their Faces Identified Using Miller Indices

1.3.6 The Morphology of Crystals

The morphology of a crystal depends on the relative growth rates of the different crystal faces; these growth rates are determined by the intrinsic crystal structure as well as by incorporated defects and the crystal environment. If relative growth rates of different faces are dominated by the crystal structure, the morphology of the crystal can be described by a combination of Bravais-Friedel and Donnay-Harker laws (Mullin, 1994) where the former states that the importance of a crystal face, hence its frequency of occurrence and relative surface area, is determined by its interplanar spacing where faces with higher indices are less important. The Donnay-Harker law extends this to take into account the effects of glide planes and screw axes. The physical basis for these laws was explained by Hartman and Perdok (1955) who considered the bond energies involved in the integration of growth units into the crystal lattice. Considering a hypothetical crystal (Figure 1.8), more bonds are formed when a growth unit is incorporated into the K (kinked) faces when compared to its incorporation into the S (step) faces and F (flat) faces, respectively. When considering the growth rates of crystal faces, associated with the growth is the

concept of attachment energy, which may be defined as the energy released per molecule when a slice d_{hkl} is formed. By comparing the attachment energies of each slice of each type of face, the small attachment energy for F-faces implies that the growth rate for this face is slow and hence will feature in the morphology of the crystal while S-faces are rarely occur and K-faces never occur as they are rapidly grown out.

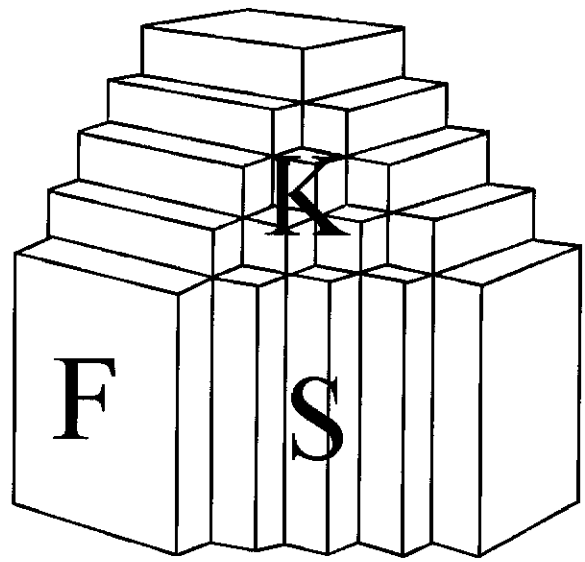

Figure 1.8 Hypothetical Crystal Showing F-faces (100), (010) and (001); S-faces (110), (101) and (011) and K-face (111) (From Hartman, 1963)

The total free energies, first used to described the formation of crystals (Gibbs, 1928), also has to be considered. In principle, the surface free energies of a crystal in equilibrium with its surroundings would be at a minimum, hence the development of the crystal faces and morphology should be such as to ensure that minimization of the surface free energy per unit volume is achieved.

1.4. Gibbsite Crystal Growth

Gibbsite crystallization from caustic aluminate solutions has been widely studied, but the mechanism by which the tetrahedral aluminate ion in solution transforms to an octahedral aluminate species in the crystal is still not understood.

Although gibbsite crystal growth occurs at all temperatures at which the industrial Bayer crystallizers operate, 60 - 90°C, nucleation and agglomeration needs to be minimised for growth studies. Misra and White (1971) showed that above 75°C, nucleation did not occur, and agglomeration may be reduced by using conditions unfavourable for the formation of the initial aggregates, such as by using a low seed charge.

The growth of a gibbsite crystal is believed to follow the Kossel model (Ohkawa, Tsuneimi and Hirao, 1985; Grocott and Rosenberg, 1988), where clusters of the solute molecules form the crystal growth unit. These growth units are adsorbed on the surface of the crystals with preference for kinks, steps and then terraces. Grocott and Rosenberg (1988) and Chaubal (1990) described the growth in terms of a five step process:

- Bulk diffusion of $Al(OH)_4^-$
- Boundary layer diffusion of $Al(OH)_4^-$ to reaction site
- Precipitation of $Al(OH)_3$
- Boundary layer diffusion of $(OH)^-$
- Bulk diffusion of $(OH)^-$.

It is also believed that a step involving the restructuring of the solution species to a more ordered species occurs before or during the precipitation step. This step is believed to be the rate limiting step in the growth process (King, 1973; Grocott and Rosenberg, 1988).

Bulk experiments have shown that the growth rate of gibbsite has a second order dependence on the supersaturation of the solution, suggesting a spiral growth mechanism consistent with the BCF model (Misra and White, 1971; Brown, 1972b; King, 1973; Overbey and Scott, 1978; Chaubal 1990). However, in contrast, the dependence of growth rate on the surface area and the negligible growth reported at low supersaturations suggest that the growth mechanism occurs not through a screw dislocation mechanism, but a birth and spread model (Brown, 1972b). Brown (1972b) also confirmed that at the beginning of the growth period, when supersaturation is high, the basal face of the gibbsite crystal roughens, resulting in a wavelike appearance due to the development of steps. With time, as the supersaturation level drops, the surface begins to smoothen as the layer grows out. However, the presence of screw dislocations, cannot be dismissed. Although the basal face appears flat, Gnyra, Jooste and Brown (1974) showed that all the common growth flaws such as twinning, internal grain boundaries and substructures, as well as dislocations can be found in what appears to be a perfect single crystal.

Several researchers have measured the growth rate of gibbsite using laboratory scale batch crystallization experiments (Misra and White, 1971; Brown, 1972b; Overbey and Scott, 1978; Veesler and Boistelle, 1994). The growth rate values were obtained either by determining successive particle size distributions or by measuring the amount precipitated. It is possible to obtain the growth rate from particle size distribution if the growth rate is independent of the initial particle size. The growth of gibbsite has been found to follow the McCabe ΔL law (McCabe, 1929), which implies that the growth rate is independent of the crystal size (Misra and White,

1971; Creswell; 1994, Veesler and Boistelle, 1994). The growth rate of gibbsite has been reported to be between 1-2 μm/hr and seldom exceeds 5 μm/hr (Misra and White, 1971).

From fundamental crystallization theories, as described in Section 3.2, the growth rate of a gibbsite crystal may be described by Equation 18.

$$\begin{aligned} \textit{Growth Rate (GR)} &= k\sigma^n \\ &= k\left(\frac{A - A^*}{A^*}\right)^n \end{aligned} \tag{18}$$

where σ = *relative supersaturation*

$k = k_o exp\left(-\Delta G / RT\right)$

R = *molar gas constant*

T = *temperature*

ΔG = *Activation Energy*

k_o = *kinetic coefficient, dependent on temperature and solution composition*

A = *initial aluminate concentration*

A^* = *equilibrium aluminate concentration*

In the literature, there are several growth rate equations quoted for gibbsite, and these are given in Table 1.4. Since the solubility of gibbsite is dependent on the caustic concentration, the equations that do not take into consideration the effect of caustic concentration have limited applicability. King (1973) proposed that the rate limiting step in gibbsite crystal growth is the adsorption of bialuminate $\left(Al_2(OH)_7^-\right)$ onto the surface and the loss of a hydroxyl ion from the adsorbed species to form gibbsite. Since the probability of hydroxyl release is inversely related to the hydroxyl concentration in solution, the growth rate can be expressed as a function of the

bialuminate concentration or the square of the aluminate ion concentration and the reciprocal of the hydroxyl ion concentration. King (1973) also showed that although experimental growth rates may be fitted to several equations, the best fit was represented by an equation which showed a dependence on the reciprocal of the concentration of free caustic (FC) (ie. caustic in solution that is not bound to aluminium species). The growth rate equation as proposed by King (1973) is given in Table 1.4.

White and Bateman (1988) showed that a decrease in the growth rate was observed with an increase in caustic concentration (C), while supersaturation remained constant. Supersaturation, here, was defined as the difference between the initial aluminate to caustic ratio and the equilibrium aluminate to caustic ratio. The growth rate, as described by White and Bateman (1988), is a function of the supersaturation squared and has a half order dependence on the caustic concentration (see Table 1.4).

As mentioned in Section 1.3.1, a supersaturation value calculated by concentration difference is dependent on the units used. Since the solubility of gibbsite is dependent on the caustic concentration, supersaturation values calculated by the concentration differences (ie $\left(A - A^*\right)$) is not suitable. Dimensionless units to describe supersaturation, taking into account the caustic concentrations are required to describe the driving force for gibbsite crystal growth. These are given as Equations 7 and 8 in Section 1.3.1.

Veesler and Boistelle (1993) reanalysed the experimental data of White and Bateman (1988) and King (1973) to obtain an equation describing the growth rate as a function of the relative supersaturation, as shown in the bottom of Table 1.4.

Table 1.4 Growth Rate of Gibbsite

	Reference
$GR = k\frac{\left(A - A^*\right)^2}{C^2}$	Pearson, 1955;
$GR = k\left(A - A^*\right)^2$	Misra and White 1971; Halfon & Kaliaguine, 1976
$GR = k\frac{\left(A - A^*\right)^2}{\left(FC\right)^2}$	King, 1973
$GR = k\frac{\left(A/C - A^*/C\right)^2}{C^{1/3}}$	White & Bateman, 1988
$GR = k\left(\frac{A - A^*}{A^*}\right)^2$	*Veesler & Boistelle, 1993; 1994*

Further work by Veesler and Boistelle (1994) in a semi-continuous constant composition crystallizer showed that the shape of the growth rates *versus* supersaturation curve indicated that either mononuclear two dimensional nucleation (19) or polynuclear two dimensional nucleation (20) is the primary growth mechanism. Veesler and Boistelle (1994) showed that the data fitted both equations and obtained the edge free energy (ϕ) of 0.02 kJ/mole, which is one order of magnitude smaller than a more plausible value obtained for NaCl (0.10 kJ/mole). Furthermore, the presence of dislocations in the seed crystals suggests that growth steps may be generated. Veesler and Boistelle (1994) cited these reasons when dismissing the birth and spread model as the main mechanism for gibbsite crystal growth.

$$GR_m = K_m \beta^3 (ln\,\beta)^{1/2} exp\left(-\frac{\phi^2}{3(kT)^2 ln\beta}\right) \quad (19)$$

$$GR_p = K_p (\beta - 1)^{2/3} \beta^{1/3} (ln\,\beta)^{1/6} exp\left(-\frac{\phi^2}{3(kT)^2 ln\,\beta}\right) \quad (20)$$

K_m & K_p = *Kinetic coefficients for mononuclear and polynuclear processes respectively*

β = *Supersaturation ratio*

$= A/A^*$

ϕ = *Bond energy between two first neighbours in the edge of the two dimensional nuclei*

k = *Boltzman constant*

T = *Temperature (K)*

The shape of the growth rate curve was explained by the presence of a dead zone (Veesler and Boistelle, 1994). This showed that a critical supersaturation, which is dependent on temperature, exists, below which the quadratic dependence of the growth rate on supersaturation is observed. Below this threshold, inhibition of growth by the presence of impurities becomes significant, and the rate cannot be described with the standard quadratic equation.

The activation energy is normally associated with a surface reaction being the rate controlling step in the reaction sequence. There is inconsistency in the literature values reported for the activation energy, which range from 53.1 kJ/mole to 83.3 kJ/mole (Veesler and Boistelle, 1994). However, all the activation energies are large and are consistent with particle growth being surface controlled. It is probable that

the large differences in values reported for the activation energy are principally due to the fact that the dependence of solubility on temperature and caustic concentration were not considered. When the caustic concentrations are taken into account, and the growth rate dependence on temperature is considered, an independent activation energy of 120.7 kJ/mol, and kinetic coefficient k_o of 1.92×10^{19} μm/hr are obtained (Veesler and Boistelle, 1994). These values are comparable with published values, when they are reanalysed to take temperature and caustic concentration into account.

The modified Veesler and Boistelle growth relation, which takes into account the concentration of caustic (in terms of equilibrium solubility, A*) and the temperature is given by Equation 21.

$$GR\,(\mu m/hr) = k_o(\beta - \beta_c)^2 \exp\left(-\Delta G/RT\right) \qquad (21)$$

$$\text{where } \beta = \frac{A}{A^*}$$

$$\beta_C = \text{critical supersaturation}$$

$$= 1 \quad \text{(for pure solutions)}$$

$$\Delta G = 120.7\,kJ/mol$$

$$k_O = 1.92 \times 10^{19}\,\mu m/hr$$

$$ie\ GR = k_O(\sigma)^2 \exp(-\Delta G/RT),\ \text{for pure solution.}$$

All the reported growth rates have been determined by measuring the increase in gibbsite crystal size or by measuring the decrease in the aluminate concentration in solution, and most studies have been of bulk growth. King (1973) determined the growth rate of gibbsite single crystals using optical microscopic methods. In this work, the sizes of gibbsite single crystals were measured before and after growth for a measured time, to obtain its growth rate. Although an increase in growth rate with

increasing aluminate concentration was observed, the ratio of the net growth rate of the prismatic faces to the basal face was found to be constant at 1.3. The growth rates of the individual prismatic faces were not differentiated.

Laboratory seeded batch precipitation of gibbsite is often preceded by an *induction period*, followed by a period of rapid precipitation (Smith and Woods, 1993; Rossiter *et al.*, 1996) The induction period may be defined as the time between the addition of seed to the supersaturated solution and the onset of measurable precipitation. The duration of the induction period is therefore dependent on the sensitivity of the instruments used. The induction period phenomenon has been studied by several researchers using spectroscopy techniques, scanning electron microscopy and conductivity measurements (Smith and Woods, 1993; Rossiter *et al.* 1996). Brown (1972a, 1972b, 1975) has shown that the end of the induction period is accompanied by the rapid formation of new particles, due to secondary nucleation. Smith and Woods (1993) showed the existence of slow growth during the induction period. These studies were based on the changes in the solution composition, and information on the seed surface was obtained by sub-sampling solids from the crystalliser.

Smith and Woods (1993) found that the induction period was affected by the crystal surface of the seed. On using dried seed, the induction period was found to increase, and it was concluded that the induction period is the time taken for the re-activation of the seed surface. In contrast, Ni and Romanov (1975) claimed that the induction period is a property of the liquor, while Ilievski *et al.* (1989) showed that the duration of the induction period was reduced but not eliminated when using active seed.

The detrimental effects of organic impurities on gibbsite precipitation in the Bayer process have been reported by several researchers (Grocott and Rosenberg, 1988 Power, 1991). Bauxite contains humates, fulvates, lignin, cellulose and protein materials, and as a result, particularly after their degradation at high pH and temperature, there is an enormous range of organic materials in Bayer liquor. Lever (1978) used various chromatographic methods for the separation and identification of these organic compounds, while Guthrie *et al.* (1984) used gas chromatography-mass spectrometry and gel permeation chromatography to identify some of these organic compounds. Most organic compounds found in the Bayer liquor were found to be formed as a result of the degradation of the organic compounds from the bauxite during the digestion process.

Some organic impurities which enter the process continuously have been found to be a strong crystallization inhibition of gibbsite (Grocott and Rosenberg, 1988; Power, 1991). In small quantities, certain organic molecule have been found to affect crystallization of gibbsite by reducing the yield and product quality in terms of the level of sodium incorporation and its particle size distribution (Grocott and Rosenberg, 1988; Armstrong, 1993)

Studies on the effects of individual organic compounds on precipitation yield have showed that there are correlations between the structure of organic molecules and their effect on yield (Grocott and Rosenberg, 1988; Power, 1991). These studies showed that adjacent hydroxyl groups are required for the inhibition to occur, with preference for acidic polyhydroxy compounds rather than carboxylic acid compounds. Sodium gluconate, which may be present in the liquor as a degradation product has been found to be a particularly good inhibitor, and this is often used to stabilize liquor during some analytical procedures.

The preference for hydroxyl groups suggests that the mechanism of inhibition is related to the ability these compounds have to form complexes with the aluminium. The concentration of these species is too low to account for the decrease in yield if the inhibition is due to complexation of these species with aluminate ions in solution, and hence it is believed that inhibition of occurs via a surface controlled mechanism.

Studies by Smith *et al.* (1994), showed that not only is the presence of adjacent hydroxyl groups important, the stereochemistry of the compound is also important. This study showed that while D/L tartaric acid inhibits crystallization, meso tartaric acid was found to be a more effective inhibitor. This work again suggests that preferential adsorption of these species to the crystal surface is a key to the inhibition mechanism.

The mechanism of growth inhibition is believed to be via the preferential absorption of the organic molecules to growth sites on the surface, preventing the incorporation of actual growth units (Grocott and Rosenberg, 1988, Power, 1991; Armstrong, 1993). As a result of this inhibition, dendritic growth occurs due to a relative increase in local growth rate on the non-poisoned growth sites. The adsorption of these impurities on the crystal surface will also inhibit sodium diffusion out of the crystal surface and the increase in local growth rates provides insufficient time for sodium diffusion, resulting in a product with a higher sodium content.

The effects of other impurities, such as sodium carbonate, sodium sulphate and sodium chloride, on precipitation have been studied by Bird *et al.* (1983); Lectard and Nicolas, (1983); and Satapathy and Vidyasagar, (1990). The impurities were tested individually and in combination. All these impurities were found to increase the solubility of the aluminate species, thereby decreasing the yield. (Bird *et al.* (1983); Lectard and Nicolas, (1983); Satapathy and Vidyasagar, (1990).

1.5. This Work

1.5.1 Significance

The conversion of bauxite ore into alumina, via the Bayer process, is a well established major industry. However, the rate of precipitation of aluminium trihydroxide as gibbsite is an extremely slow process and is undoubtedly the rate limiting step to productivity, with the aluminium spending more than half its processing time in large capitally intensive tanks. There is therefore a considerable interest in the alumina industry in understanding the mechanism of gibbsite crystallization with a view to increasing productivity.

Although a mature industry, the mechanism of gibbsite crystal growth is not well understood and difficulties are encountered in regulating particle growth to achieve desirable characteristics of purity, strength, morphology and size distribution. Understanding the fundamentals of gibbsite crystal growth will naturally yield information to enable better control of these parameters.

Although gibbsite crystal growth has been studied extensively, there are still conflicting views on the mechanisms that operate. According to growth rate expressions from bulk experiments, growth rate = $k\sigma^2$, the second order dependence on supersaturation suggesting that spiral growth is the main contributing mechanism by which gibbsite growths. Microscopic investigations of the crystals, however, suggest the birth and spread model to be the main mechanism for gibbsite crystal growth. The question of which mechanism is operational therefore arises - does the growth of gibbsite crystals follow the birth and spread model as suggested visually, or the BCF model as inferred from the growth rate relation to

supersaturation? It is also possible that the growth mechanism differs for individual crystal faces.

1.5.2 Objectives, Approach and Expected Outcomes

The primary aim of this work is to obtain mechanistic information on the growth of gibbsite crystals and this has been achieved through two parallel studies - the growth of gibbsite crystals and the resulting morphology of gibbsite. Before either aspect can be considered, the crystals need to be well characterized.

Several methods of precipitating aluminium hydroxide were considered. These included the conventional Bayer process technique of seeding aluminate solutions, slow desupersaturation of caustic aluminate solutions by addition of acid or carbon dioxide, and ageing of the aluminate solutions in the absence of solids.

The precipitates were characterized using various electron microscopic techniques and X-ray diffraction. The characterization work yielded a technique for the preparation and identification of gibbsite and its polymorphs. Gibbsite was then characterized further, and its crystal faces identified. This is essential for the study of crystal growth on the individual crystal faces.

Although a body of work has been reported on the bulk growth rate of gibbsite, the growth of individual crystal faces has been examined only by King (1973). Because of the difference in the atomic structure of the crystal faces, differences in growth rates of these faces are expected, due to the differences in the interactions between the growth units and the surfaces which present chemically different aspects to the solution. Several *in situ* microscopic techniques have been considered in this work

and assessed for their ability to determine growth rates. *In situ* techniques were also considered for the determination of the overall growth rate of the gibbsite crystal as a complement to the measurement of crystal face growth rates.

The effect of supersaturation on growth rate was investigated and the effect of selected organic compounds on the growth of individual crystal faces examined for potential selective inhibition. From the microscopic work, mechanistic information was obtained visually and also inferred from the relationship between growth rates and supersaturation. The growth rates of the prismatic crystal faces are expected to be similar to each other due to the similarities in the atomic structure of these faces; whereas a difference in growth rates is anticipated between the prismatic faces and the basal face, because of the layer structure of gibbsite.

The activation energies of each crystal face were also determined from the growth rate dependence on temperature at a constant supersaturation.

The effect of initial seed size was studied and the growth rate dispersion phenomenon investigated.

Changes in the relative growth rates of individual crystal faces result in changes in crystal habit. By studying these changes, information may be obtained about the mechanism of growth. The growth of gibbsite is known to be decreased by the addition of certain organic compounds. The morphology of gibbsite crystals grown in the presence of organic compounds were studied to investigate the selectivity of action on different crystal faces during the growth process.

The work carried out by Smith *et al.* (1994), indicated the importance of stereochemistry in the inhibition of gibbsite crystal growth. Since the atomic structures of the individual crystal faces differ, it is expected that these organic poisons will selectively inhibit the growth of certain crystal faces. Again, because of the similarities between the structure of the prismatic faces, it would be difficult to inhibit one of the prismatic faces without affecting the other. Selectivity between prismatic and basal faces would be more likely, with preferential inhibition of the basal face with respect to the prismatic resulting in the formation of elongated hexagonal prisms.

Crystal morphology may also be altered by changing the crystal lattice, for example by the incorporation of impurities into the crystal. The effect of alkali metal ion incorporation on the morphology of gibbsite was investigated both experimentally and computationally.

Chapter 2

Characterization of Aluminium Trihydroxide

2.1. Introduction

There are three polymorphs of aluminium trihydroxide: gibbsite, bayerite and nordstrandite. The major difference between the three polymorphs is in the stacking order of their $[Al_2(OH)_6]_n$ double layers (see Figure 1.3). The inclusion of impurities may affect this stacking sequence.

Bayerite may be formed by reacting aluminium chloride solution with ammonium hydroxide, by neutralizing sodium aluminate solutions with carbon dioxide at room temperature or by autoprecipitating aluminate solutions at room temperature (Fricke and Wüllhorst, 1932). Immersion of amalgamated aluminium in water at room temperature has been reported to form well crystallized bayerite (Schmäh, 1946). Other methods of bayerite preparation include hydrolyzing aluminium alcoholates at temperatures below 40°C (Fricke and Jockers, 1947) and electrolytically using platinum cathodes and aluminium anodes with H_2O_2 as an electrolyte (Torkar and Bergmann, 1960).

The reported morphology of bayerite depends on the method of preparation, but usually bayerite takes the form of somatoids, with an "hour glass", cone or spindle shape (somatoids are defined to be "bodies" of uniform shape that are not enclosed by crystal faces).

The formation of nordstrandite was first discovered by Van Nordstrand (1956) as a product of ageing the gelatinous precipitate formed by reacting aluminium chloride or nitrate solutions with ammonium hydroxide at a pH of 7.5 to 9. Hauschild (1963) showed that very pure nordstrandite can be prepared by reacting aluminium, aluminium hydroxide gel or hydrolyzable aluminium compounds with aqueous

solutions of alkylenediamines, especially ethylene diamines. The morphology of nordstrandite has not been reported.

The morphology of synthetic gibbsite is believed to be determined by the crystallization conditions (Wefers and Misra, 1987), while natural gibbsite usually takes the form of small tabular crystals with the {001} basal face and {100} and {110}faces forming its pseudohexagonal outline.

A study by Misra and White (1971) showed that single crystals of up to 40 μm can be produced from potassium aluminate solutions (rather than sodium aluminate solutions) under conventional Bayer process type conditions. Wefers (1962) suggested that the inclusion of potassium ions results in the formation of elongated crystals that are morphologically quite perfect, whilst with the inclusion of sodium ions, results in less well formed crystals with growth distortion. Wefers (1965) also suggested that the inclusion of these cations is necessary to stabilize gibbsite with respect to bayerite, and the transformation of bayerite to gibbsite occurs on ageing bayerite in saturated caustic aluminate solutions.

Carbonation (reaction of caustic solution with carbon dioxide) of potassium aluminate solutions at elevated temperatures (70 - 80°C) is reported to result in the formation of large (~80 μm) single crystals of gibbsite (Rosenberg, 1993). A study by Wojcik and Pyzalski (1990) however, showed bayerite to be the predominant species formed in the carbonation process of potassium aluminate and sodium aluminate solutions between 50 - 80°C.

In this section of the work, several methods of growing crystals were employed, using both sodium aluminate and potassium aluminate solutions, at either room

temperature or 70°C. The precipitates were characterised using scanning electron microscopy to examine the morphology of the crystals and powder X-ray diffraction to identify the major phases present. X-ray diffraction provides a fast and non ambiguous answer in the indentification of polymorphs because the differences bewteen the crystal lattices of the polymorphs will result in different diffraction patterns. The characterization work helped refine a technique for the preparation and identification of gibbsite and its polymorphs. Gibbsite has subsequently been characterized further in this work, and its crystal faces identified. This was an essential precursor to the study of crystal growth of the individual crystal faces.

Bayerite and nordstrandite were also prepared by the methods described in the literature (Thomas and Sherwood, 1992).

2.1. Experimental

2.1.1 Preparation of Bayerite and Nordstrandite from Aqueous Media

The preparation of bayerite and nordstrandite, as described in the literature (Thomas and Sherwood, 1992), requires the prior formation of amalgamated aluminium. This was prepared by ageing washed aluminium wire (washed with acetone and ethanol, followed by Milli-Q water) with 0.1M mercuric chloride ($HgCl_2$) at 30°C for 5 minutes. After the coating process, the aluminium wire was washed three times with Milli-Q water. In the preparation of bayerite, the amalgamated aluminium was aged in electrolyte free water, while for nordstrandite, the amalgamated aluminium was aged in aqueous ethylenediamine (approximately 20%v/v) for 4 days. The precipitates were collected by filtration, washed with deionised water and air dried.

To examine the effect of temperature on the polymorph formed, amalgamated aluminium was also aged in Milli-Q water at 80°C for 24 hours.

The preparation of aluminium hydroxide from caustic aluminate solutions will be discussed in the following sections.

2.2.2 Solution and Solid Preparations

2.2.2.1 Solution Preparation

It is believed that the digestion of gibbsite at atmospheric temperature is insufficient for its complete dissolution, and higher temperatures are required for its complete dissociation (Gerson *et al.,* 1996). The atmospheric digestion of aluminium wire produces a solution similar to that from high temperature digestion of gibbsite (Gerson *et al.,* 1996). There is also concern that gibbsite may contain a number of impurities, for example calcium and iron. For the purpose of this work, the solutions used for morphological studies were prepared using gibbsite, while for growth rate determinations, solutions were prepared using aluminium wire. This is because the growth rates may be affected by the presence of other aluminate species or undissolved gibbsite templates may affect the growth rate of gibbsite, while the morphology will not be affected.

All the alkaline aluminate solutions used in this section of the work were prepared using gibbsite with either sodium hydroxide or potassium hydroxide using the method discussed below (Section 2.2.2.1.1)

2.2.2.1.1 Preparation from Gibbsite

The aluminate solutions (synthetic Bayer liquors) were prepared using gibbsite (C31, Alcoa Chemical Division, Arkansas), sodium hydroxide pellets (AR grade) and sodium carbonate (AR grade). A mixture of gibbsite, sodium hydroxide and deionised water was heated, with stirring, in a stainless steel vessel, covered to minimize evaporation, until the gibbsite had dissolved. This was then added to pre-dissolved carbonate in water. The solutions were allowed to cool and made up to volume with deionised water in a volumetric flask. The solutions were filtered through a 0.22 μm membrane prior to use.

2.2.2.1.2 Preparation from Aluminium Wire

Aluminate solutions may also be made by dissolving aluminium wire in sodium hydroxide solutions. The wire was washed with ethanol, acetone and then with deionised water prior to use. The aluminium wire was dissolved in hot sodium hydroxide solution at 100°C, in a covered stainless steel vessel with stirring. Once complete dissolution had occurred, the solutions were allowed to cool, and made up to volume with deionised water in a volumetric flask. The solutions were filtered through a 0.22 μm membrane prior to use.

2.2.2.2 Solid Preparation

The precipitates were collected by filtration through a 0.45 μm membrane, washed with hot de-ionised water and air dried at room temperature. The precipitates were characterised using powder X-ray diffraction (XRD) and scanning electron microscopy (SEM).

2.2.3 Precipitation Conditions

The amount of aluminium dissolved in the synthetic Bayer liquors studied here is in excess of the equilibrium solubility of the $Al(OH)_3$ polymorphs, and solid will precipitate if the solutions are simply left for a sufficient period of time, referred to as ageing (4 - 48 hours, depending on conditions). The ageing period described above includes the crystallization induction time and some precipitation. The rate of precipitation can be increased by the addition of seed crystals or by partially neutralising the alkali hydroxide by the addition of carbon dioxide or acid in the absence of seed.

2.2.3.1 Ageing of Aluminate Solutions

The aluminate solutions were allowed to age for up to 48 hours at room temperature or for up to 4 hours at 70°C in the absence of any seed crystals or the addition of acid or CO_2.

2.2.3.2 Addition of Carbon Dioxide Gas (Carbonation)

Bubbling carbon dioxide through a tube into synthetic Bayer liquors at moderate rates results in the exit holes for the gas becoming blocked by precipitated gibbsite. To try to overcome this problem, and thus achieve reproducible rates of precipitation, two approaches were adopted. First, carbon dioxide was bubbled through a bubbler ring with many holes into a stirred sodium or potassium aluminate solution at room temperature or 70°C (Figure 2.1). Secondly, carbon dioxide was bubbled through a gas chromatography syringe (0.5 mm diameter) into a potassium aluminate solution at 70°C, with no stirring.

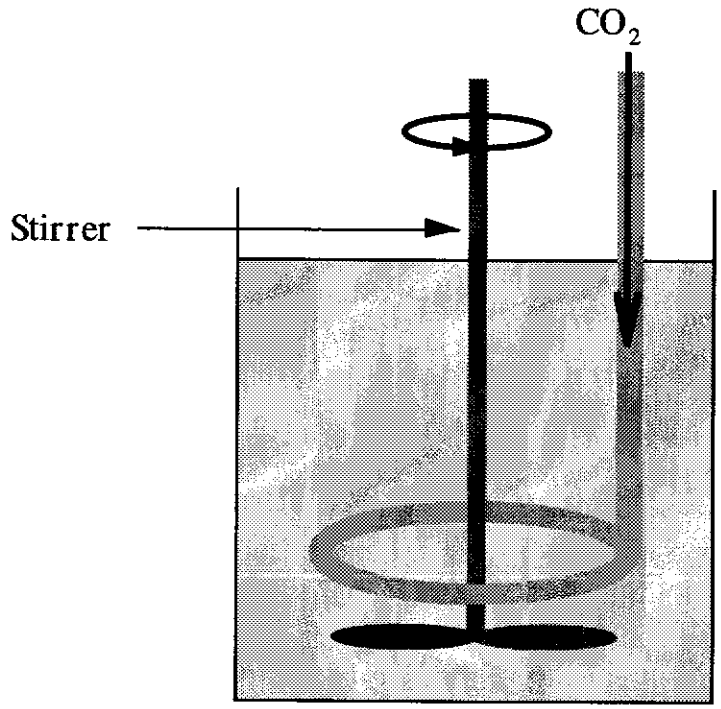

Figure 2.1 Carbonation Reactor

2.2.3.3 Addition of Acid

Hydrochloric acid (0.5 moles/L) was added dropwise via a peristaltic pump to a stirred sodium or potassium aluminate solution at room temperature or 70°C, at a rate of 0.5 mL/min. The volume of acid added completely neutralised the caustic solution.

2.2.3.4 Addition of Seed

Sodium or potassium aluminate solutions were seeded with 10 g/L of gibbsite (C31) or bayerite in Nalgene polypropylene bottles and tumbled end over end at 70°C for 2 hours.

2.3. Results

2.3.1 Nordstrandite, Pseudo-boehmite and Boehmite

The precipitate collected from ageing amalgamated aluminium in electrolyte free water at room temperature was identified by XRD as bayerite. The morphology of these crystals consisted of spindle and cone shaped somatoids (Figure 2.2) which agrees with the reported morphology of bayerite (Wefers and Misra, 1987).

The gelatinous product obtained from ageing amalgamated aluminium at high temperature was identified by XRD as pseudo-boehmite. The X-ray diffraction pattern of pseudo-boehmite shows broad lines that coincide with the major reflections of well crystallized boehmite with a shift towards higher d-spacing values in the direction of the b-axis. The increase in the unit cell dimension has been ascribed to the additional water found in gelatinous boehmite compared to the well crystallized boehmite. Papée *et al.* (1958) and Lippen (1961) account for the additional water as intercalation of water molecules while Baker and Pearson (1974) claimed that the excess water found in gelatinous boehmite is coordinated to the aluminium in the crystal. The morphology of pseudo-boehmite (Figure 2.3) produced from this study is quite unlike that of boehmite (Figure 2.4) formed by thermally (250°C) treating gibbsite in the presence of water.

Figure 2.2 Bayerite with Somatoid Morphology (Full scale = 15 μm)

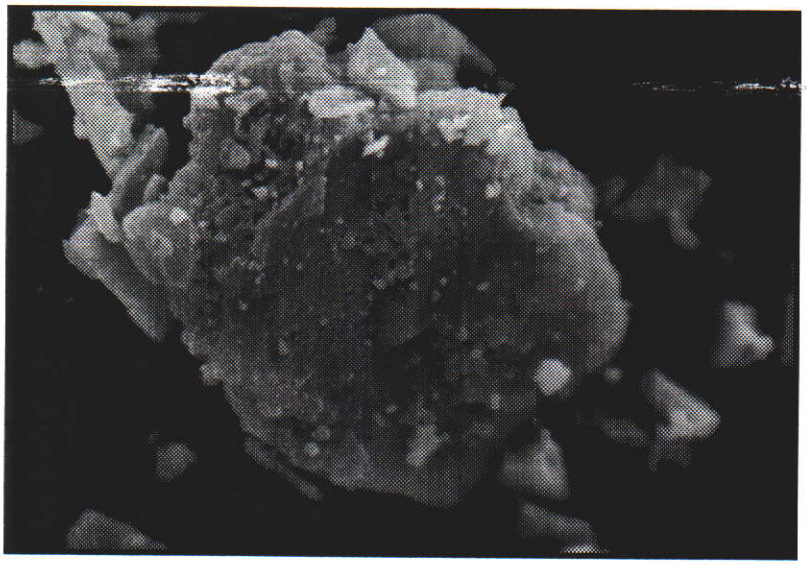

Figure 2.3 Pseudo-boehmite (Full scale = 55 μm)

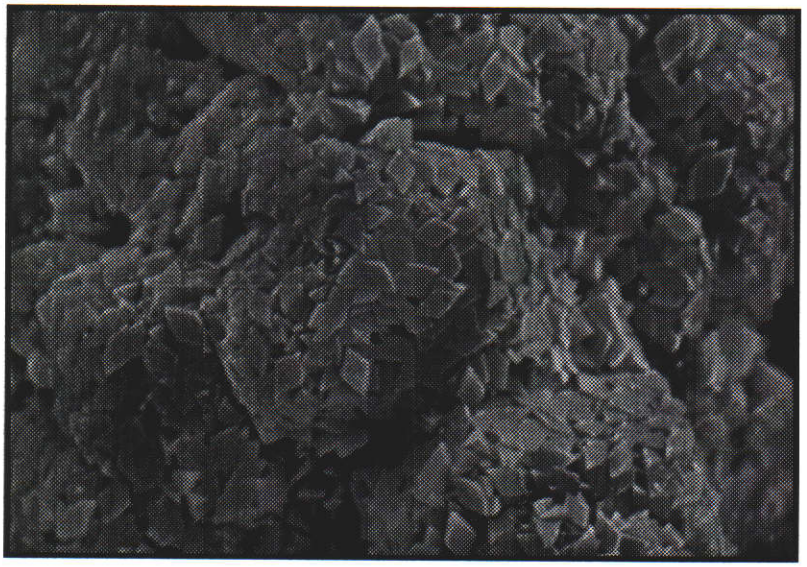

Figure 2.4 Boehmite (Full scale = 28 μm)

The product produced from ageing amalgamated aluminium in aqueous ethylene diamine was identified by XRD as nordstrandite with a trace amount of bayerite if aged for 4 days or just nordstrandite if aged for 7 days. The morphology of nordstrandite in the presence of bayerite consisted of somatoids (Figure 2.5), while the morphology of just nordstrandite consisted of agglomerates of cubic shaped crystals (Figure 2.6).

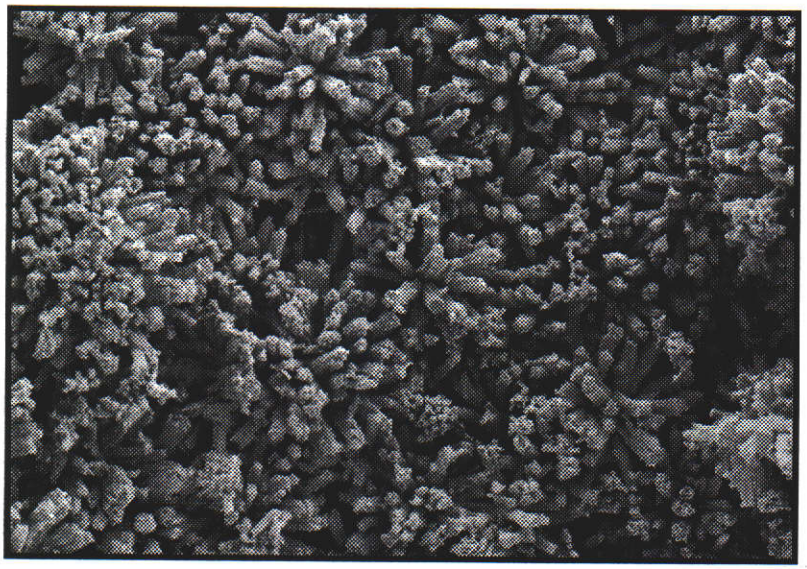

Figure 2.5 Nordstrandite with Trace Amounts of Bayerite (Full scale = 150 μm)

Figure 2.6 Nordstrandite (Full scale = 15 μm)

2.3.2 Bayerite Formation and its Morphology

2.3.2.1 From Sodium Aluminate Solutions

The initial products obtained from ageing sodium aluminate solution at room temperature (after 16 hours) were mainly calcium containing compounds ($CaCO_3$ and $3CaO.Al_2O_3.CaCO_3.11H_2O$), FeO(OH) and some bayerite. Calcium and iron (identified by energy dispersive spectroscopy in the products) are present as impurities in the reagents used for liquor preparation. The X-ray diffraction patterns (Figure 2.7) show the development of the bayerite peaks (2θ = 18.8, 20.4, 40.6, 53.2°) and the decrease of the $3CaO.Al_2O_3.CaCO_3.11H_2O$ peak (2θ = 11.6°) with time.

The morphology of the precipitate collected after ageing sodium aluminate solution for 16 hours consisted of rounded aggregates of plates (Figure 2.8). Bayerite with a *woolball* morphology was observed after 48 hours (Figure 2.9). The bayerite crystals produced by the carbonation of sodium aluminate consisted of *web-like* and *frond* shaped crystals (Figure 2.10), while the bayerite from the addition of acid to the sodium aluminate solution formed agglomerates of triangular prisms that showed radial growth characteristics (Figure 2.11).

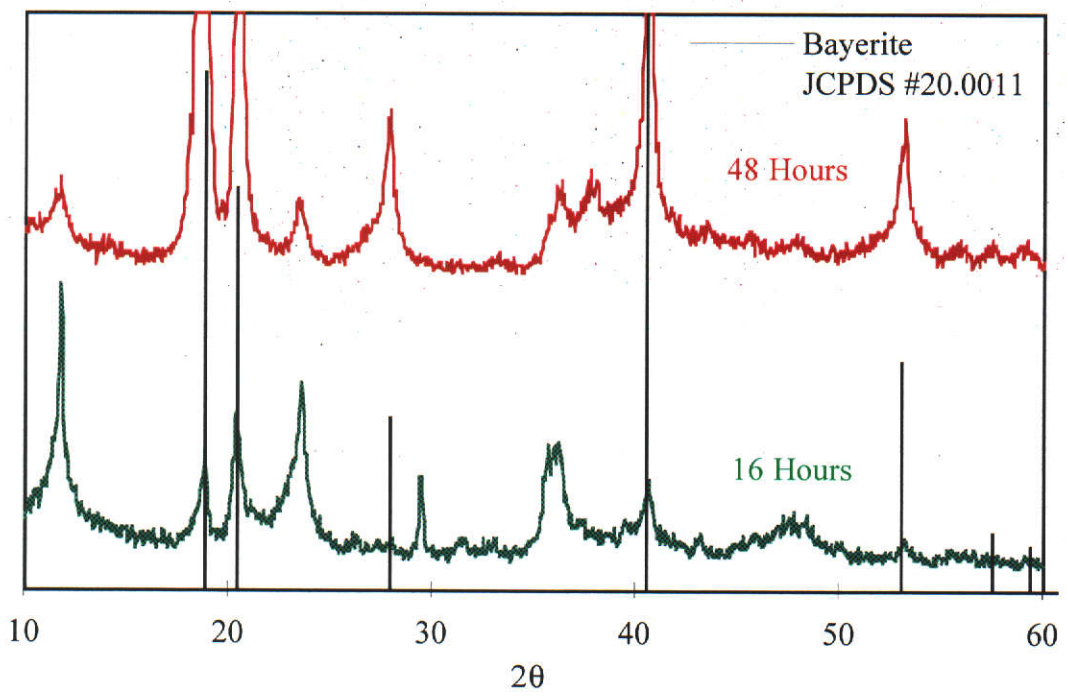

Figure 2.7 XRD Patterns of Precipitates Collected from Ageing Sodium Aluminate Solutions at Room Temperature

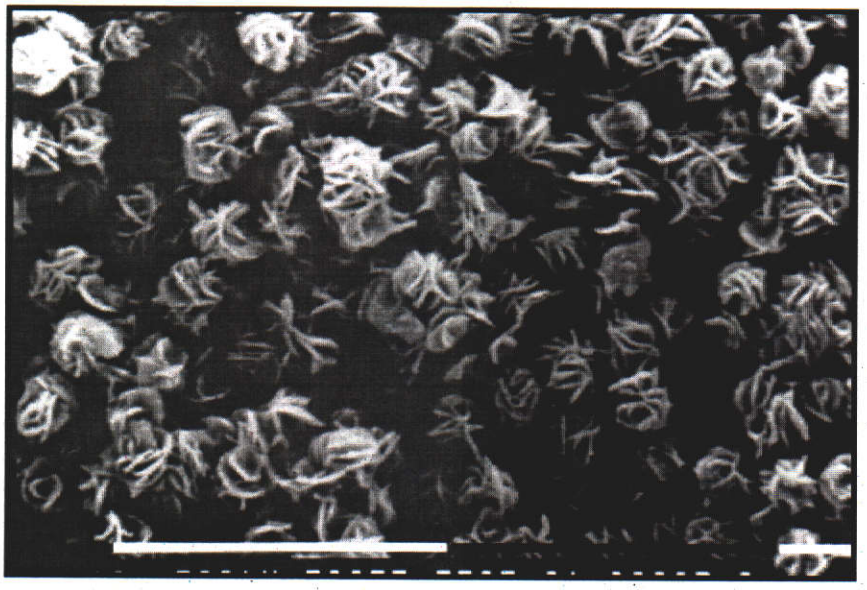

Figure 2.8 Precipitate from Sodium Aluminate after 16 Hours at Room Temperature (Scale Bar = 10 μm)

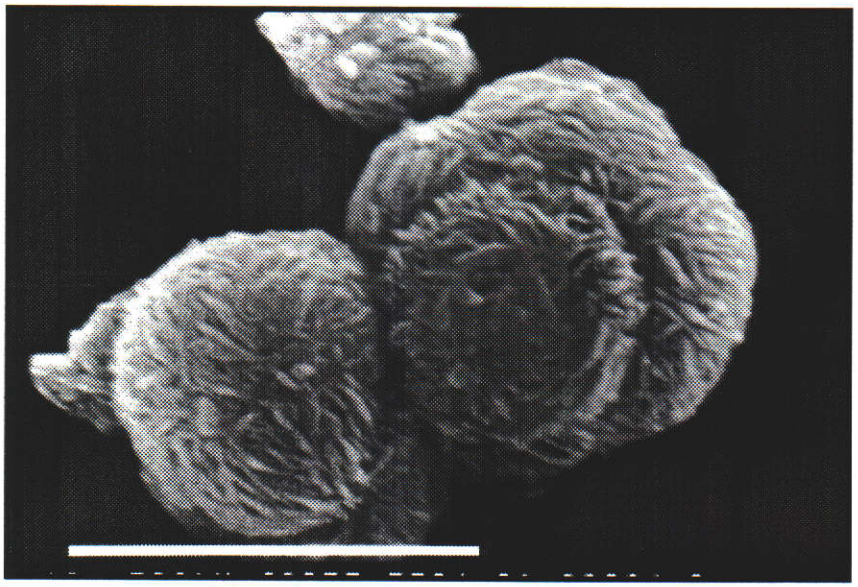

Figure 2.9 Precipitate from Sodium Aluminate after 48 Hours at Room Temperature

(Scale Bar = 10 μm)

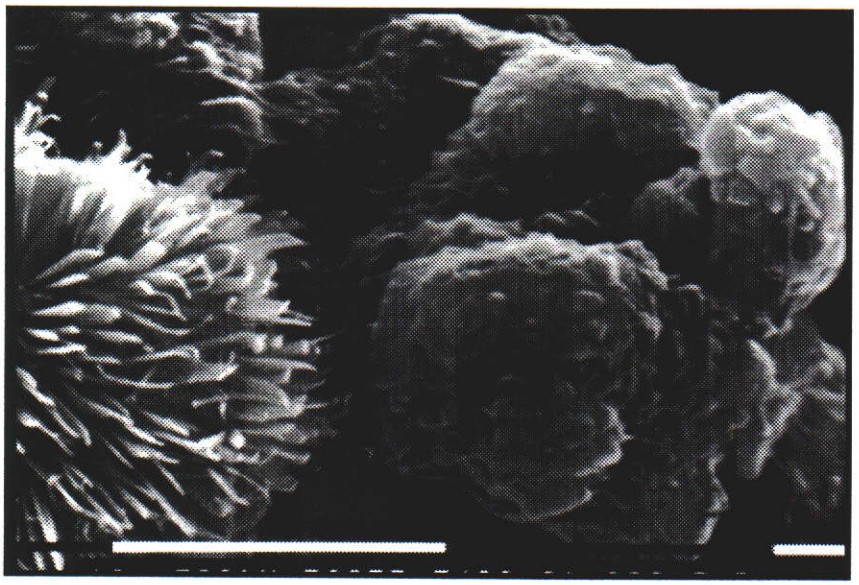

Figure 2.10 Bayerite from Carbonation of Sodium Aluminate Solutions

(Scale Bar = 10 μm)

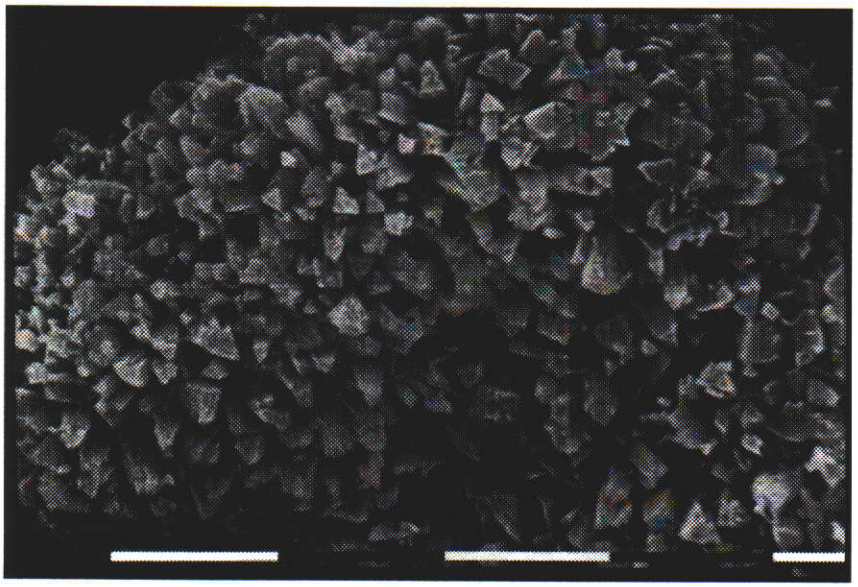

Figure 2.11 Bayerite with Radial Growth Characteristics (Scale Bar = 10 μm)

2.3.2.2 From Potassium Aluminate Solutions

The morphology of bayerite formed by ageing potassium aluminate solutions at room temperature consisted of agglomerates of hexagons and diamonds, as well as single crystals of elongated hexagonal prisms (Figure 2.12) These elongated prisms are typical of the morphology of crystals grown from potassium aluminate solutions (Wefers, 1962). On further ageing (up to two weeks) the precipitate formed was identified to be gibbsite, indicating that a very slow transformation of bayerite to gibbsite occurred. This transformation, from bayerite to gibbsite, was not observed with the sodium aluminate solutions after two weeks.

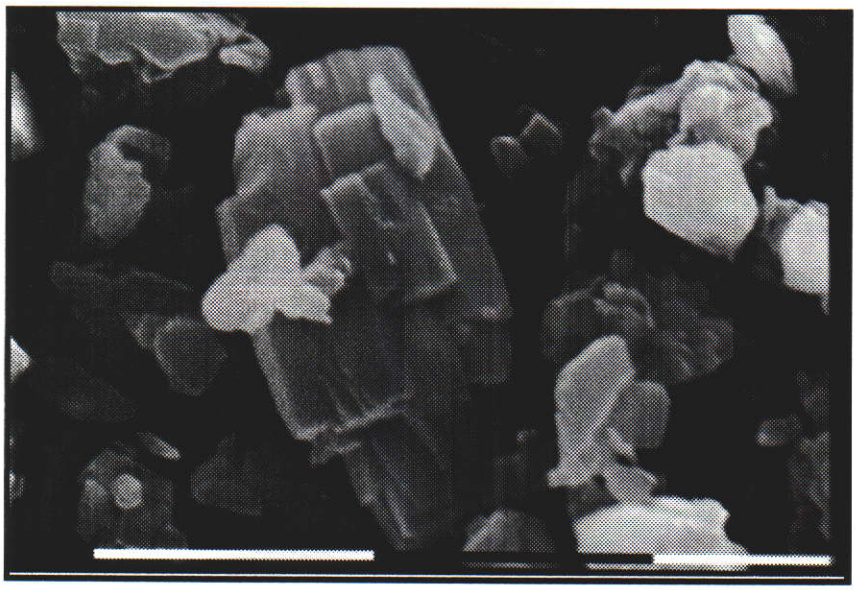

Figure 2.12 Bayerite from Ageing Potassium Aluminate Solutions at Room Temperature (Scale Bar = 100 μm)

The morphologies of the product from the carbonation of potassium aluminate solutions were similar to those produced when using sodium aluminate solutions - agglomerates of fine crystals with some web-like and frond shaped crystals (Figure 2.13) . The slow neutralization of potassium aluminate solutions by addition of acid resulted in the formation of bayerite with two distinct morphologies. The first morphology was comparable to the samples produced from the addition of acid to sodium aluminate; bayerite which consisted of agglomerates of triangular prisms with radial growth characteristics. In addition, bayerite also took the form of single crystals (~40 μm), which sometimes exhibited zig-zag edges (Figure 2.14). The two morphologies have different settling properties, and hence were physically separated into layers on standing. It is unknown whether both morphologies are formed simultaneously, or whether during the slow acid addition, one morphology appears before the other.

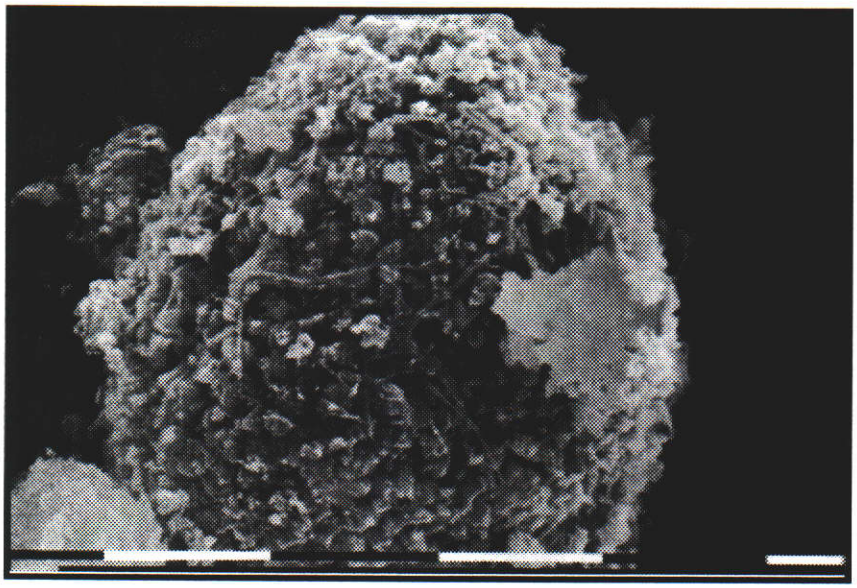

Figure 2.13 Bayerite Formed by Carbonation of Sodium Aluminate at Room Temperature (Scale Bar = 10 μm)

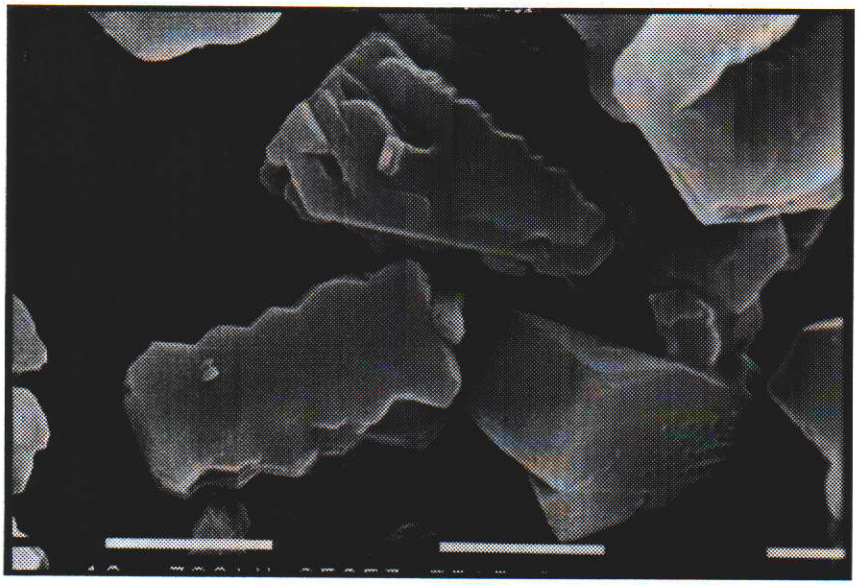

Figure 2.14 Single Crystals of Bayerite with Zig-Zag Edges (Scale Bar = 10 μm)

2.3.3 Gibbsite Formation and its Morphology

2.3.3.1 From Sodium Aluminate Solutions

The morphology of the crystals formed from ageing sodium aluminate solutions at 70°C consisted of agglomerates of hexagonal tablets, as well as diamond shaped crystals, similar to those of natural gibbsite. These were identified by XRD as gibbsite, with some nordstrandite and trace amounts of bayerite.

The carbonation process at 70°C, using the multiple inlet, resulted in the formation of a mixture of bayerite and gibbsite. The morphology of the crystals formed consisted of aggregates of web-like and frond shaped crystals with hexagonal prisms protruding from the web like structures (Figure 2.15).

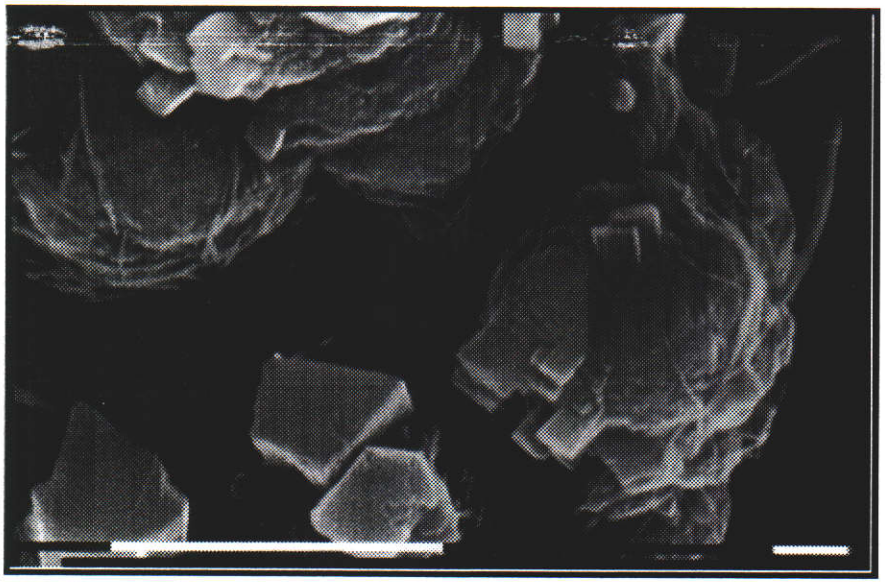

Figure 2.15 Gibbsite/Bayerite from Carbonation of Sodium Aluminate

(Scale Bar = 10 μm)

The addition of hydrochloric acid to sodium aluminate at 70°C resulted in the formation of gibbsite crystals with morphology similar to that of industrially produced gibbsite - agglomerates of hexagonal and diamond shaped crystals, but with finer crystals (Figure 2.16) (Wefers and Misra, 1987).

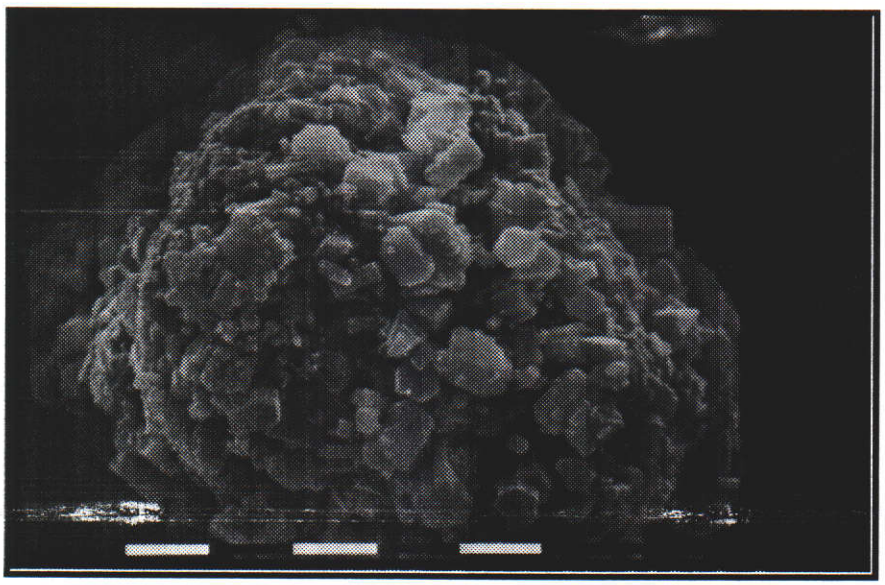

Figure 2.16 Gibbsite from Acid Addition to Sodium Aluminate (Scale Bar = 10 μm)

The seeding of sodium aluminate solutions with gibbsite resulted in the formation of agglomerates of hexagons and diamond shaped crystals (Figure 2.17), as well as the formation of some single crystals of up to 10 μm in diameter. The sub-micron fractions of this sample were used for the determination of Miller indices (see Section 4.1).

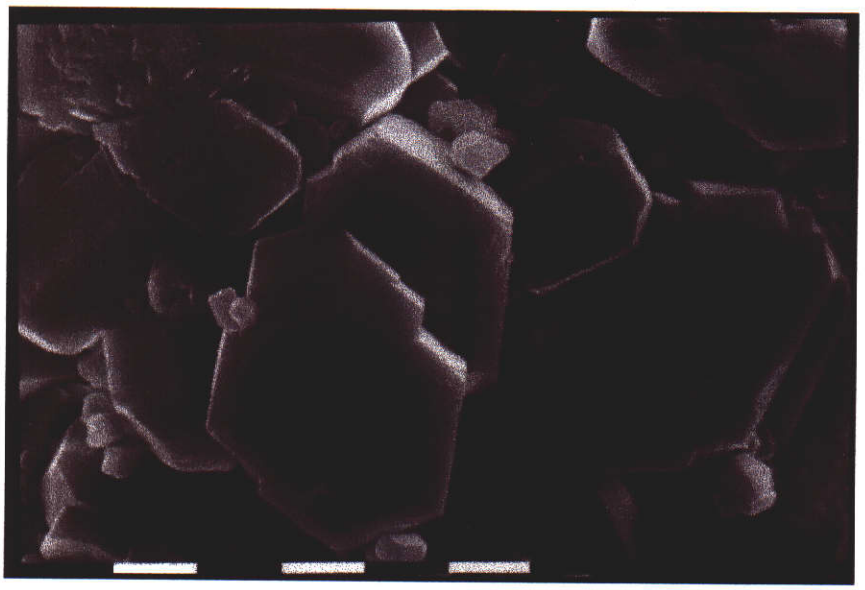

Figure 2.17 Agglomerate of Hexagonal and Diamond Shaped Crystals (Scale Bar = 10 μm)

Seeding the sodium aluminate solutions with woolball bayerite at 70°C resulted in the precipitation of gibbsite. These crystals were agglomerates of rectangular blocks, rather than hexagonal tablets (Figure 2.18). Figure 2.19 gives the XRD pattern of the gibbsite precipitated on the bayerite seed. These patterns show the increase in the relative intensities of the gibbsite peaks ($2\theta = 45.5°, 46.3°$) and the decrease in the bayerite peaks ($2\theta = 40.7°, 53.2°$) with time.

The weakness of the bayerite peaks in the 24 hour sample suggests that either some of the bayerite seed has transformed to gibbsite, or that the bayerite is covered by the precipitated gibbsite. Partial dissolution of these crystals in caustic solution resulted in the separation of the agglomerates, which were subsequently identified by XRD to be mainly gibbsite, with some bayerite. There are two possible reasons for the reduction in the amount of bayerite present. First, the dissolution of the agglomerates could have preferentially dissolved the bayerite, and secondly the bayerite could have transformed to gibbsite. Neither process can be considered proven.

A full quantitative x-ray diffraction analysis of the original crystals formed is required for the determination of the relative amounts of each polymorph present and these results should be compared with the initial amount of bayerite added and the amount of gibbsite precipitated in order to determine if the bayerite has transformed to gibbsite.

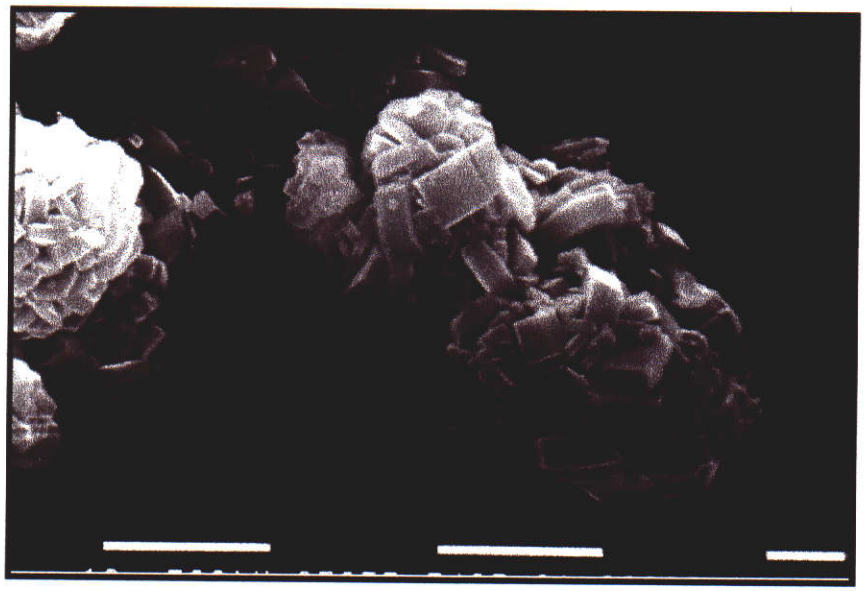

Figure 2.18 Product from Seeding Sodium Aluminate with Bayerite (Scale Bar = 10 μm)

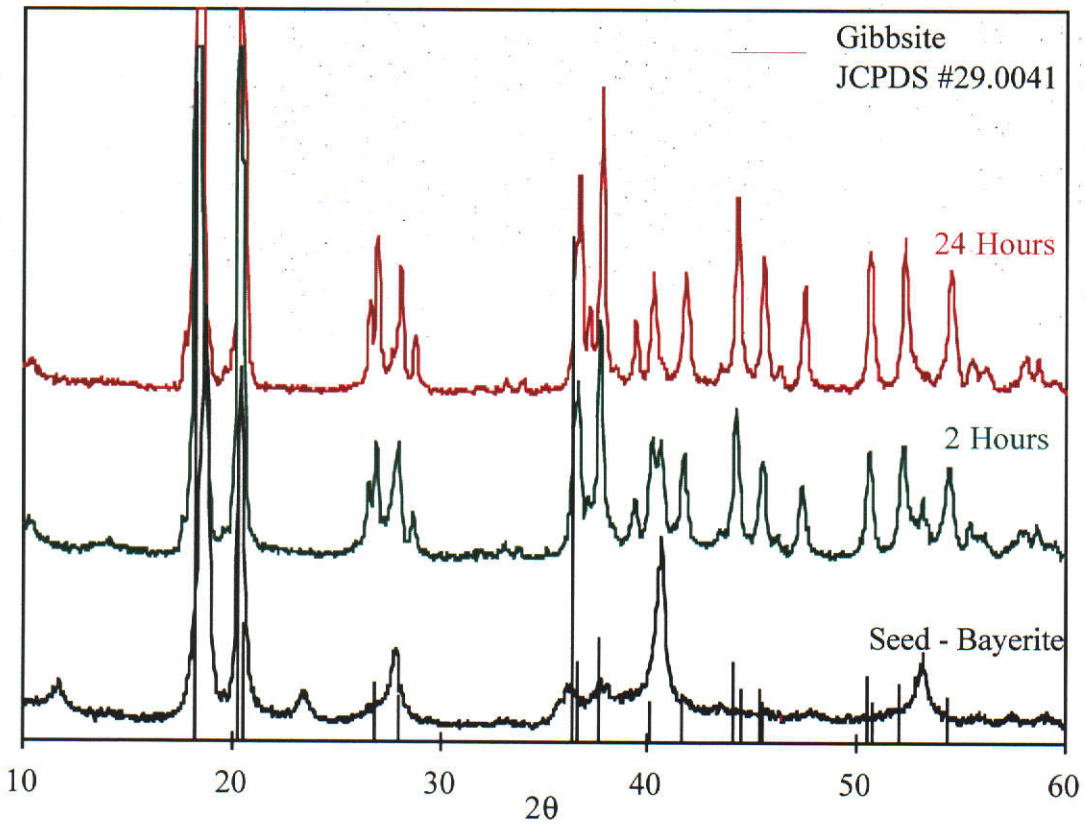

Figure 2.19 XRD Pattern of the Product Obtained When Seeding Sodium Aluminate Solution with Bayerite

2.3.3.2 From Potassium Aluminate Solutions

The morphology of the crystals formed on ageing potassium aluminate solutions at 70°C is similar to that formed from sodium aluminate solutions. The difference being that the crystals are coarser in the potassium aluminate solutions and elongated hexagonal prisms are also present.

The addition of carbon dioxide through the multiple inlet apparatus resulted in the formation of gibbsite and bayerite, while carbonation through the single inlet resulted in the formation of gibbsite only. The morphology of the bayerite/gibbsite crystals consisted of agglomerates of hexagons and elongated prisms (Figure 2.20), while the

gibbsite crystals were relatively large single crystals. These single crystals were elongated hexagonal prisms (Figure 2.21).

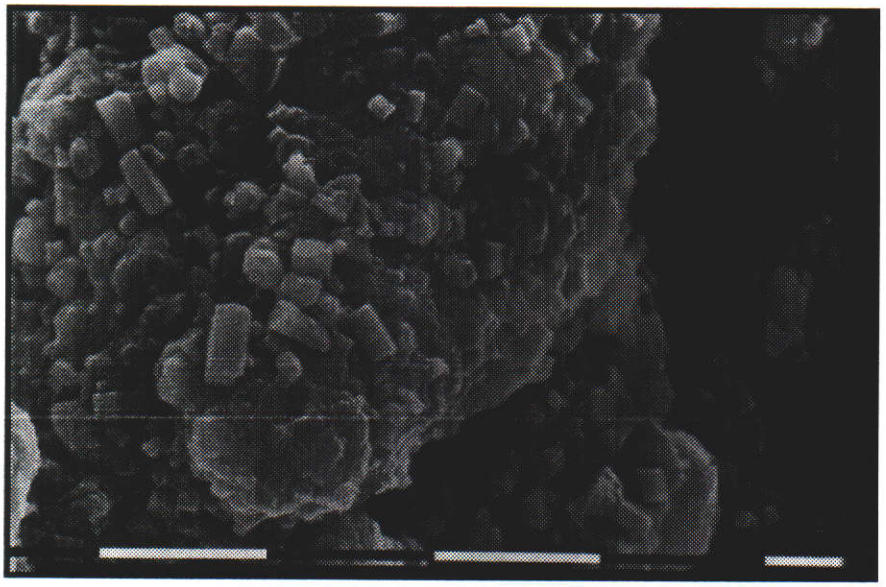

Figure 2.20 Gibbsite and Bayerite from Carbonation of Potassium Aluminate Through Multiple Inlet Apparatus (Scale Bar = 10 μm)

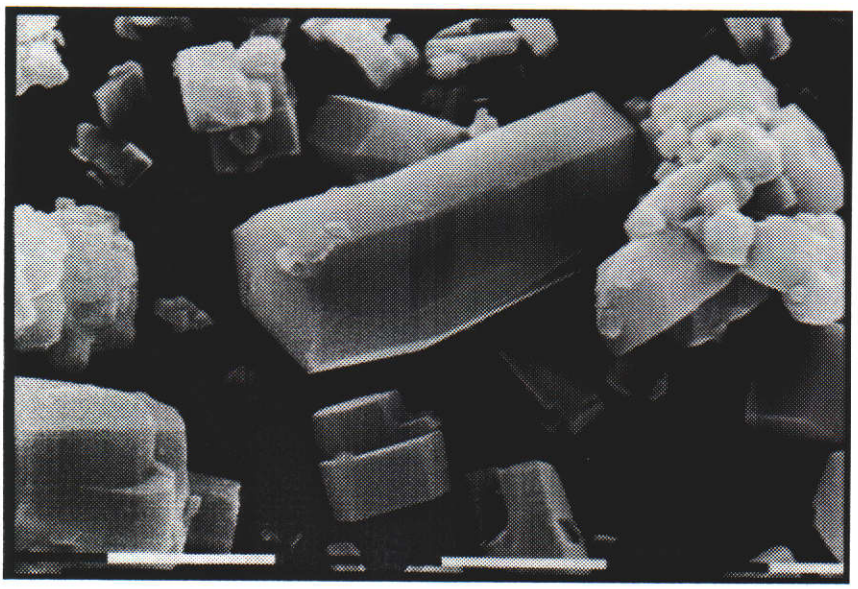

Figure 2.21 Elongated Hexagonal Prism of Gibbsite (Scale Bar = 10 μm)

The resulting difference in the morphologies and phases produced by different preparation methods indicates that the rate of carbonation and agitation play an important role in the formation of the crystals. According to theory, in Ostwald ripening it is possible that in the longer duration of growth using the single inlet compared to multiple inlets, the finer particles dissolved and subsequently recrystallized on the larger particles resulting in the single elongated hexagonal prism observed. Another possible explanation for the difference in morphology and phase formed could be explained using Ostwald's rule of stages. This rule states that the phase which crystallizes is not necessarily the one which is thermodynamically most stable, but the one which crystallizes the fastest. From all the other experiments described in this section, the formation of gibbsite is favoured at the higher temperatures, while the formation of bayerite is favoured at room temperature. Use of the multiple inlet for the carbon dioxide at high temperature resulted in the formation of a mixture of gibbsite and bayerite, implying that although the formation of gibbsite is favoured, bayerite crystallizes faster.

The scope of this section of work, however, is to refine the technique to produce gibbsite and not study the effect of crystallization conditions on the polymorph formed, hence the effect of agitation and carbonation rate on the polymorhs formed were not studied.

The crystals formed by acid addition to potassium aluminate solution were agglomerates of hexagons, diamonds and elongated prisms, similar to those formed from sodium aluminate solutions. Again, coarser crystals resulted from potassium aluminate solutions (Figure 2.22).

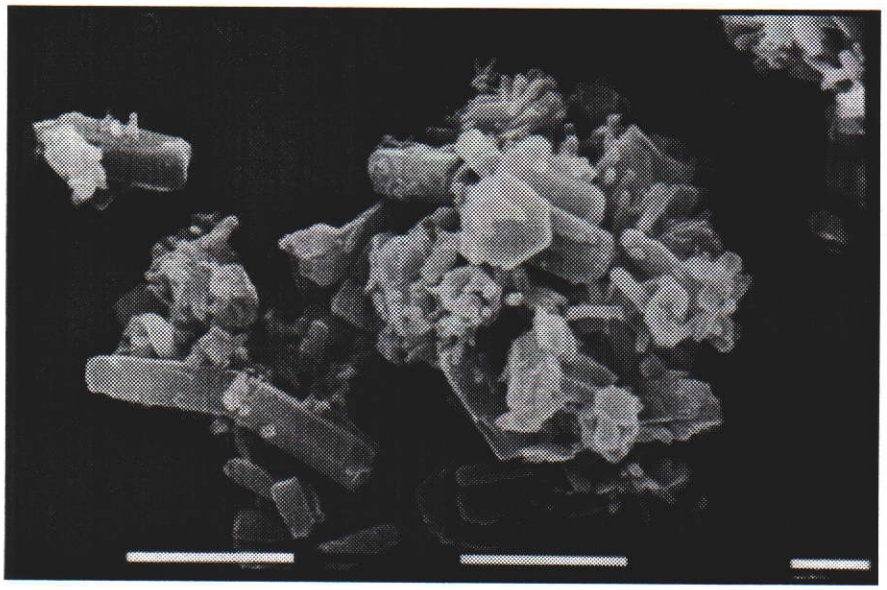

Figure 2.22 Product of Acid Addition to Potassium Aluminate (Scale Bar = 10 μm)

Seeding potassium aluminate solutions with gibbsite or bayerite resulted in the formation of crystals typical for this system - elongated hexagonal prisms of gibbsite of approximately 7 μm.

2.4. Gibbsite Crystal Faces

Crystal faces may be identified by obtaining the electron diffraction patterns from a crystal using a transmission electron microscope (TEM) fitted with a suitable tilting stage. This method, however, requires thin crystals for the penetration of the electron beam, and is thus only suitable only for the identification of the basal and prismatic faces. Identification of the other crystal faces present in the thicker crystals can be done by measuring the angles between two crystal faces (Hirsch *et al.*, 1971). Using the unit cell dimensions reported for gibbsite, the interplanar spacings (d_{hkl}) for any face (h, k, l) can be calculated using Equation 22, and the angle (ϕ) between any two planes (h_1, k_1, l_1) and (h_2, k_2, l_2) can be calculated using

Equation 23. Crystal faces may therefore be identified by comparing the calculated and measured angle between a reference plane and an unknown plane.

$$\frac{1}{d^2_{h\,k\,l}} = \frac{h^2}{a^2 \sin^2 \beta} + \frac{k_2}{b_2} + \frac{l^2}{c^2 \sin^2 \beta} - \frac{2hl \cos \beta}{ac \sin^2 \beta} \qquad (22)$$

$$\cos \phi = d_{h_1 k_1 l_1} \cdot d_{h_2 k_2 l_2} \left(\frac{h_1 h_2}{a^2 \sin^2 \beta} + \frac{k_1 k_2}{b^2} + \frac{l_1 l_2}{c^2 \sin^2 \beta} - \frac{(l_1 h_2 + l_2 h_1) \cos \beta}{ac \sin^2 \beta} \right) \qquad (23)$$

Equations 22 and 23 are valid for monoclinic crystal systems ($\alpha = \gamma = 90°$) with unit cell dimensions a, b and c and where β is the angle between $\underline{a}$ and $\underline{c}$, and d_{hkl} is the interplanar spacing for the (h, k, l) plane.

An optical goniometer may be used if large single crystals are available, otherwise a scanning electron microscope is more suitable.

2.4.1 Transmission Electron Microscopy (TEM)

The crystal faces of hexagonal and diamond shaped gibbsite were indexed by obtaining selected area diffraction patterns. Figure 2.23 shows a hexagon with its [001] zone electron diffraction pattern, showing that the principal prismatic growth faces are (100) and (110). The areas of the (100) and (110) faces in hexagonal crystals are similar. Although the morphology of the diamond shaped crystals matches that of boehmite (Figure 2.4), their electron diffraction patterns confirmed that these crystals are gibbsite with (100) and (110) faces forming the edge of the crystals. In these diamond shaped crystals the (110) faces are dominant, indicating a difference in growth rates between the (100) and the (110) faces. There are more

diamond shaped crystals found in samples precipitated by seeding aluminate solutions than from those produced by ageing the aluminate solutions.

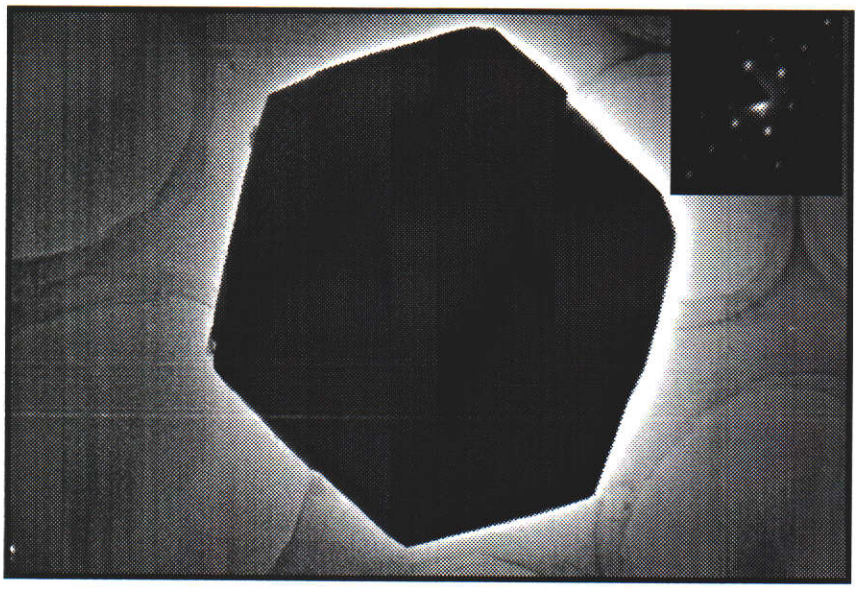

Figure 2.23 Hexagonal Gibbsite Crystal with its [001] Zone Electron Diffraction Pattern

2.4.2 Scanning Electron Microscopy (SEM)

Examination of gibbsite crystals obtained by slow growth showed the presence of other crystal faces as well as those identified by TEM (Figure 2.24). To measure the angle between two planes accurately, the crystals have to be orientated correctly. For example, to obtain the angle between the (110) and (10l) planes, the crystal has to be orientated such that the resulting image is perpendicular to both the (110) and (10l) planes (Figure 2.25), ie. the crystal is viewed along the $[\,\bar{1}\,11\,]$ zone. However, due to the limited tilt and rotation movement available for the sample in the SEM, the crystals chosen are such that only minimal adjustments are required to correctly orient the crystal, which means that the identification of the reference plane is not simple, since the basal plane is not in view.

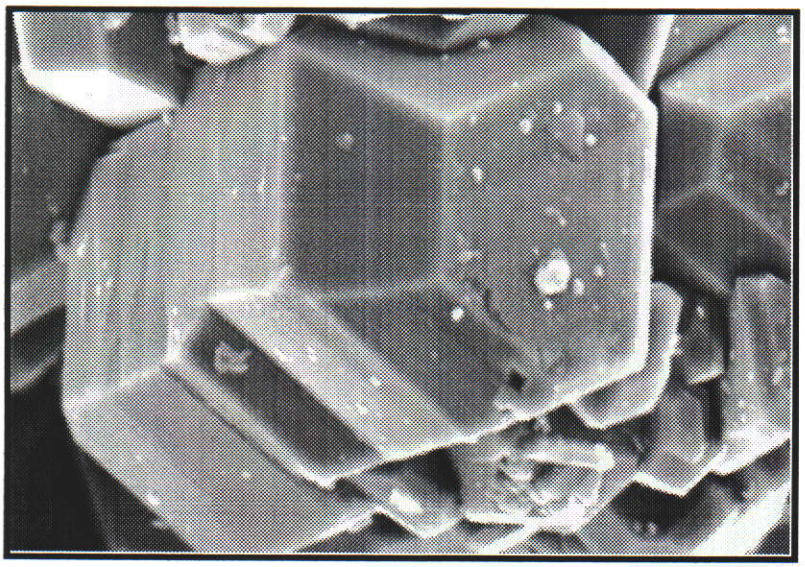

Figure 2.24 Gibbsite Crystal with Chamfered Faces (Full scale = 30 μm)

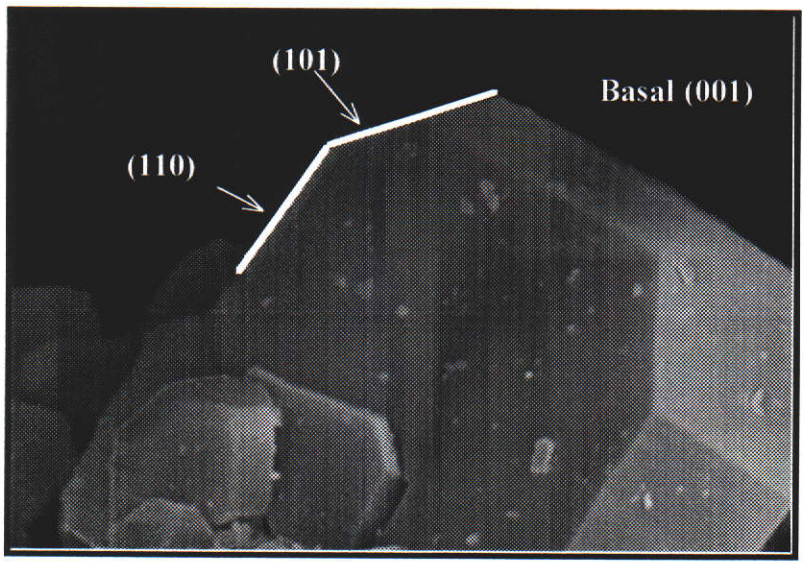

Figure 2.25 Aligning Crystal to Measure the Angle Between (110) and (101)

(Full scale = 30 μm)

Taking this into account, the average value of the angles measured between the prismatic and chamfered faces is 40 ± 2°. The possible identification of the chamfered planes is given in Tables 2.1 and 2.2. From these Tables, it can be concluded that the chamfered faces are the (101) and (112) planes at the top of the (100) and (110) faces, respectively.

Table 2. 1 Calculated Angle Between {200} and {20l}

Reference Plane ($h_1k_1l_1$)	{200}	
$d_{1(200)}$	4.3284	
Possible Planes ($h_2k_2l_2$)	d_2	Calculated Angle (ϕ°)
{201}	3.8416	23.2
{202}	***3.1102***	***39.7***
{203}	2.4982	50.3
{204}	2.0485	57.3
{205}	1.7210	62.1

Table 2. 2 Calculated Angle Between {110} and {10l}

Reference Plane ($h_1k_1l_1$)	{110}	
$d_{1(110)}$	4.3800	
Possible Planes ($h_2k_2l_2$)	d_2	Calculated Angle (ϕ°)
{111}	3.9337	23.9
{112}	***3.1886***	***41.0***
{113}	2.5539	52.1
{114}	2.0873	59.3
{115}	1.7489	64.2

2.5. Summary

Bayerite was the predominant phase formed at room temperature from alkaline aluminate solutions, while the formation of gibbsite was favourable at higher temperatures. Nordstrandite was detected in samples prepared by ageing the aluminate solutions at high temperatures, and trace amounts of bayerite was also detected in the ageing of sodium aluminate solutions at high temperatures. In samples prepared using the carbonation process, bayerite and gibbsite were formed at 70°C when a multiple carbon dioxide inlet was used, while only gibbsite was formed when a single inlet was used.

The morphology of the bayerite formed depended on the method used, ranging from well formed aggregates of fine crystals to agglomerates of hexagonal and diamond

shaped crystals, as well as single crystals. None of these observed morphologies of bayerite formed from caustic aluminate solutions matched the somatoids cited in the literature (Wefers and Misra, 1987).

The neutralization of aluminate solutions by either mineral acid or carbon dioxide addition resulted in several morphologies. If the rates of neutralization are compared, then carbon dioxide is faster than the addition of mineral acid, which results in the formation of fine crystals. Carrying out the carbonation reaction at 70°C resulted in the formation of a mixed precipitate of bayerite and gibbsite, with gibbsite being the dominant form. The effect of the rate of neutralization was again seen when a single inlet was used, resulting in the formation of relatively large single crystals of gibbsite from potassium aluminate solutions.

Although the morphology of gibbsite varies with the crystallization conditions, the crystals are generally agglomerates of hexagons and/or diamonds or single crystals of hexagonal plates from sodium aluminate solutions, and single crystals of elongated hexagonal prisms from potassium aluminate solutions. The observed gibbsite crystal faces have been identified as (110) and (100) prismatic edges and (001) basal face. This is in agreement with the crystal faces identified in the literature (Deer, Howie and Zussman, 1977). In some cases, the presence of (112) and (101) faces were also identified. The principal difference between the hexagonal plate-like crystals precipitated from sodium aluminate and the elongated prisms precipitated from potassium aluminate solutions is in their relative length along the c - axis.

The different morphologies of gibbsite crystals grown from sodium and potassium aluminate solutions, under otherwise identical conditions, suggest that the alkali metal plays an important role in the crystallization mechanism. The morphological

difference observed between the gibbsite precipitated from sodium aluminate solutions and potassium aluminate solutions will be discussed in detail in Chapter 3.

From aqueous media, ageing amalgamated aluminium in water at room temperature resulted in the formation of bayerite while ageing amalgamated aluminium in aqueous ethylenediamine at room temperature resulted in the formation of nordstrandite. Based on the experiments carried out using alkaline aluminate solutions, where gibbsite was the major product formed at 80°C and bayerite the major product formed at room temperature, the formation of gibbsite is expected when amalgamated aluminium is aged in water at 80°C. However, experimentally ageing amalgamated aluminium in water at 80°C resulted in the formation of a gelatinous product, which was identified to be pseudo-boehmite by its X-ray diffraction pattern. This suggest that either the cation, for example sodium, or the anion hydroxyl plays an important role in the formation of gibbsite.

Chapter 3

The Morphology of Gibbsite

3.1. Introduction

The morphology of natural gibbsite crystals is pseudohexagonal tabular, while gibbsite precipitated in the Bayer process forms agglomerates of hexagonal and diamond shaped crystals (Wefers and Misra, 1987). According to Wefers and Misra, elongated hexagonal prisms of gibbsite can be formed from sodium aluminate solutions under low supersaturation and high temperatures. In Chapter 2, the different forms of aluminium trihydroxides precipitated under a variety of conditions were studied. Although slight differences were observed with precipitating conditions, the morphologies of gibbsite were found to be affected mainly by the type of aluminate solutions used. This Chapter investigates the effect of the incorporation of alkali metal ions and the adsorption of organic compounds on the morphology of gibbsite.

3.2. The Effect of Metal Ion Incorporation

The crystallization of gibbsite is surface reaction controlled (Grocott and Rosenberg, 1988). Grocott and Rosenberg (1988) proposed that the rate limiting step involves the restructuring of tetrahedral aluminate ions at the seed crystal surface into more ordered species, formed by the combination of aluminate ions. The formation of these aluminate species requires the release of sodium and hydroxide ions to formed aluminium hydroxide ($Al(OH)_3$). These (Na^+ and OH^-) may become trapped and hence incorporated into the gibbsite lattice. The influence of different alkali ions on the morphology of gibbsite is experimentally investigated in this section of the work and compared to the computationally generated morphology.

3.2.1 Experimental

The aluminate solutions were prepared using gibbsite (C31; Alcoa Chemical Division, Arkansas) and sodium hydroxide pellets (BDH, AnalaR) for sodium aluminate solutions; or with potassium hydroxide for potassium aluminate solution. The solutions were prepared by the method described in Section 2.2.2.1.2 and filtered through a 0.45 μm membrane prior to use. Lithium aluminate solutions and caesium aluminate solutions were prepared by dissolving aluminium wire (BDH AnalaR, 99.9% purity) in hot lithium or caesium hydroxide solutions (100°C). These solutions were also filtered through a 0.45 μm membrane prior to use.

Precipitates were produced by allowing the aluminate solutions to age for 24 hours at 70°C. The precipitate from each experiment was collected and treated as previously described in Section 2.2.2.2. Inductively coupled plasma (ICP) analysis was used to determine the level of cation incorporation in the crystals.

3.1.2 Molecular Modelling

3.1.2.1 Derivation of Potentials

3.1.2.1.1 Bonded Interactions

Force fields consist of two major components: bonded interactions and non-bonded interactions (Grant and Richards, 1995). The bonded term takes into account the interactions between atoms that are chemically bonded and hence involves the bond length (E_ℓ), bond angle (E_θ) and dihedral angle (E_ω) while the non-bonded interactions (E_{nb}) takes into account the electrostatic and short-range repulsive and attractive forces. The energy of a molecule (E_{tot}) is calculated to be the sum of these interactions, as given by Equation 24 (Grant and Richards, 1995).

$$E_{tot} = E_{\ell} + E_{\theta} + E_{\omega} + E_{nb} \quad (24)$$

When considering the bond length, the bond energy results from the stretch and compression of the bond. This vibrational behaviour is near harmonic at close to its equilibrium value, but shows dissociation at longer bond lengths. The potential used to account for bond lengths is described with a simple harmonic function or a Morse potential, as given by Equation 25 (Grant and Richards, 1995).

$$E_{\ell} = D_e \left\{1 - exp\left[-\alpha\left(\ell - \ell_o\right)\right]\right\}^2 \quad (25)$$

where

D_e = *Depth of potential minimum*

α = *curvature around miniumum*

$= \omega\left(\mu / 2 D_e\right)^{\frac{1}{2}}$ *(from spectroscopy)*

ω = *Oscillation frequency*

μ = *Effective molecule mass*

ℓ & ℓ_0 = *Bond length and equilibrium bond len*

The bond angle component of the total energy (E_{θ}) is due to the bending of a bond and can also be treated by using a simple harmonic function. The energy due to the deviation in the equilibrium bond angle is also known as the three body potential (Grant and Richards, 1995).

The torsional or dihedral angle energy (E_{ω}) accounts for bond rotation and considers energies for the eclipsed and staggered conformation of the molecules. This potential is also known as the four body potential.

Three and four body potentials are not applicable to the development of a gibbsite potential model as only the hydroxide groups are considered to be covalently bonded.

3.1.2.1.2 Non-Bonded Interactions

The non bonded interactions (E_{nb}) are distance-dependent and include van der Waals forces (E_{vdw}) and electrostatic interactions (E_{el}) of atoms (Equation 26).

$$E_{nb} = E_{vdw} + E_{el} \tag{26}$$

Van der Waals forces consist of a size dependent term for short distances (Pauli repulsion) between atoms, while at longer distances attraction due to electron correlation as a result of instantaneous dipole interactions predominates. These can be described by the Lennard Jones or Buckingham potentials. The expression for the Buckingham potential to describe the short range interactions between ions is given by Equation 27.

$$E_{short\ range} = \sum_{ij} A_{ij}\ exp\left(-r_{ij}/\rho_{ij}\right) - C/r_{ij}^{6}$$

where

A *and* ρ = *Repulsive interactions* (27)

C = *Dispersive interactions*

r_{ij} = *Distance between atom i and atom j*

Electrostatic energy takes into account the interactions between charges (q) on the atom centres using Coulomb's law (Equation 28). The value of the dielectric constant (D) is unity or a value of one appropriate for the solvent or is made proportional to the distance (r_{ij}) between the charges. It is set to unity in the calculations reported here.

$$E_{el} = \sum \frac{q_i q_j}{D\, r_{ij}} \qquad (28)$$

where

q_i = *Partial charge of atom i*

q_j = *Partial charge of atom j*

D = *Dielectric constant*

r_{ij} = *Distance between atom i and atom j*

Atomic polarization can be modelled by a shell model potential which represents the ions by a pair of point charges, a positive core and massless negative shell, connected by a harmonic spring (Dick and Overhauser, 1958). Since all short range repulsion and attraction is caused by electron repulsion, all short range interactions are defined between the shells rather than the core.

The expression for the core-shell interaction is given as Equation 29.

$$E_{core\text{-}shell} = \sum_i k_i r_i^2$$

$$\text{where } r_i = \textit{Distance between the } i^{th} \textit{ core and its shell} \qquad (29)$$

$$k = \textit{Core shell spring constant}$$

The Morse potential has been used by Jackson and Catlow (1988) to describe the interactions between O and H ions of hydroxyl groups.

All energies in this work are calculated using interatomic potentials based on a formal charge description of the electrostatic interactions (except hydroxyl groups which are treated as covalent) combined with a shell model (Dick and Overhauser, 1958) to describe oxygen ion polarization. The potential parameters were refined to reproduce the structure of bayerite and to yield correct hydroxyl stretching frequencies. Fitting to bayerite rather than gibbsite was done for two reasons: the hydrogen positions in gibbsite are not accurately known, and a good potential model should be applicable to all polymorphs of a compound.

The potential model used was developed by Dr J. D. Gale; Imperial College of Science, Engineering and Medicine, University of London and is given in Table 3.1

Table 3.1 Gibbsite Potentials (O(s) - Oxygen shell; O(c) - Oxygen core)

Buckingham Potential			
Species	A (eV)	ρ (Å)	C (eV.Å.10^6)
Al-O(s)	1360.0	0.29912	0.000
O(s)-O(s)	22764.3	0.14900	27.880
H-O(s)	262.2765	0.26846	0.000
Morse Potential			
Species	D_e	α	ℓ_o
H-O(s)	5.53900	3.11006	0.97979
Coulomb Potential			
No electrostatic interactions within hydroxyl groups			
Core Shell Spring Constant			
Species	k (eVÅ^{-2})	q_{core}	q_{shell}
O	74.920	0.8690	-2.8690

3.1.2.2 Morphology Prediction

Two methods are commonly used to calculate ideal morphologies, whilst ignoring the effects of additives and solvent. The first method predicts what is called the equilibrium morphology, and is based on the calculation of surface energies. Surface

energy is defined as the difference in energy of the surface ions compared to those in the bulk per unit surface area. At equilibrium, a crystal will minimize its total surface energy for a given volume, and thus the importance of a crystal face is inversely proportional to its surface energy. The equilibrium morphology has been found to agree well with small experimentally grown crystals, less than a micron in diameter (Hartman, 1958; Lawrence *et al.*, 1990).

The other method is based on the idea of attachment energy (the energy per molecule released when a new slice of depth d_{hkl} is attached to the growing crystal face). The attachment energy is assumed to be proportional to the growth rate, therefore the smaller (in absolute value) the attachment energy, the lower the growth rate and the more dominant the face will be in the morphology. This morphology is called the growth morphology since it is based on the idea of growth slices attaching themselves to the crystal. This method was developed by Hartman and Perdok to explain the morphology of geological specimens (Rohl and Gay, 1995).

Surface ions tend to move away from their ideal lattice sites (surface relaxation). Most studies on morphology prediction ignore the effects of surface relaxation. Although this is a reasonable approximation for non-polar organic molecules, the same approximation cannot be made for inorganic systems or systems with significant ionic character. The effects of surface relaxation on equilibrium morphologies of α Fe_2O_3 and α Al_2O_3 have been studied by Mackrodt *et al.* (1987). They found the relaxed morphologies to be substantially different from the unrelaxed morphologies. The effect of surface relaxation on growth

morphologies were not studied in these cases but have been determined for zircon, quartz and α-Al_2O_3 by Rohl and Gay (1995).

The morphology derived by the methods discussed can be visualised using a Wulff plot with the growth rate either proportional to either the surface energy or the attachment energy (Wulff, 1901).

3.2.2.2.1 Calculation Methodology

The attachment and surface energies for the twenty planes of gibbsite with the largest interplanar spacings were calculated using the MARVIN surface simulation code (Rohl and Gay, 1995). The calculation utilizes a simulation cell containing two regions. In the first (surface) region, the ions are relaxed such that there is zero force on each of them while in the second region, the ions are fixed (Figure 3.1). This region represents the electrostatic potential of the bulk lattice on the surface region (Rohl and Gay, 1995).

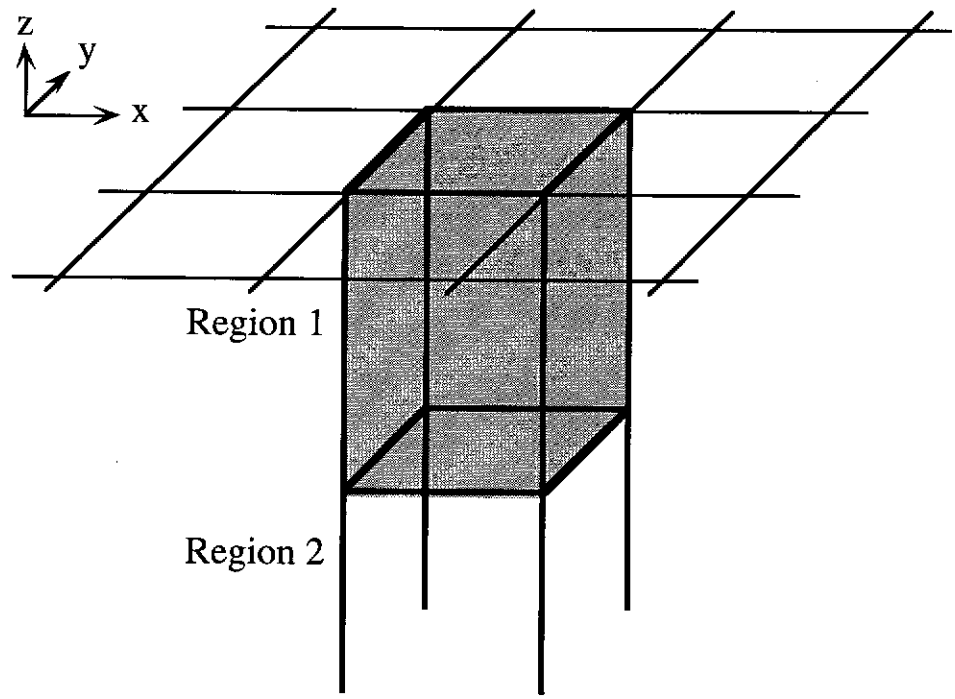

Figure 3.1 Surface Simulation Cell Illustrating the Two Regions: Region 1 Represents the Surface while Region 2 Represents the Bulk Lattice

For each face considered, there may be more than one unique surface configuration and for each of these the unrelaxed surface and attachment energies were calculated. The configurations with the smallest absolute attachment and surface energy were then relaxed to obtain the relaxed attachment and surface energies. The resulting relaxed and unrelaxed attachment energies were used to generate morphologies via the Wulff plot using the InsightII graphic package (Molecular Simulations Inc., San Diego).

3.2.2.3 Incorporation of Defects Calculations

3.2.2.3.1 Bulk Calculations

In this work, the energy for incorporating an alkali metal ion into the gibbsite lattice by substituting the hydrogen atom of a hydroxyl group with a metal cation, leaving an O^{2-} ion at the oxygen site of the hydroxyl group is calculated. This model, where the metal cation replaces a proton in the gibbsite lattice (as suggested by Eremin *et al.*, 1980), allows the defective structure to remain charge neutral.

Computationally, there are two different models for examining the incorporation of defects. The first uses the imposition of periodic boundary conditions, where the alkali metal cation is incorporated in all replications of the unit cell throughout the solid. This represents the situation where there is a finite concentration of defects and the defect level is controlled by the number of foreign ions per unit cell and the size of the supercell. In this work, only a concentration of one ion per unit cell has been considered.

A second approach is to treat an isolated foreign ion substituted into an otherwise perfect crystal using the Mott-Littleton method (Mott-Littleton, 1938). This models the limit of infinite dilution and thus simplifies the problem by removing the need to consider the influence of interaction between defects. Such calculations yield a defect energy for the replacement of hydrogen by an alkali metal ion within the gibbsite interlamellar region.

The potentials used for the defect calculations are the same as those used in the morphology calculations augmented with potentials for the dopant ions derived from their oxide crystal structures and properties. Calculations were performed using the solid state modelling package GULP (Gale, 1992-1995).

The potentials used for the dopants are given in Table 3.2.

Table 3.2 Buckingham Potentials for Dopants Used in Incorporation Calculations

Species	A (eV)	ρ (Å)	C (eV.Å.10^6)
Li - O(s)	541.9436	0.3000	0.000
Na- O(s)	611.0800	0.3530	0.000
K- O(s)	902.7900	0.3698	0.000
Cs - O(s)	1065.3200	0.3911	0.000

3.2.3 Results and Discussion

3.2.3.1 Ageing of Aluminate Solutions

Ageing of sodium aluminate solutions, as described in Section 2.3.2.1, resulted in the formation of gibbsite and nordstrandite, with trace amounts of bayerite. Attempts were made to grow gibbsite from lithium aluminate solutions by the same method, but these resulted in the formation of lithium aluminium hydroxide (Figure 3.2).

The morphology of the crystals formed from aged sodium aluminate solutions is similar to that of those produced industrially by the Bayer process (Wefers and Misra, 1987). Agglomerates of hexagonal tablets, as well as diamond shaped crystals were observed. From the potassium aluminate and caesium aluminate solutions, elongated hexagonal prisms were formed, with the caesium aluminate solutions

producing longer crystals (Figure 3.3 and Figure 3.4). The effect of leached ions from the stainless steel vessel was not investigated, as it was thought that any effect would be insignificant compared to that of the alkali metal ions.

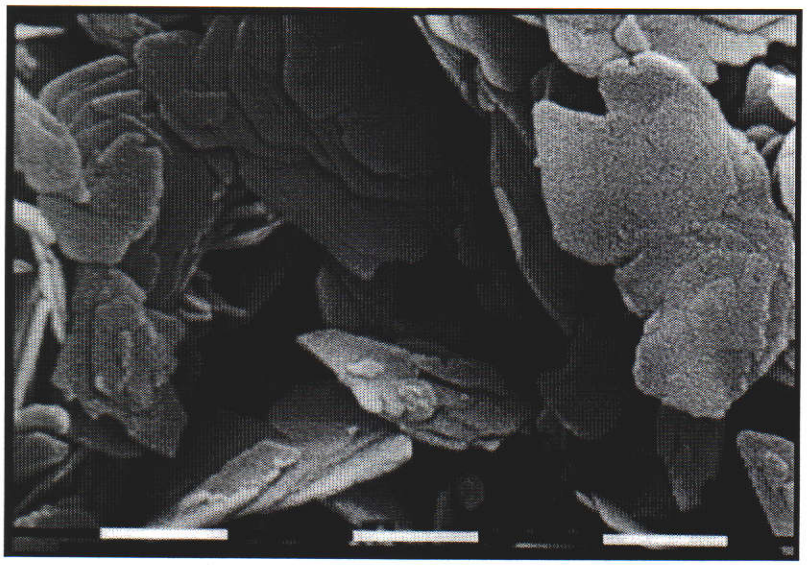

Figure 3.2 Precipitate Collected from Ageing Lithium Aluminate Solution (Scale Bar = 1 μm)

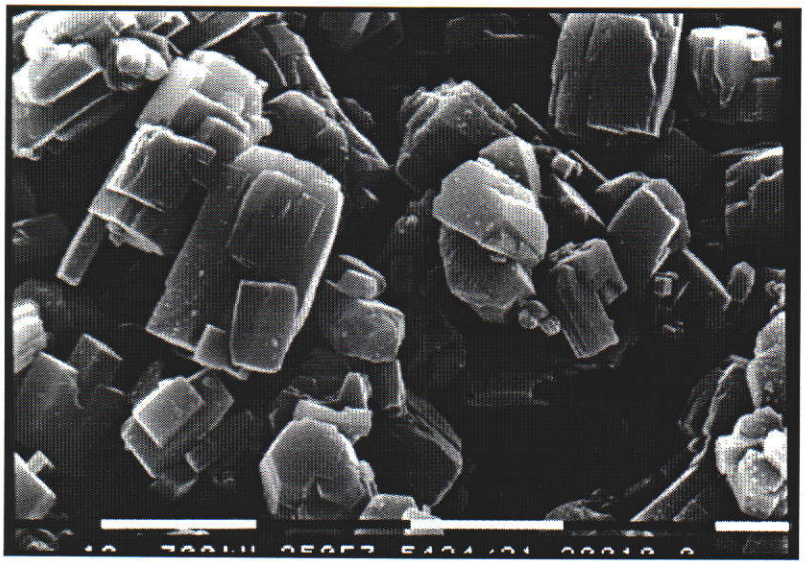

Figure 3.3 Gibbsite Produced from Potassium Aluminate Solution (Scale Bar = 10 μm)

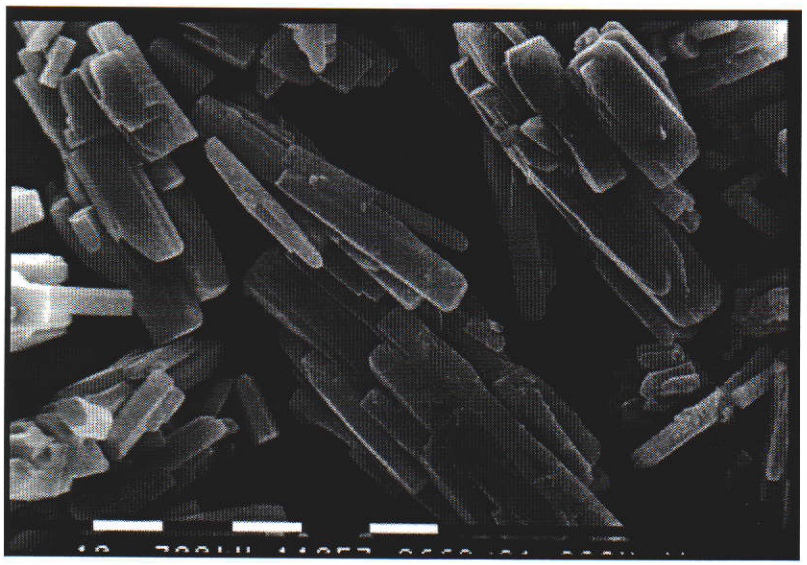

Figure 3.4 Gibbsite Produced from Caesium Aluminate Solution (Scale Bar = 10 μm)

The gibbsite samples precipitated from sodium aluminate, potassium aluminate and caesium aluminate solutions were analysed to determine the level of cation incorporation and the results are summarized in Table 3.3.

Table 3.3 Level of Cation Incorporated into Gibbsite Grown from Different Alkali Aluminate Solutions as Analysed by ICP

Cation	Incorporation (ppm)
Sodium	6700
Potassium	505
Caesium	175

3.1.1.1 Molecular Modelling

The quality of a potential model generated from molecular modeling can be gauged by comparing the experimentally determined crystallographic structure (Figure 3.5a) with the structure calculated from the potentials (Figure 3.5b). These show that the relative aluminium and oxygen positions within the $Al(OH)_3$ layers are very similar in each, but the positions of the hydrogen atoms are modelled less successfully. This is due to the crystallographic structure being determined by its x-ray structure and hence are inaccurate. Since X-rays are scattered by electrons and hydrogen does not have any core electrons, rather it has a single electron over the bond, the bond lengths determined will be too short. Secondly, hydrogen atom has only one electron whereas oxygen has 8 and aluminium has 13, thus the hydrogen atoms does not contribute greatly to the diffraction resulting in the errors.

The hydrogen atoms in Figure 3.5 are numbered in the order that they appear in the asymmetric unit, implying that those with the same number are related by symmetry. In the calculated structure (Figure 3.5bb), the layers slip relative to each other and this is accompanied by an increase in the β angle. In the crystal structure of gibbsite, there are 6 symmetry-independent hydrogen positions. Three of these (numbered 1 to 3 in Figure 3.5 lie in the plane of close packed oxygen layers with the rest lying between the close packed layers. In the calculated structure, the hydrogens labelled 3

have come slightly out of the plane whilst the relative disposition of the $Al(OH)_3$ layers has put hydrogens 4 and 6 in close proximity to each other. It is noted that an accurate experimental location of the hydrogen positions requires a re- determination of the crystal structure by neutron diffraction. However, the increase in the β angle predicted by the potential model is significant and indicates that the potential model can only be used qualitatively.

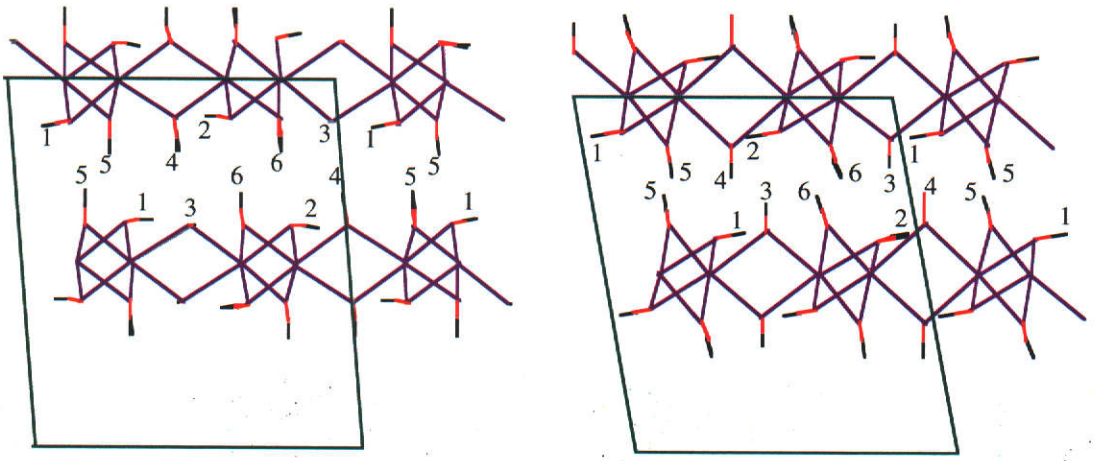

Figure 3.5 (a) The Experimental Gibbsite Structure Determined Crystallographically (b) The Calculated Structure of Gibbsite Using Interatomic Potentials (Purple represents the aluminium, red represents the oxygen and black represents the hydrogen atoms)

3.2.3.3 Calculated Morphology

The predicted equilibrium morphology of gibbsite (Figure 3.6a), is a hexagonal tablet with (001) basal and (101) and (112) faces forming the edges of the crystal. Upon relaxation, the (110) and (100) faces were formed, resulting in (101) and (112) forming chamfered edges (Figure 3.7b). This morphology, (001) basal, (110) and

(100) prismatic and (101) and (112) forming as chamfered edges has been found to exist experimentally, especially in slowly grown crystals from sodium aluminate solutions (see Section 2.4.2).

The growth morphology was predicted to be an elongated hexagonal prism, with a (001) basal face and (110) and (101) prismatic faces (Figure 3.8). Although elongated crystals are also formed from sodium aluminate solutions, the majority of these elongated crystals are diamond shaped crystals. Experimentally, the area of the (100) face is reduced or eliminated by the expansion of the (110) face rather than by replacement with the {101} faces as predicted.

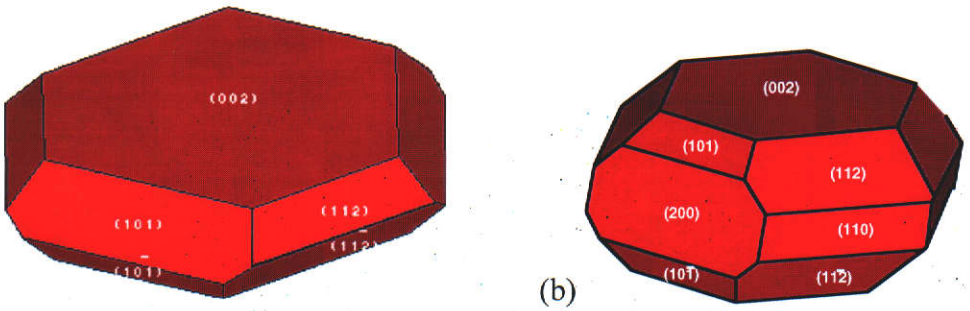

Figure 3.6 Predicted Equilibrium Morphologies of Gibbsite (a) Unrelaxed (b) Relaxed

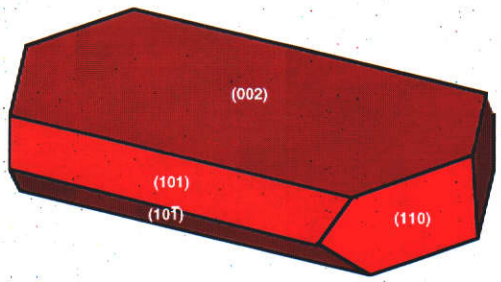

Figure 3.7 Relaxed Growth Morphology of Gibbsite

The calculations suggest that the observed hexagonal plates with chamfered faces have very low sodium content and are grown in near equilibrium conditions. The inability of the calculations to produce the "diamond" morphology suggests that these crystals have a higher concentration of sodium than the hexagonal plates. Difficulties were faced when attempting to quantify, by energy dispersive spectrometry in a scanning electron microscope. This is because of the amount of sodium in each type of crystals. Because of the low levels of sodium in the crystals and the mobility of sodium ions in the electron beam, it is not possible to confirm this proposal experimentally at this stage.

The atomic structures of the basal and the (100) and (110) prismatic faces are given in Figure 3.8. The similarities between the prismatic faces should be noted here, and the significance of this to the results obtained in Section 3.3 and also in Section 5.2.3 will be discussed later.

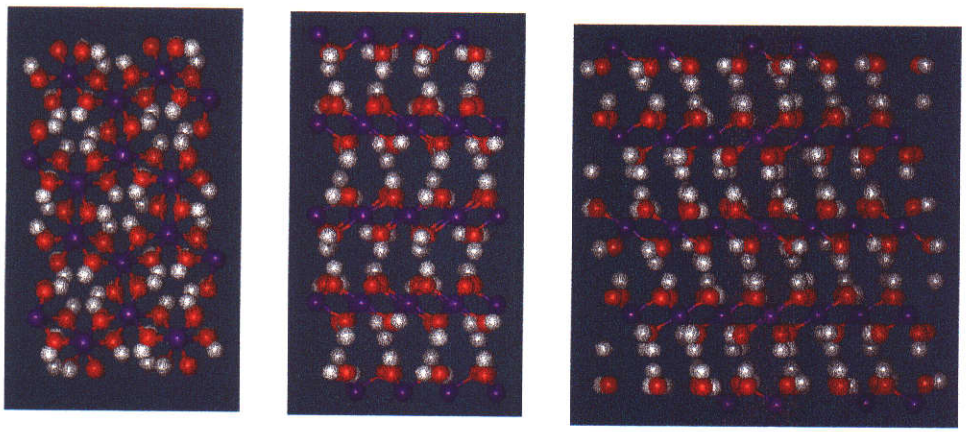

Figure 3.8 Atomic Structure of Gibbsite Crystal Faces Viewed from Above

3.2.3.4 Defect Calculations

3.2.3.4.1 Infinitely Dilute Defects

Calculations replacing each of the six distinct hydrogen sites individually, as labelled in Figure 3.5, with lithium, sodium, potassium and caesium were performed. For all the alkali metals, the most stable site was position 2. The second most stable site was position 1 except in the case of caesium, for which it was position 3. The third most stable was the remaining in-plane hydrogen position (ie. hydrogen in position 3 for sodium and potassium or hydrogen in position 1 for caesium). The defect energies for the incorporation of the alkali metal at position 2 are given in Table 3.4. In order to obtain absolute defect energies, it is necessary to apply a correction for the inconsistency in the O-H dissociation energy as described by the Morse potential in the interatomic potential energy calculations. This correction arises due to the fact that the charges on the ions in the simulation differ from the formal oxidation states at the dissociation limit. Based on an MP2/6-31G** quantum mechanical calculation of the proton affinity of $Al(OH)_4^-$, an estimate has been made of the magnitude of the correction due to this inconsistency and due to the change in short range potential action on the oxygen. Although there will consequently be a degree of uncertainty concerning the absolute defect energies, this will not influence the relative magnitudes for different alkali metal cations.

It is clear that for isolated defect energies that there is an approximately linear increase in the cation substitution energy with ionic radius, with lithium being the most favourable for inclusion. This was accompanied by a linear increase in the largest displacement of ions surrounding the defect. The fact that only lithium has a negative defect energy is significant, as this implies that thermodynamically all of the lithium in the crystallizing solution should be incorporated in the crystal. This was found to be the case as the material grown from lithium aluminate solution was the only one to form a mixed alkali metal/ aluminium hydroxide (see Section 3.2.3.1).

Table 3.4 Defect Energies of Infinitely Dilute Cation Incorporation

Cation	Ionic Radii (Å)	Defect Energy (eV)	Largest Displacement (Å)
Lithium	0.68	-1.71	0.089
Sodium	0.97	1.64	0.125
Potassium	1.33	4.45	0.158
Caesium	1.67	7.66	0.183

The calculated defect energies also explain the ICP analysis results, where the cation incorporation level is inversely related to the defect energies. Thus, caesium which has the largest defect energy has the lowest level of incorporation.

3.2.3.4.2 Periodic Defects

Again, calculations replacing each of the six distinct hydrogen atoms with lithium, sodium, potassium and caesium were performed, and the results are summarised in Table 3.5.

In contrast to the results for infinitely dilute defects, the most stable cation position depends on the alkali metal. Potassium and caesium prefer to be incorporated at a different site to sodium and lithium. The adoption of different sites at large defect concentrations is expected to produce different morphologies, and thus the morphology of gibbsite from sodium aluminate solutions is expected to be different to that obtained from potassium and caesium aluminate solutions. This is in agreement with the experimental observations that sodium aluminate solutions

produce hexagonal plates and diamonds whilst those of potassium and caesium both produce elongated hexagonal prisms (see Section 3.2.3.1). The difference in the morphology of gibbsite observed however, may not be due to the incorporation of the cation into the lattice and other factors need to be considered. First, the aluminate speciation has to be considered. The exact nature of the aluminate ion is not known. However, it is expected that the behaviour of the aluminate ion in a sodium aluminate solution will be different from that in a potassium aluminate solution. Differences may occur due to ion pairing between the aluminate and the cation, and the degree of hydration. The interaction between these aluminate species in solution with the crystal surfaces will therefore be different and can have an effect on the relative growth rates of the crystal faces and hence result in differences in morphology observed. Another factor to be considered is the preferential adsorption of the different cations on the specific crystal faces. This may act to enhance or reduce the growth rate of the crystal face and hence alter the relative growth rates of the crystal faces and the morphology of the crystal.

Table 3.5 Most Stable Cation Position for Periodically Repeated Alkali Metal Defects

Cation	H Position	Lattice Energy (eV)	Δ Volume (%)
Hydrogen		660	
Lithium	2	-665.84	-1.4
Sodium	2	-662.49	4.5
Potassium	3	-661.74	22.1
Caesium	3	-660.66	33.7

3.3. The Effect of Organic Compounds

Various organic compounds have been shown to inhibit the crystallization of gibbsite (Grocott and Rosenberg, 1988). This section of the work investigates the effect of selected organic compounds on the morphology of gibbsite crystals that are precipitated from solutions containing them. Since the crystallization of gibbsite is believed to be a surface controlled mechanism (Grocott and Rosenberg, 1988), organic compounds that selectively inhibit the growth of a particular face can therefore be used as probes for indirectly characterizing the aluminate species in the crystallization process. The observations of changes in morphology due to preferential inhibition of specific crystal faces in the presence of an organic compound implies that parts of the stereochemistry of the organic compound matches the stereochemistry of the aluminate growth unit for that face, hence information about the structure of the aluminate species may be inferred.

3.3.1 Experimental

Organic compounds, dissolved in water, were added to a concentrated solution of sodium aluminate, which had previously been filtered through a 0.45 μm membrane to remove any solid gibbsite. The final liquor composition used in this section of experiments was 0.700 A/C, 200 C, with 10 mmol/L organic. The solutions (200mL) were placed in polypropylene Nalgene bottles and tumbled in a water bath end over end, at 80°C for 95 hours. The precipitates were collected by the method described in Section 2.2.2.2. The organic compounds investigated and their structures will be given in the following section.

3.3.2 Results and Discussion

By quantifying the way in which organic compounds, with different stereochemistry, interfere with the normal mechanism of crystal growth (as evidenced by growth rates, crystal size and crystal morphologies), inferences can be made at the molecular level about processes which occur in the pure system.

Selected organic compounds were examined for their effect on unseeded gibbsite crystallization. XRD analysis confirmed that the precipitate formed was gibbsite in all cases. Comparative data for the effect of these compounds on yield and soda content in seeded precipitation have already been reported (Armstrong, 1993; Grocott and Rosenberg, 1988). The thrust of this work is to characterize their effects on morphology. The addition of certain organic compounds may selectively inhibit the growth of specific crystal faces, thus altering the resultant morphology. It is important to allow for the effects of partial decomposition that may have occurred in some of the molecules during the course of the experiments, as well as the reactions between the molecules in an alkaline media.

The detection and identification of organic compounds in the synthetic Bayer liquor at low concentrations is extremely difficult. To account for decomposition of the organic compound, a systematic experimental procedure is used. For example, a polyol with five carbon atoms may degrade to form another polyol with either three or four carbons. Due to the volatility of methanol and ethanol at high temperatures

(95°C), these were not considered. The effects of adding glycerol, 2,3-butanediol and sodium tartrate on the precipitation of gibbsite were considered as modelling degradation products. Glycerol and 2,3-butanediol were found to have no effect on the precipitation yield and morphology, while sodium tartrate reduced the yield to 90% relative to the control and resulted in the formation of acicular crystals. The effect of sodium tartrate on the morphology of the gibbsite produced will be discussed later in this Section. This implies that unless the organic compounds used in this study degrades to form a compound similar to tartrate, the effects on precipitation yield and crystal morphology observed are due to the addition of that compound are not due to the degradation product.

The concentration of organic molecules used was insufficient to complex all the aluminium in solution. The observation that in the presence of certain molecules some gibbsite crystals grow, whilst others do not, strongly suggests that in the latter case the organic molecules act by binding to specific growth sites and hence reduce the rate of deposition of gibbsite. The reduction in yield observed for all cases implies that it is the inhibition of growth on specific crystal faces that leads to the changes in morphology, rather than an increase in growth on other faces.

The gibbsite crystals precipitated from pure liquor consisted of agglomerates of hexagons and diamond shaped crystals. The crystal faces have been identified to be

(001) basal, (110) and (100) prismatic, with (112) and (101) forming chamfered faces, as reported in Section 2.4.

Initial observations on the reduction in yield confirmed the importance of hydroxyl groups in the organic compounds. This has been demonstrated by examining the phenol group of compounds which are shown in Figure 3.9, along with the yield of gibbsite in the presence of the organic compound at a level of 10 mmol/L. The morphology of the crystals grown in the presence of phenol, resorcinol and hydroquinone were similar to those formed in the control experiment where no organic compound was added. With the addition of catechol, the morphology of the crystals changed to that of single elongated hexagonal prisms, indicating the preferential inhibition of the growth of the (110) and (100) faces. This was accompanied by a 72% reduction in yield. The absence of chamfered faces was also noted on these crystals (Figure 3.10). Some elongated hexagonal prisms were also found in the presence of hydroquinone where a reduction of yield was not observed. The morphological changes observed on some crystals grown in the presence of 10 mmol of hydroquinone suggest that although hydroquinone may act as a selective inhibitor, it is not as powerful as catechol at the same level of dosage.

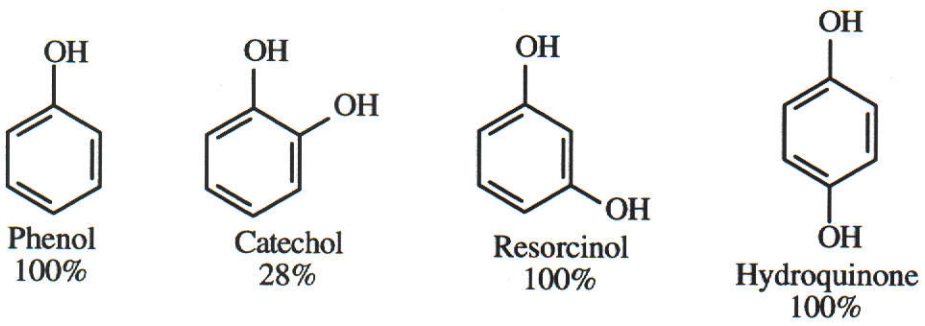

Figure 3.9 Structures of Phenols and their Effect on Gibbsite Precipitation Yield

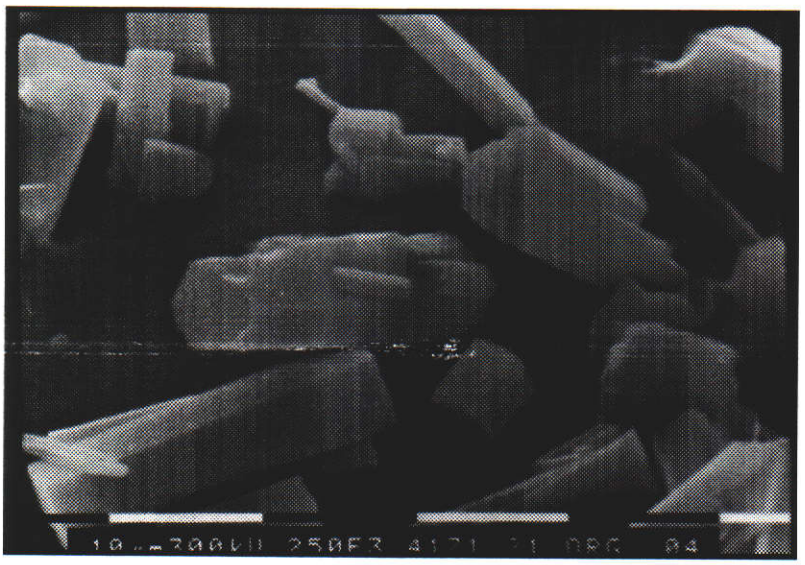

Figure 3.10 Gibbsite Grown in the Presence of Catechol (Scale Bar = 10 μm)

The yield of gibbsite formed as a result of sodium gluconate addition (10 mmol/L) was less than 1% and there were two distinct crystal morphologies obtained from liquors containing this additive. The first morphology indicates the preferential inhibition of the basal face, resulting in the formation of plate like hexagonal crystals (Figure 3.12), while the second morphology indicates the preferential inhibition of the prismatic faces resulting in the formation of acicular crystals (Figure 3.13). Again,

the absence of chamfered faces was noted. The presence of fine hexagonal plates aggregates were also observed in this sample (as seen in Figure 3.12 and Figure 3.13).

The presence of sodium tartrate (10 mmol/L) was found to reduce the yield to 90% relative to the control experiment, and the crystals consisted of elongated hexagonal prisms, with some chamfered faces (Figure 3.14).

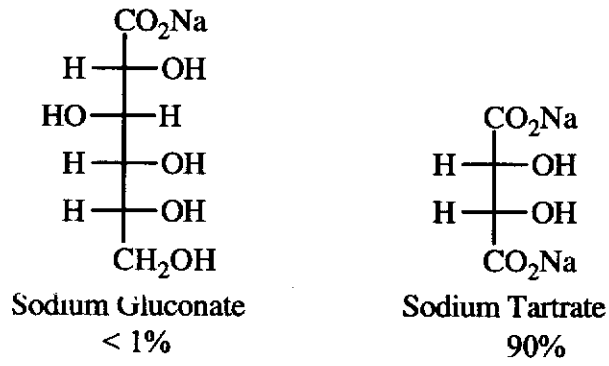

Figure 3.11 Sodium Gluconate and Sodium Tartrate and their Effect on Gibbsite Precipitation Yield

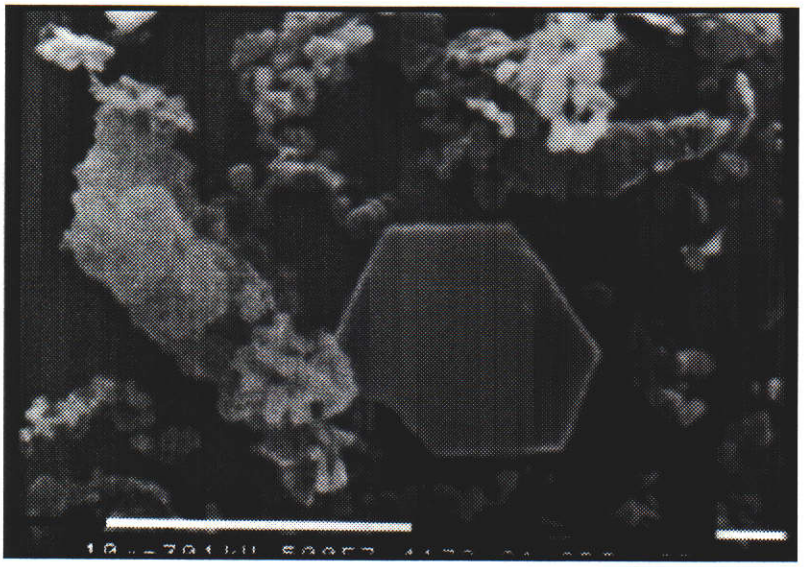

Figure 3.12 Hexagonal Plates formed in the Presence of Sodium Gluconate

(Scale Bar = 10 μm)

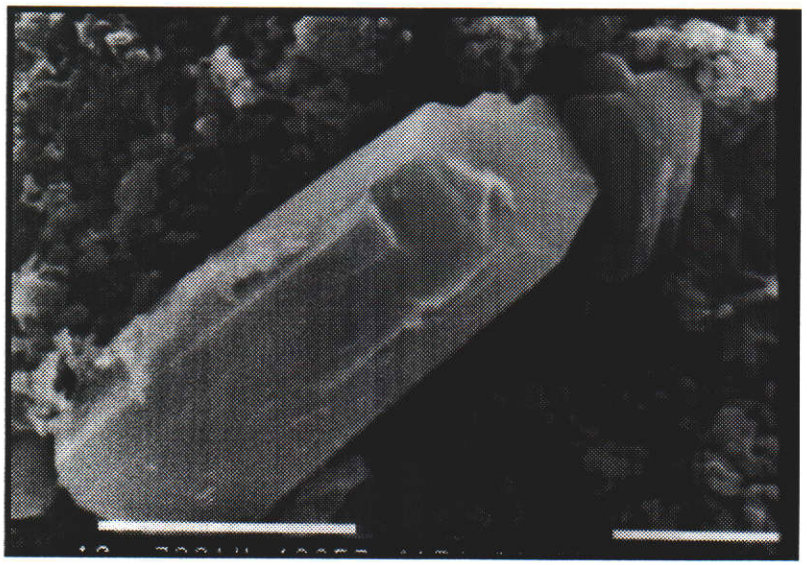

Figure 3.13 Acicular Crystal formed in the Presence of Sodium Gluconate

(Scale Bar = 10 μm)

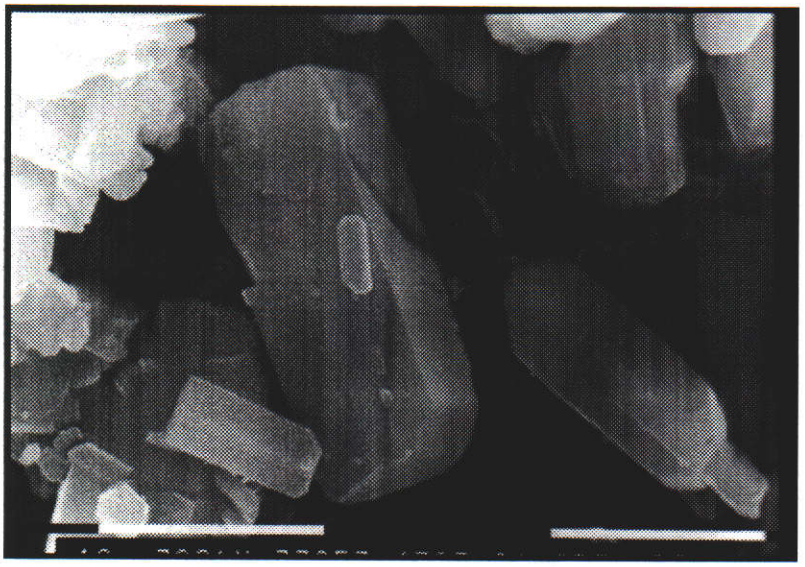

Figure 3.14 Acicular Crystals formed in the Presence of Sodium Tartrate (Scale Bar = 10 μm)

Although the crystals collected from both the sodium gluconate and sodium tartrate experiments had the form of acicular crystals, the average diameter to length ratio of the crystals differed. In the presence of sodium tartrate shorter, but wider crystals were formed with an average aspect ratio (diameter to length ratio) of approximately 0.4, while in the presence of sodium gluconate, the aspect ratio of the crystals formed was 0.3.

Arabinitol and xylitol are two isomers of the group of C5-polyols in which there is a hydroxyl group at every carbon atom (Figure 3.15).

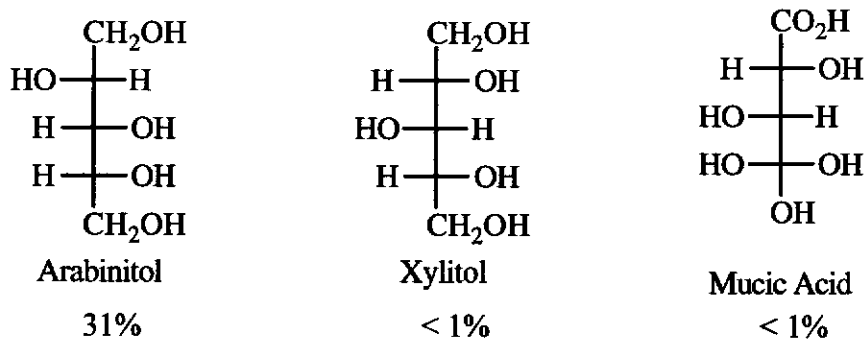

Figure 3.15 Arabinitol and Xylitol. Two Isomers of C5-Polyols and Mucic Acid and their Effect on Gibbsite Precipitation Yield

The addition of 10 mmol/L of arabinitol to the liquor resulted in a yield of 31% and crystals with larger basal faces (Figure 3.16). The an aspect ratio obtained for the crystals grown in the presence of 10 mmol arabinitol is approximately 4, compared to an average aspect ratio of 1 for the control samples. The higher degree of agglomeration was also noted for this sample.

The addition of 10 mmol/L of xylitol produced less than 1% of gibbsite and resulted in the formation of elongated hexagonal needles, with an aspect ratio of approximately 0.1 (Figure 3.17).

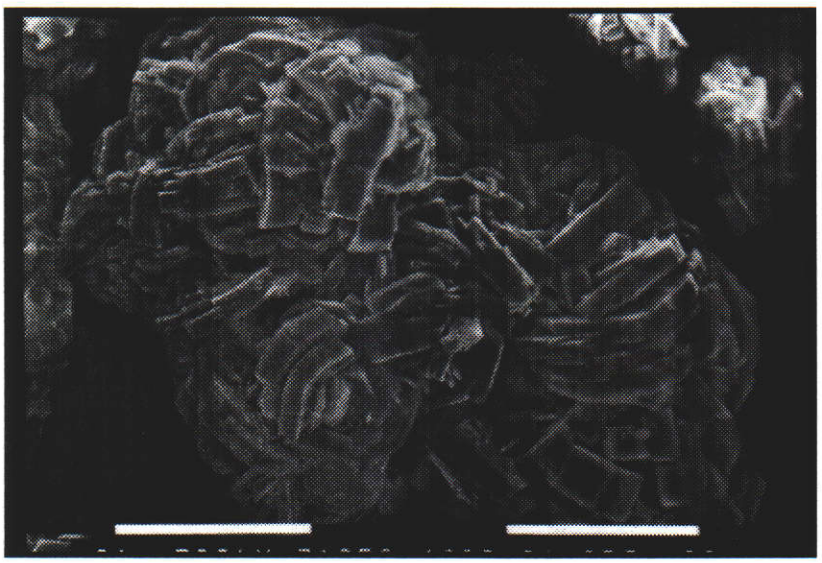

Figure 3.16 Gibbsite Grown in the Presence of Arabinitol (Scale Bar = 0.1 mm)

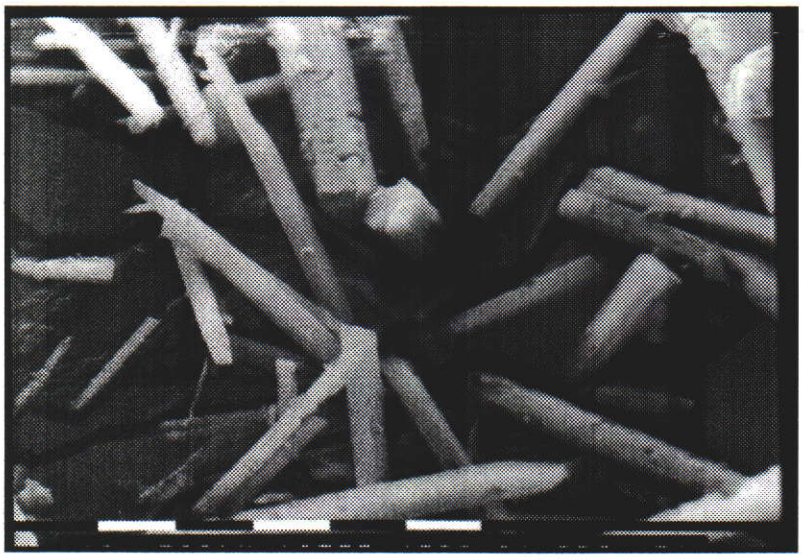

Figure 3.17 Gibbsite Grown in the Presence of Xylitol (Scale Bar = 10 μm)

The importance of stereochemistry is indicated by the different effects induced by the same concentrations of xylitol and arabinitol. The three dimensional structures of xylitol and arabinitol are given in Figure 3.18. These structure have been minimised semi-empirically, using the SPARTAN software. The presence of xylitol has been shown to inhibit the growth of the prismatic faces, while the presence of arabinitol inhibits the growth of the basal face, indicating the preferential adsorption of xylitol and arabinitol on the prismatic faces and basal face, respectively. Inspection of the preferred conformers of these molecules showed the major difference to be arabinitol remaining as a straight chain, while xylitol "curls" onto itself. This is, however the structure of the organic molecules in the absence of solvent and the behaviour of the organic compounds in the presence of the caustic environment needs to be considered before information on the structural compatibility with specific crystal faces can be made.

Other factors such as the distance between hydroxyl groups were considered when attempting to determine which feature of the organic compounds give selectivity towards specific crystal faces. However, similarities between the distances obtained for the hydroxyl groups of arabinitol and xylitol showed the complexity of the system.

(a) 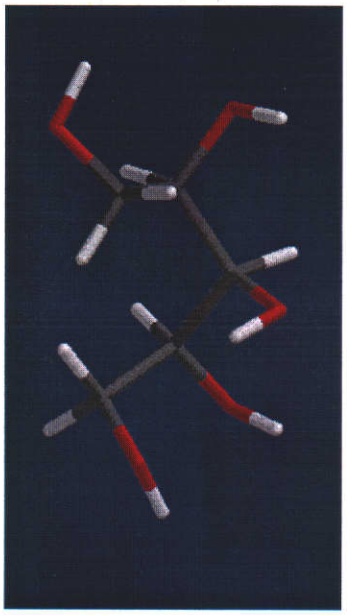 (b) 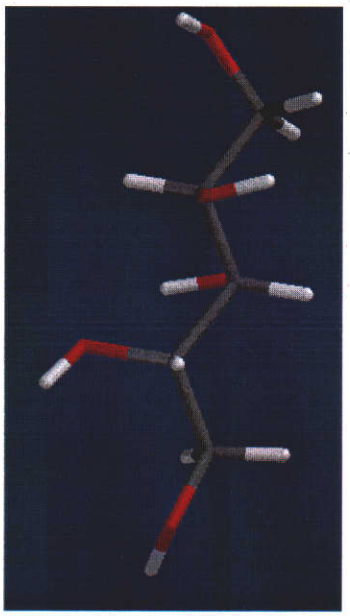

Figure 3.18 Three Dimensional Structures of (a) Xylitol; (b) Arabinitol

The addition of 10 mmol/L of mucic acid, another C5 polyol which combines the structure features of arabinitol and xylitol, in terms of the position of their hydroxyl groups, resulted in the formation of "bow-tie shaped" crystals, where inhibition of both the prismatic and basal faces occurs simultaneously (Figure 3.20).

Figure 3.19 Gibbsite Grown in the Presence of Mucic Acid (Scale Bar = 10 μm)

Comparison of the crystals grown in the presence of mannose, mannitol and mannonic acid (molecular structure in Figure 3.20) showed that although these compounds differed in their ability to reduce the yield of gibbsite, the resulting morphology was acicular in all cases. This supports the theory that the position of the hydroxyl groups is important in their selectivity for specific faces. The different functional groups, such as additional hydroxyl or acidic groups alter the ability of the compounds to be absorbed onto the crystal faces, hence their power as an inhibitor.

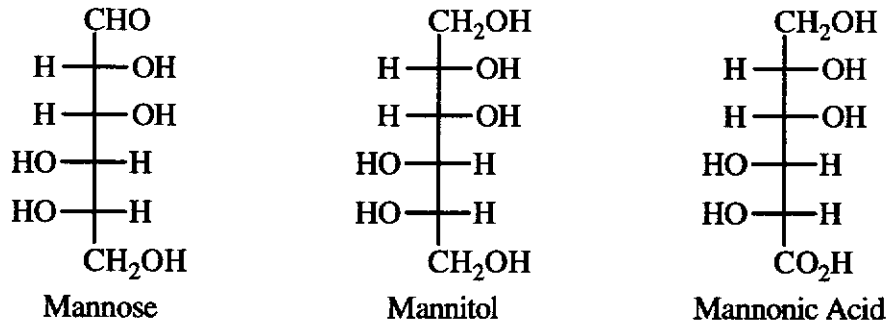

Figure 3.20 Mannose, Mannitol and Mannonic Acid and their Effect on Gibbsite Precipitation Yield

All the organic compounds tested resulted in the formation of one of the three mentioned morphologies: acicular crystals, indicative of selective inhibition of the growth of prismatic faces, thin hexagonal plates, indicative of selective inhibition of the basal face, and blocky hexagons and diamond shaped crystals, similar to those formed in the control experiments, except for mucic acid. The presence of different morphologies in the control sample, such as the diamond shaped crystals, implies that unless very pronounced, the selective inhibition of individual prismatic faces cannot be identified. Furthermore, due to the similarities in the atomic structures of the (100) and (110) faces (as shown in Figure 3.8), selectivity towards an individual prismatic face is not expected.

All the organic additives tested which lead to the formation of acicular crystals also lead to a marked reduction in agglomeration compared to the control sample, while

the formation of large flat crystals, as in the presence of arabinitol, resulted in an increase in the degree of agglomeration about the basal face, indicating the importance of the basal face in the agglomeration process.

With the addition of organic compounds (10 mmol/L) containing nitrogen groups (Figure 3.21), an increase in yield (up to 130%) and the formation of fine crystals (~ 1 μm) (Figure 3.22) were noted. The rate of precipitation was also increased as seen with the presence of visible precipitate after less than 1 hour compared to approximately 2 hours for the control. These compounds are believed to be nucleation promoters, resulting in the rapid formation of nuclei with little or no agglomeration.

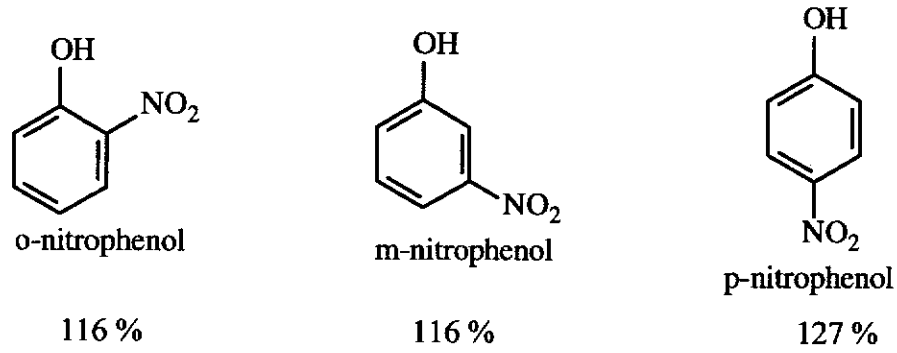

Figure 3.21 Some Nitrogen Containing Compounds Added to Bayer Liquor and their Effect on Gibbsite Precipitation Yield

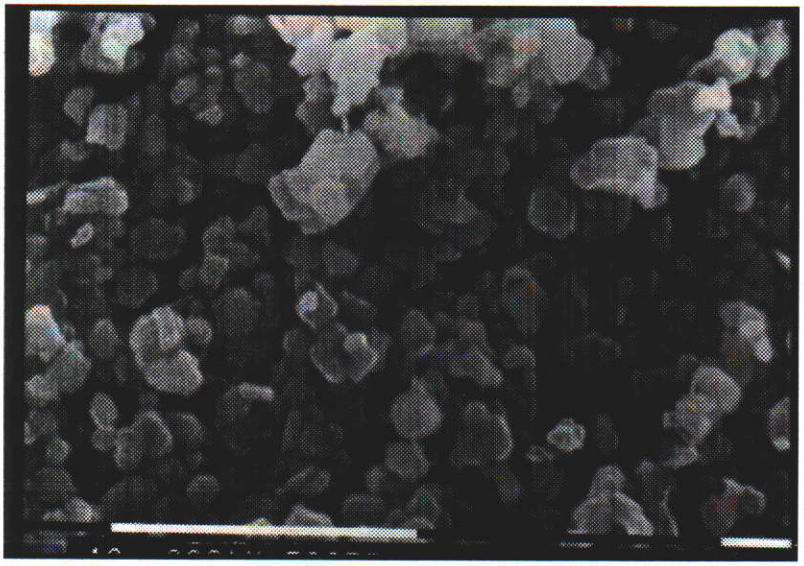

Figure 3.22 Fine Crystals formed in the Presence of O-Nitrophenol

(Scale Bar = 10 μm)

3.3.3 Summary

Although only slight variations can be observed in the morphology of gibbsite as a result of the method of preparation (Chapter 2), the morphology changes may be greatly enhanced by using different alkali aluminate solutions or the addition of organic compounds which can selectively inhibit specific crystal faces.

The effect of different alkali metals on the morphology was determined experimentally and two different morphologies were found, with sodium aluminate solutions producing hexagonal tablets and potassium and caesium aluminate solutions producing elongated hexagonal prisms. The incorporation of the metal ions was also

studied computationally and it was found that the most stable defect site for sodium was different to that for potassium and caesium for a finite defect concentration. Furthermore, the degree of incorporation as measured by ICP was inversely related to the defect energies.

Addition of certain organic compounds may selectively inhibit the growth of specific crystal faces. The importance of stereochemistry has been demonstrated, with the position of hydroxyl groups playing a major role in producing preferential inhibition. The exact nature or stereochemical requirements of an organic compound for its selectivity is not known. To determine the exact stereochemical requirement for selective inhibition, more work is required in determining the exact nature of the organic compounds in the alkaline media. Factors such as the reaction between the organic compound - eg complex ion formation and stereochemistry of the compound in caustic environment needs to be considered.

The preferential inhibition of the prismatic faces over the basal face and the converse preferential inhibition of the basal face over the prismatic faces wereobserved via a change in the morphology of the gibbsite crystals. With the former case, the formation of elongated hexagonal prisms (acicular crystals) occurred, while the latter resulted in the formation of thin hexagonal plates. Selective inhibition between the prismatic faces were not observed. It is believed that this is due to the similarities in the atomic structures of the (100) and (110) faces.

In all cases, with the addition of organic compounds, the absence of the chamfered faces, (101) and (112), was noted in the gibbsite formed. Grocott and Rosenberg

(1988) reported higher levels of sodium found in crystals grown in the presence of organic inhibitors. It is presumed that the absence of these chamfered faces is due to the higher levels of incorporation expected in these crystals. The equilibrium morphology of the gibbsite predicted in the absence of cation incorporation showed the presence of the chamfered faces. Furthermore, the morphology of gibbsite crystals grown slowly, and hence having low sodium, content are hexagonal tablets with chamfered faces, again suggesting that the presence of chamfered faces appears only in crystals with low or no sodium content.

The degree of agglomeration is markedly less when acicular crystals are formed in comparison to hexagonal tablets. These indicate the importance of the basal face in the agglomeration process.

Chapter 4

Assessment of Various Techniques for the Study of Crystal Growth

4.1. Introduction

There are several methods that may be used to study crystallization from solutions, and these methods range in complexity and differ in the type of information they produce. For example, crystallization may be monitored by the desupersaturation rate of the solution, changes in the solid characteristics or both.

One of the simplest crystallization methods involves the use of an agitated thermostated bath containing a large number of identical supersaturated solutions, where the samples may be removed at different time intervals to determine the solution concentration and precipitate characteristics. The solution composition may be determined with any suitable analytical technique, while changes in the particle size may be monitored using particle size determination methods. The mass precipitated is determined by filtering, drying and weighing the solid produced. Mechanistic information on crystal growth may be obtained using electron microscopic techniques (refer to Section 4.2.1). The amount precipitated and changes in the crystal size distribution can be obtained from this type of experiments. This method of studying crystallization offers the benefit of its simplicity and allows a large range of experiments to be carried out simultaneously. However, the simplicity of the technique makes it difficult to control parameters such as agitation, and problems may be encountered with variations between samples.

Studies may also be carried out in laboratory crystallizers. Crystallizers may be operated in a batch, constant composition (where one parameter, for example supersaturation, is kept constant) or continuous mode. Continuous operation is often considered the ideal procedure for simulating refinery conditions, but has its disadvantages such as self seeding, contamination and a long operating time in order to reach steady state (Mullin, 1994). Batch crystallizers offer the advantage of

simplicity, but problems of product variations may be encountered from batch to batch. The problems arising from variations between batches are not as extreme as those faced when using multiple bottles in a thermostated agitated bath.

Crystallization may be monitored by *ex situ*, as well as, *in situ* techniques in a laboratory crystallizer. The simplest method of monitoring crystallization in a crystallizer is by sub-sampling, where a sample is removed periodically to analyse the solution composition and solid characteristics. Provided the removal of sample is small compared to the overall volume of the crystallizer, it is reasonable to consider that the perturbation such sampling introduces to the system is negligible.

In situ techniques for monitoring crystallization includes the use of a conductivity probe, pH electrode or ion selective electrode. Although conductivity measurements require reference to an external *ex situ* analytical method, the probe allows a continuous recording of the desupersaturation of the solution. Conductivity probes, with the support of titrometric techniques have been successfully used to follow the desupersaturation of Bayer liquors during the crystallization of gibbsite (Smith and Woods, 1993). In non-Bayer systems, other methods such as on-line measurements of density have been used. This method of monitoring crystallization of gibbsite is unsuitable since the changes in liquor density are negligible during process.

Synthetic Bayer liquor, as described in Section 1.2.3, is a complex matrix of caustic soda, water and sodium aluminate and the exact nature of the aluminate ion is not clear. It is also highly alkaline with pH in excess of 14. Due to the nature of the aluminate solutions in the Bayer process, pH and ion selective electrodes are unsuitable for monitoring the crystallization process.

In the study of crystal growth from supersaturated solutions, it is insufficient to follow only the solution composition unless the system is well characterised. The structure of a supersaturated solution can be very complex as it may be composed of a variety of units eg atoms, molecules, ions, hydrated solute molecules, dimers, trimers, polymers and clusters. In these cases, it is therefore necessary to monitor simultaneously the actual growth of the crystals, and this may be done by using turbidity measurements and particle size determination methods. Increases in turbidity may be ascribed to increases in particle numbers and/or particle size; although, turbidity is not as sensitive to increases in particle size as it is to changes in to particle numbers. Turbidity has been successfully used in a continuous mode to detect secondary nucleation and its subsequent growth in the Bayer process (Rossiter *et al.*, 1996).

A number of commercial instruments are available for particle size determination. These instruments work on the principle of laser diffraction, sedimentation, light blockage and conductivity. The choice of the instrument used depends on the information required and the nature of the samples.

All the methods discussed so far describe the overall crystallization rate of a system. Although it is possible to control a crystallizer such that predominantly crystal growth occurs, in the gibbsite system it is difficult to eliminate totally nucleation and agglomeration within the system. Furthermore, the techniques described above that measure changes in solution concentration do not differentiate between nucleation, growth and agglomeration (cementation).

The technique of dynamic light scattering (DLS) is based on the variation with time of the intensity of light scattered from particles in suspension. Information on the numbers and diameters of these particles may be obtained by monitoring the

intensity of the scattered light and short term fluctuations in it, respectively. Commercially available DLS systems have been used successfully to analyze a wide range of materials ranging in particle diameter from 5 nm to 5 mm (Nicoli and Elings, 1988). By monitoring particle numbers and particle size simultaneously, observed increases in average particle size whilst particle numbers remain constant may be ascribed to crystal growth. However, if an increase in average particle size is observed with decreasing particle numbers, the increase is particle size is due to agglomeration of particle, while a decrease in average particle size accompanied by an increase in particle numbers is due to nucleation.

The overall rate of crystal growth for a single crystal may be defined as *the average of the rates of displacement of each manifested crystal face in the directions perpendicular to those faces*. From the techniques described above, a crystallization rate may be obtained and the growth rate calculated using existing models. Theoretically, the crystal growth mechanism may be inferred from the relationship between supersaturation and growth rate (see Section 1.3.2). These techniques, however, provide information on the overall growth of the crystal only and not information on the growth of individual crystal faces.

Microscopic techniques have been successfully used for *in situ* and *ex situ* studies of crystallization. An assessment of various microscopic techniques for the study of gibbsite crystal growth is given below.

4.2. Assessment of Microscopy Techniques

Various techniques are examined for their applicability to *in situ* and *ex situ* studies of gibbsite crystal growth, including scanning electron microscopy, environmental

scanning electron microscopy, laser confocal microscopy and optical microscopy. An assessment of each technique is given below.

4.2.1 Electron Microscopes

4.2.1.1 Scanning Electron Microscope (SEM)

Scanning electron microscopes are frequently used for the examination of crystals produced during a crystallization experiment. In the study of gibbsite crystal growth, Brown (1972a, 1972b) obtained mechanistic information using SEM. As a microscopic technique, the SEM offers a high depth of field, high magnification and resolution (0.1 μm), as well as the ability to carry out microanalysis.

Imaging in an SEM is based on sample and beam interactions, which can result in the production of secondary electrons, back scattered electrons, the emission of X-rays and cathodoluminescence from a sample. The interaction between the electron beam and the specimen results in the emission of loosely bound outer orbital electrons (secondary electrons) of low energy. Due to their low energy, only secondary electrons produced near the surface (5 nm) can emerge and thus be detected, and hence contribute to the images. The second way of imaging is based on the elastic scattering of the electron beam, its interaction with the specimen and ultimately emission from the specimen surface. Back scattered electrons are emitted from a greater depth than secondary electrons, but they essentially still produce a signal from the surface (up to several μm deep). The probability of electrons back scattering is closely linked to the mean atomic number per unit volume of the sample. Images obtained by detection of the secondary electrons are more suitable for morphological studies and to obtain surface information, while detection of the back scattered electrons is useful for differentiating the specimen identity when differences in mean atomic numbers exist.

Cathodoluminescence signals are formed when electrons recombine with the holes formed by electron beam interaction, resulting in a radiation of visible, ultraviolet or infrared wavelength. This only occurs for certain classes of materials. In mineralogy, it is a powerful tool, as the intensity of cathodoluminescence can be related to trace element distorting the lattice or variations in thermal histories of different growth stages.

The most essential sample requirements of a sample for SEM are that it is dry and electrically conductive. The addition of a conductive coating is therefore necessary for the examination of most samples.

Traditionally, a SEM operates at a pressure of 10^{-5} - 10^{-6} Torr. It is now possible to operate the instrument at reduced vacuum in the specimen area, at a pressure of up to 1 Torr. Operating in this mode is limited to images from the back scattered electrons, as low energy secondary electrons interact with gas molecules and are effectively absorbed in the higher pressure environment. Furthermore, when using microanalysis facilities, the residual gas scatters the beam over a larger area, hence lowering the spatial resolution. However, the primary advantage is that it is also possible to examine uncoated samples under reduced vacuum.

Brown (1972a, 1972b) has examined the surface of gibbsite crystals during the growth and nucleation processes using a scanning electron microscope. Because of the need for the samples to have a conductive coating, it was not possible to follow the process on the same crystal. Representative samples were obtained from a crystallizer, and they were then washed and dried before characterization of the surface was performed. When employing this technique it is not known what artefacts are introduced during the sub-sampling, washing and drying stages.

In this work, SEM is used as a tool for imaging and general characterization only. Although a conductive coating may not be required, it is still not possible to follow the growth of the same crystal using the SEM due to the requirement for a dry sample. The effects of drying gibbsite seed crystals on crystallization have been studied by Smith and Woods (1993) and it was shown that drying the seed crystals deactivates their surfaces.

4.2.1.2 Environmental Scanning Electron Microscope (ESEM)

The ESEM offers all the benefits of the conventional scanning electron microscope - depth of field, high magnification and resolution, and microanalysis capability, and can operate at pressures ten thousand times higher than that of the standard instrument. This allows the observation of wet or moist specimens without the requirement for a conductive coating.

Imaging with secondary electrons of uncoated samples under the higher pressure in an ESEM is possible due to the Environmental Secondary Detector developed by Danilatos (1988). The detector works on the principle of gas ionization to collect and amplify the signals originating from the beam-specimen interactions. For each electron produced by gas ionization, a positive ion is also generated. Although the positive ions do not contribute to the image signal, they play a very important part in the system by neutralizing the surface build up of electron charge, to which they are automatically drawn by electrostatic attraction.

There are at least three different ways in which the ESEM may be used to study crystallization within a supersaturated solution:

1) Conditions such as humidity or temperature can be changed to induce crystallization. Saturated vapour pressure can be maintained above an aqueous solution within the chamber at a working pressure of 4 Torr only at temperatures below ambient (5-10°C); at higher temperatures, liquid will evaporate. This technique can be used to follow crystallization from simple solutions (eg NaCl) where a solid phase precipitates as the liquor concentrates.

2) Crystallization may be induced by mixing of reactants. In the case of gibbsite, crystallization may be induced by controlled neutralization of the highly alkaline sodium aluminate solutions while maintaining the system at saturated vapour pressure. This method however results in the formation of bayerite rather than gibbsite due to the temperature of the sample chamber (a temperature of greater than 50°C is required for the formation of gibbsite).

However, in both these cases (evaporation and mixing methods) only crystals that appear above the solution meniscus can be imaged; the electrons cannot "see" inside the solution.

3) ESEM allows the examination of wet/moist crystals taken from a crystallizer. This is essentially an *ex situ* technique. However, by mounting the gibbsite crystals on a mesh, and periodic immersion of this into supersaturated solutions, the growth of specific crystals may be observed with time.

4.2.1.2.1 Experimental - Observations of induced crystallization by dehydration

Drops of supersaturated sodium aluminate liquors (0.730 A/C, 200 C, 0.830 C/S) were placed on a glass slide and mounted on the cold stage in the sample chamber. During evacuation of the sample chamber, water vapour was introduced to the

system periodically until a chamber pressure of 4 Torr was achieved. The chamber temperature was then increased from 8°C to 15°C, and the pressure reduced to 1.5 Torr. Under these conditions, rapid evaporation is expected. Initial observation of the droplet in ESEM showed that the liquor was not transparent to electrons, and hence only surface details can be studied during the evaporation process.

Figure 4.1 shows a sequence of images demonstrating the appearance of bubbles from the boiling of the liquor, and possibly some crystallites, followed by the formation of a "crust" or gel like surface with no regular structure. The nature of the crystallites formed could not be determined *in situ* but a sample of the liquor evaporated to dryness under ambient conditions was shown by XRD to be a mixture of sodium aluminate, sodium carbonate and sodium hydroxide, as expected. Some bayerite was also formed.

Evaporation of synthetic Bayer liquors or sodium aluminate/sodium hydroxide solutions would not be expected to induce the precipitation of gibbsite due to the increased solubility of aluminium as the sodium hydroxide concentration increases, hence resulting in the formation of solid sodium aluminate hydroxide species.

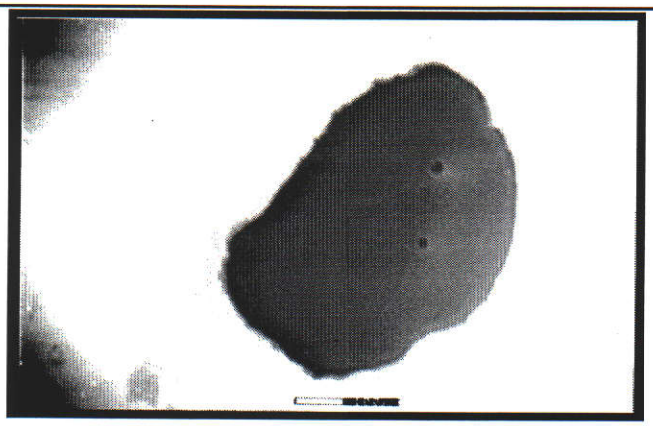

Initial Image of A Droplet of Liquor (Scale Bar = 100 μm)

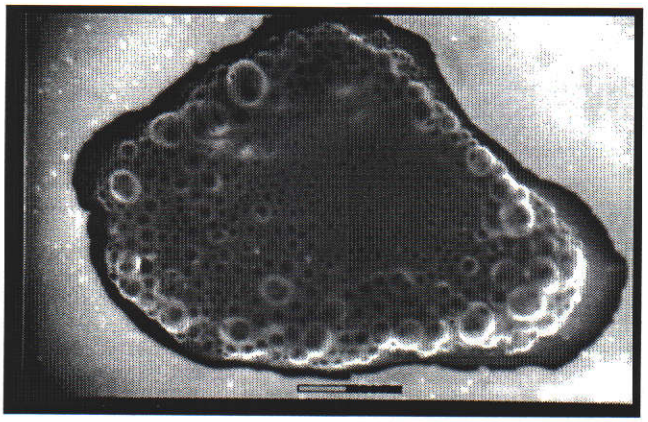

During Dehydration Process - The Appearance of Bubbles as Liquor Boils

(Scale Bar = 100 μm)

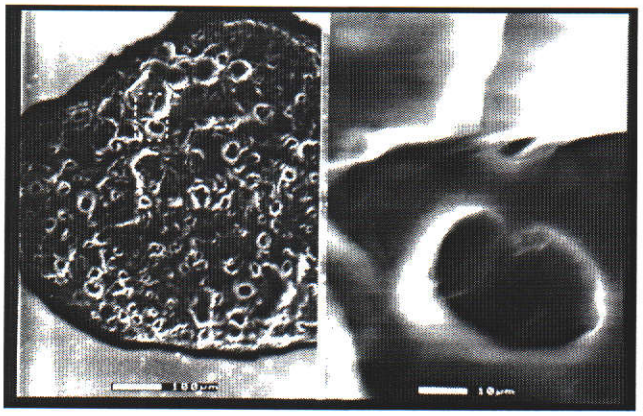

Completely Dehydrated Drop of Synthetic Liquor

Figure 4.1 Dehydration of a Drop of Synthetic Liquor at 1.5 Torr and 15°C

4.2.2 Light Microscopes

Light microscopy uses electromagnetic radiation in the ultraviolet or visible wavelength range to obtain a magnified image of an object. The resolution of the image is therefore limited to the maximum focus of the light source and this is limited by diffraction effects. Typically, the maximum resolution of a light microscope is approximately 1 μm.

The operation of all optical microscopes may be classified into either diascopic illumination, where an image is collected from the light that passes through the specimen, or episcopic illumination where the light is reflected off the specimen and then into the objective lens. The way the specimen is illuminated is important when designing a growth cell for the crystal growth studies.

A feature of a microscope which needs to be considered when developing an experimental technique is its mechanism for contrast formation. Contrast is defined as the ratio between the light and the dark features of an image. Different microscopes use different means of generating contrast such as phase contrast, dark field and differential interference contrast. Differential interference contrast microscopy, a form of interferometry, has been successfully used for the observations of CaI_2 and $BaNO_3$ growth from solutions (Tsukamoto, 1983; 1985). Tsukamoto showed that steps on a crystal surface as shallow as 1 nm can be detected visually, and their growth followed with a differential interference contrast microscope.

4.2.2.1 Light Microscopy Growth Cells

Before any optical microscopy can be used for *in situ* studies of crystal growth, growth cells need to be designed and constructed. The following requirements need to be addressed when designing a growth cell. Most importantly, for studies using Bayer liquors, all the cell parts must be inert to highly alkaline conditions at high temperatures. For this reason, stainless steel and Teflon (PTFE) were chosen as the materials for the body of the cell. Another consideration is the material of the gasket and other materials in contact with the solution used. The effects of impurities on crystallization have been widely studied (Davey and Mullin, 1976). In the case of gibbsite crystal growth, the presence of trace amounts of certain organic compounds have been shown to totally inhibit the crystallization process (Grocott and Rosenberg, 1988; Power, 1991). For this reason, the choice of the material for the gaskets and O-rings as well as tubing used is very important, especially if they are in contact with the supersaturated solutions. Although the main constituents of the material chosen may not affect crystallization, it is still important to determine if the presence of plasticizer or added dyes effect crystallization.

Other considerations depend upon the mode of operation and the type of microscope used. A growth cell may be operated in a "flow through" configuration; where the supersaturated solution is circulated through the cell, either by pumping it into or out of the cell from a thermostatically controlled reservoir. Alternatively, it can be operated in a static mode where all the constituents of the crystal growth experiment are placed in the sample chamber and the temperature of the chamber is maintained by heating the cell. Important considerations also include the method of illumination and the working distance of the lenses.

4.2.2.1.1 Experimental - The Effect of Gasket Materials on Gibbsite Crystallization

To examine the suitability of various materials as potential gaskets for the *in situ* growth cell, a 1 cm^2 sample was placed in a Nalgene bottle with 200 mL of synthetic Bayer liquor (0.700 A/C, 200 C). The solutions were tumbled in a water bath at 80°C for 24 hours. The precipitate was collected by filtration, washed with hot deionised water and air dried at room temperature. The yield was compared to that of a control where no gasket material was present (Table 4.1).

These results indicate that polypropylene, ethylene propylene (EPDM) or ultrahigh molecular weight polypropylene (UHMP) are suitable materials for the gaskets of the *in situ* growth cell. The gibbsite samples precipitated in the presence of these three materials were also characterized using an SEM and found to be comparable to that formed in the control in terms of morphology and particle size. Both the polypropylene and UHMP do not compress easily and hence do not form a complete seal with the fragile glass coverslips (see Figures 4.2 - 4.4). For this reason, polypropylene is unsuitable as a gasket material and EPDM was chosen.

Table 4.1 The Effect of Various Materials on the Yield of Gibbsite.

Material Tested	Yield (%)
Control - no additive	100
Viton	32
Silicone	
Orange	52
Clear	82
Polypropylene	100
Rubbers	
Black	87
Red	69
Orange	75
Green	32
White	0
EPDM	100
Teflon	
Virgin	134
Etched back	95
UHMP	100

Note: The difference in colour is due to the dye added

4.2.2.1.2 Growth Cell Designs

Three *in situ* growth cells were designed and constructed. The first cell is a *flow through cell* (displayed in Figure 4.2), where the supersaturated liquor is pumped into the cell using a peristaltic pump and the seed crystals are mounted on a stainless steel sample stub. The main advantage of a flow through cell is the ability to maintain a constant supersaturation in the cell. The disadvantages of this type of cell include potential scaling of the tubing, the difficulties faced when circulating hot corrosive liquids, and the problem of crystal displacement by the liquid flow.

Two static cells were also designed and constructed. The design of the cell was based on the cell used by Garside and Larson (1978). The first cell may only be used with reflected light (Figure 4.3), while the second cell may be used for transmitted or reflected light (Figure 4.4). The main advantage of the static cell is its ease of use compared to the flow through cell and its main disadvantage is the inability to maintain a constant liquor composition during the observation of crystal growth. Comparing the two static cells, while one offers greater flexibility in working distance, the other offers the capability of working with transmitted light.

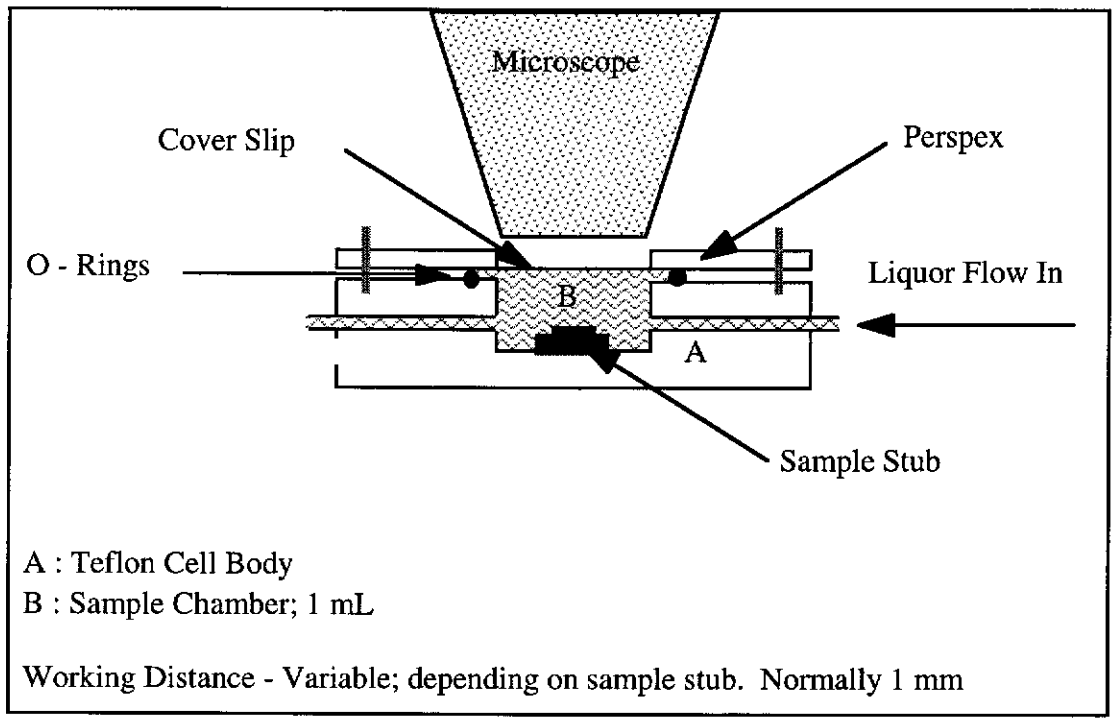

Figure 4.2 Flow Through Cell

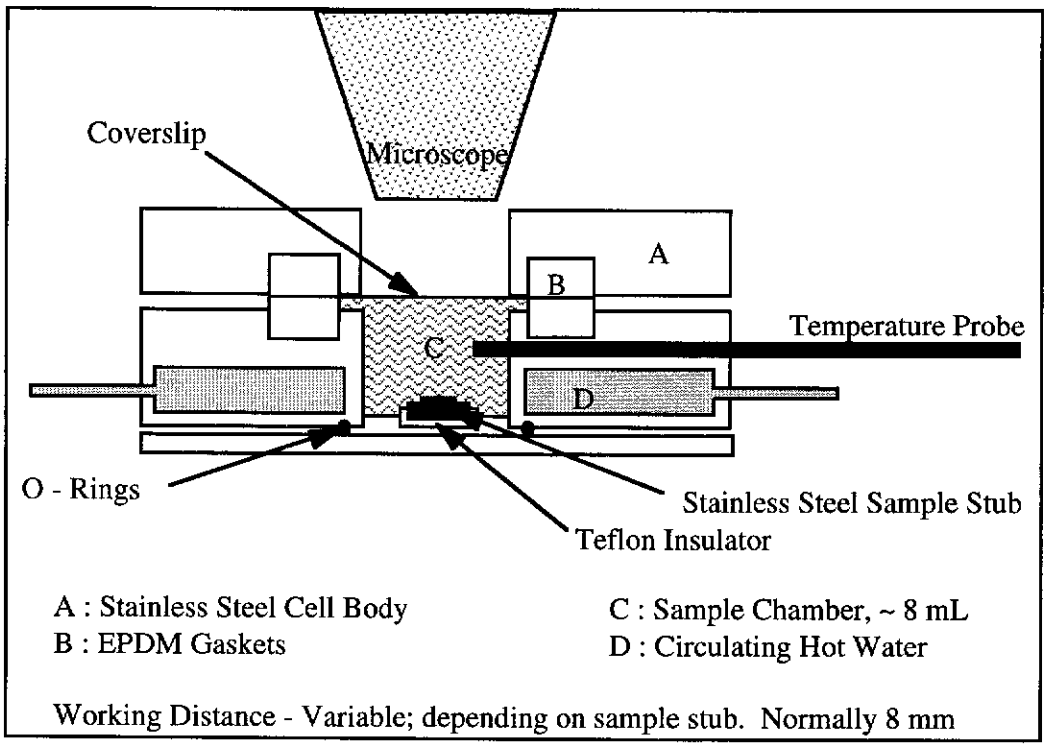

Figure 4.3 Static Cell - Reflection Mode Only

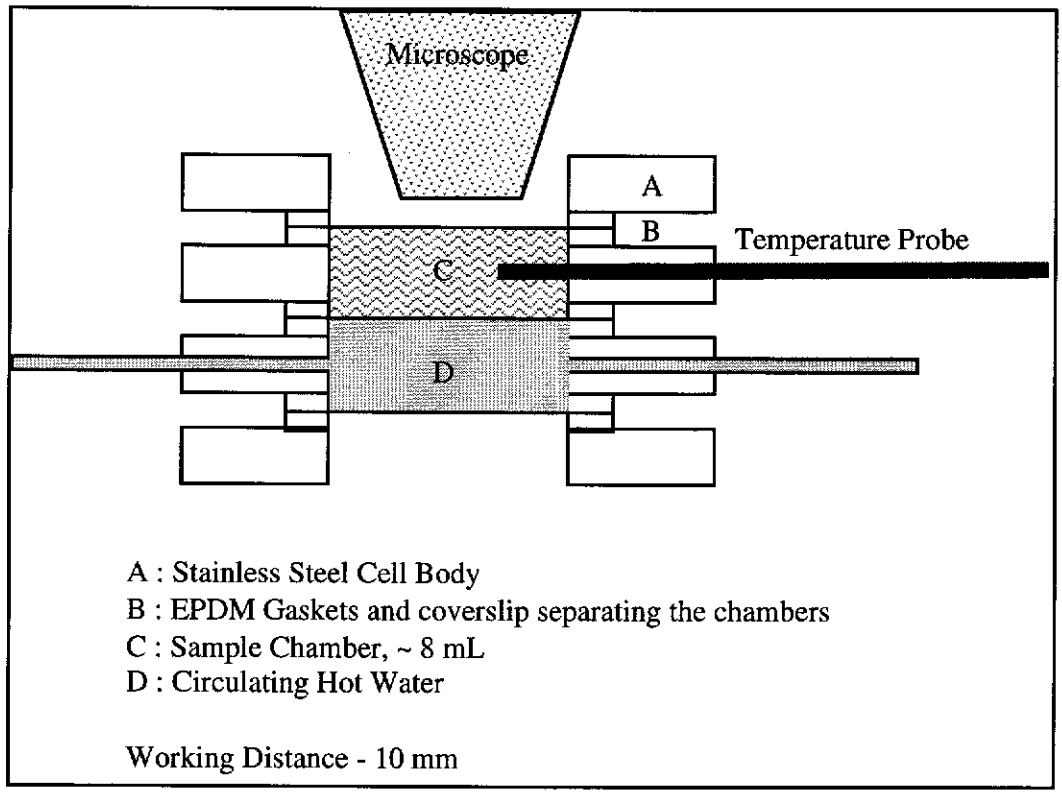

Figure 4.4 Static Cell - Transmission and Reflection Modes

4.2.2.2 Confocal Laser Scanning Microscope

Like all scanning microscopes, the sample is scanned with a beam of radiation that illuminates one point in, or on the specimen at a time. A resultant signal from the interaction of the radiation with the sample is collected, and reconstructed as an image signal. In the case of conventional light microscopy, light interacts with the sample over a vertical range, and is reflected and/or fluorescent light is emitted. This implies that the image is formed from signals from a range of depths, even those that are not in focus.

The advantage of the confocal scanning microscope is that it eliminates the scattered, reflected or fluorescent light from out-of-focus planes. The presence of two apertures in the confocal microscope strongly discriminates against the unwanted

signals, hence only the light from the focused plane is detected. As a result, the image is one of a very thin layer on which the beam is focused, with a greater resolution compared to that produced by standard optical microscopes.

With image analysis software, it is possible to "build-up" images from each focal plane, hence a height profile or 3-dimensional image may be obtained.

4.2.2.2.1 Experimental - Assessment of Confocal Laser Scanning Microscope

To assess the confocal microscope as a tool for the study of gibbsite crystal growth, the flow through cell was chosen. The static cells were unsuitable primarily due to the microscope being a inverted episcopic microscope and because of the larger size of these cell.

The solution used for this examination was a 0.700 A/C, 200 C liquor which was maintained at 70°C to allow for a drop to 10°C from the reservoir to the cell, which was at 60°C. The flow rate of the liquor to the cell was maintained at 0.5 mL/minute. The seed (C31, Alcoa Chemical Division, Arkansas) was mounted on the sample using various commercial adhesives, such as Araldite, Superglue and Chesterton Clear Protective Coating. At this level of liquor supersaturation, growth is expected, however dissolution was also observed.

Typical results from these experiments are shown in Figure 4.5 and Figure 4.6. In the first hour of crystallization, crystal growth was observed as an increase in the height of the crystal surface as shown in Figure 4.5. Some lateral dissolution was also observed. However, due to the instability of the adhesive and consequent movement of the crystals towards the coverslip, no clear conclusions may be drawn. These observed effects can be seen especially in Figure 4.6b and c; taken 10 minutes apart.

The observed dissoluton at this level of supersaturation could be due to artefacts in the experimental set up or instability of the adhesive resulting in the movement of the crystal in the duration of the experiment. Another possible reason for the dissolution of the crystals at this level of supersaturation may be due to Ostwald ripening, where the larger particles grow at the expense of smaller particles dissolving. This may be applied to the lateral dissolution of the crystal and the subsequent growth in "z" direction.

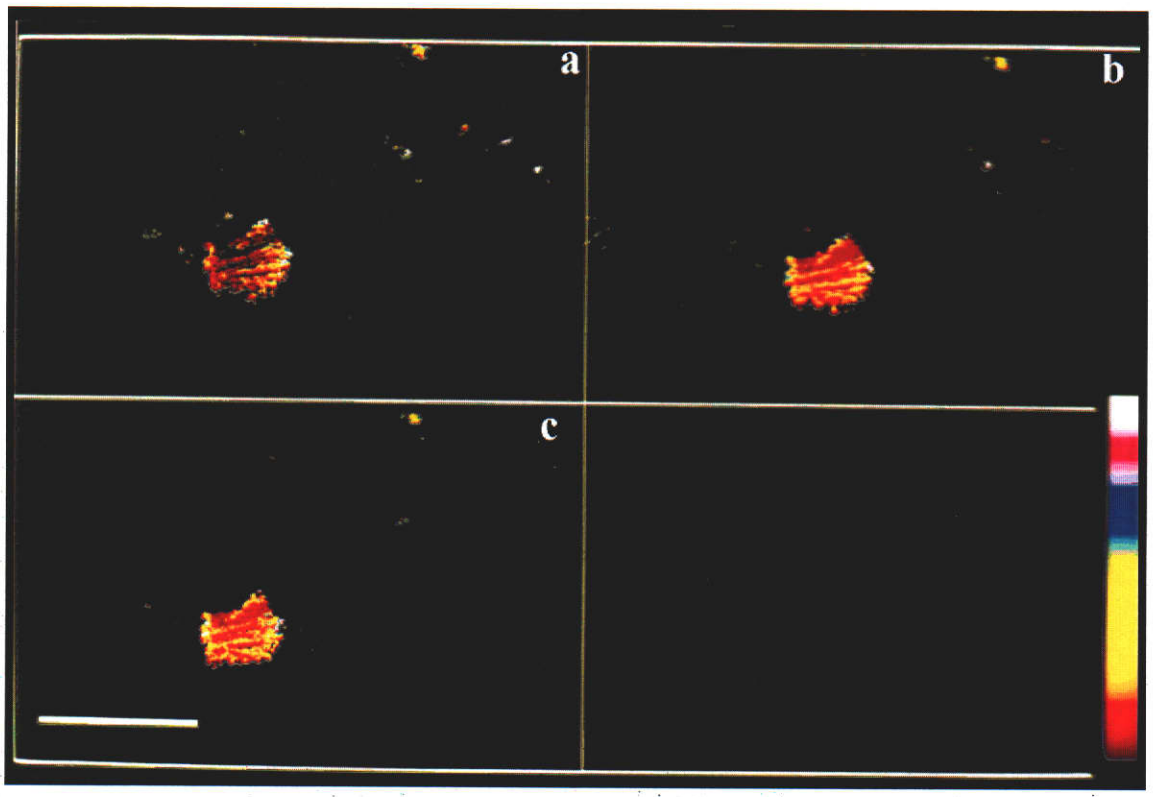

Figure 4.5 Surface Height Coding of Gibbsite Crystals During Growth Process at 60°C, a: initial, b: 20 minutes, c:50 minutes. Scale bar = 1000 μm

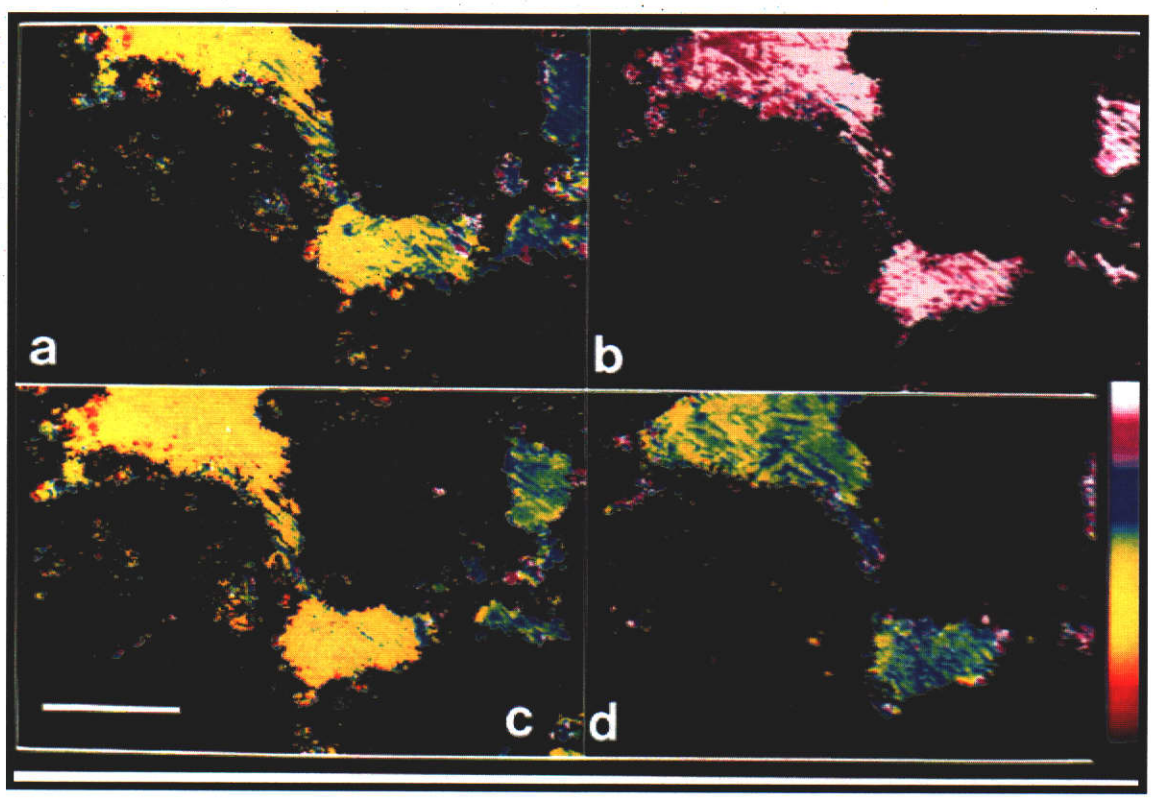

Figure 4.6 Surface Height Coding of Gibbsite Crystals During Growth Process at 60°C, a: initial, b: 72 minutes, c: 82 minutes, d: 198 minutes. Scale bar = 50 μm.

The laser confocal microscope can therefore be used to observed the overall lateral growth of a plate-like seed, as well as, growth in the [001] (approximately parallel to "z" in the images) direction. The use of adhesive, however, is unsuitable for *in situ* studies of crystal growth in Bayer liquors. The problems faced when using adhesives include swelling of the adhesive and hence movement of the crystals, as well as a potential contamination and hence growth modification.

Problems were also encountered with autoprecipitation and scaling. Due to the circulating motion of the liquor, autoprecipitation occurred quite rapidly in the tubing, and resulted in crystals being carried through to the sample chamber, and obscuring the view of the crystal of interest.

4.2.2.2.2 Experimental - Assessment of a Standard Light Microscope

The standard light microscope was assessed as a tool for the study of crystal growth of individual crystal faces, using both the static cell and the flow through cell, in a similar manner to that employed with the confocal microscope. Again, overall growth of the crystal may be observed, but only lateral growth rates may be quantified. It is possible to observe and measure the growth of all the individual crystal faces that are of interest by choosing the appropriate orientation of crystals with respect to the microscope optical axes.

The main advantages of the static cell are that it does not require an adhesive to hold the crystal in place and that growth on crystal surfaces may be observed. Figure 4.7 shows a sequence of images of a growing nucleus in a liquor (0.650 A/C, 200C) at 80°C. Growth of the (100) and (110) faces was observed, and information about the mechanism of growth on the basal face was obtained. The growth rate of the (001) face may be determined if the crystal is placed on its side (Figure 4. 8).

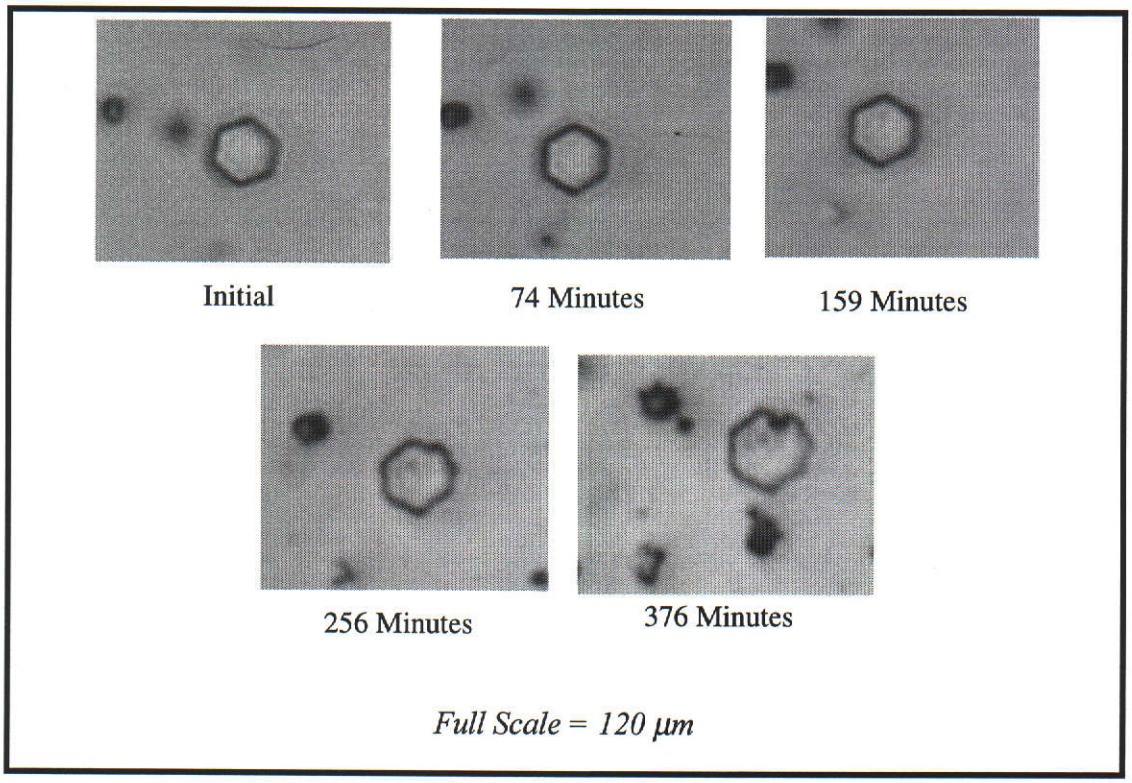

Figure 4.7 Optical Microscope Images of a Growing Nucleus Viewed along [001]

(Liquor Concentration: 0.650 A/C, 200 C; Temperature: 80°C)

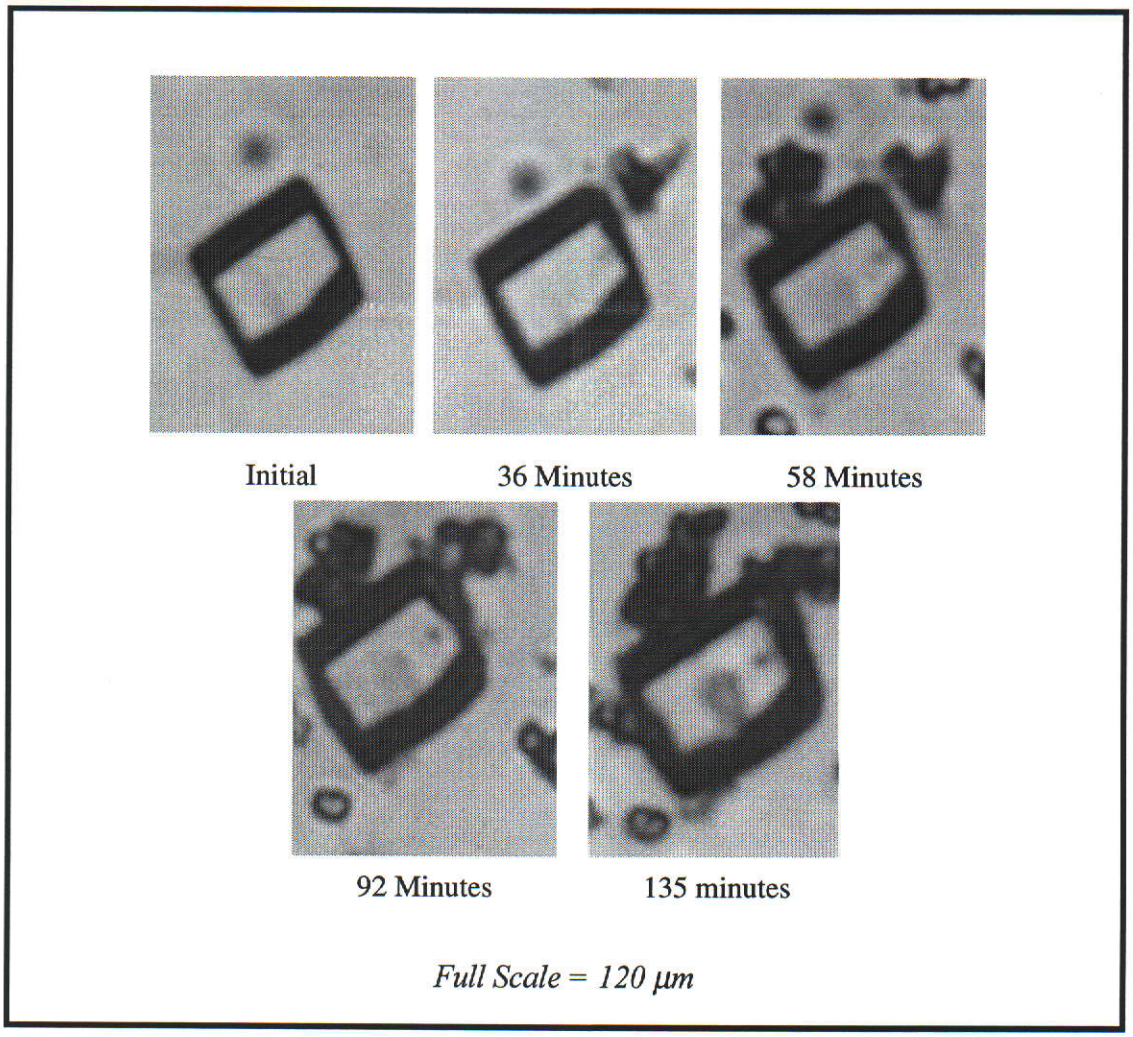

Figure 4. 8 Growth of the (001) Face of A Gibbsite Crystal Viewed Perpendicular to [001] (Liquor Concentration: 0.650 A/C, 200 C; Temperature: 80°C)

4.2.2.3 Differential Interference Microscopy and Interferometry

Similar experiments to those performed to assess the standard light microscope as a technique for the study of gibbsite crystal growth were carried out to assess a differential interference contrast microscope (DIC), using the static cell (reflection mode only) in Figure 4.3. It was envisaged that the use of DIC would enhance the observations of the surface features, allowing the presence of growth steps or

emergent dislocations to be identified. However, since gibbsite crystals are transparent, the interference from within the crystal as well as reflection of the stainless steel stub in the cell prevented the observation of growth steps of spirals.

Other interferometric techniques are not available in Western Australia, and an assessment of such techniques was not performed.

4.3. Summary

The use of various methods for the study of crystal growth have been assessed and it can be concluded that microscopy is a powerful tool for *in situ* and *ex situ* observations of crystal growth of individual crystal faces. SEM and ESEM are used in the *ex situ* studies of crystal growth. Compared to the light microscopes, the electron microscope offers better resolution (0.01 μm compared to 1 μm), hence more information may be obtained on the mechanism of gibbsite crystal growth, at the expense of the crystals having to be removed from solution, coated, and observed in a low pressure environment

Light microscope and confocal laser scanning microscopes can be used in both *in situ* and *ex situ* studies. A comparison between key features of these techniques is given in Table 4.2.

Table 4.2 Comparison Between Light and Laser Confocal Microscopes

Light Microscope	Laser Confocal Microscope
Maximum of 1 μm resolution	Maximum of 0.1 μm resolution
Narrow depth of focus	Very narrow depth of focus. Only image in the focal plane observed
Very easy technique	Ability of build up images and hence obtain height profile, or "3D" image

Although the confocal microscope may in principle be a suitable tool, crystals have to be mounted with adhesive as it has an inverted reflection configuration. In the gibbsite crystal growth studies, no suitable adhesive was found that could withstand the corrosive alkaline liquor at high temperatures. The problems faced when using adhesives include swelling of the adhesives and hence movement of the crystals, as well as potential contamination and hence interference with the growth mechanism. Due to these problems, only the static cells, used with conventional light microscopes were used for the present studies.

The growth rates obtained from the microscopic work on individual crystals are compared those obtained using dynamic light scattering (DLS). Using DLS, particle numbers and particle size can be obtained simultaneously, hence growth can be differentiated from nucleation and agglomeration. An overall growth rate may be obtained by this method.

Chapter 5

The Growth Rate of Gibbsite

5.1. Introduction

The growth rate of gibbsite has been reported to be between 1 - 2 μm/hour, and several models exist to describe the growth rate as a function of supersaturation (King, 1973; White and Bateman, 1988; Veesler and Boistelle, 1994). According to these models the growth of gibbsite follows the BCF model or spiral growth. However, observations of surface activities during the growth process indicate that the growth on the gibbsite basal face occurs by the birth and spread mechanism (Brown, 1972b). This section of the work reports the findings from *in situ* optical microscopy experiments performed to determine the growth rates of individual crystal faces of gibbsite and compares them to bulk growth rates obtained by another *in situ* technique - rapid dynamic light scattering.

The generalised growth rate term, $GR = k_0\sigma^n \exp\left(\frac{-DG}{RT}\right)$, where k_0 is the kinetic coefficient, σ is the relative supersaturation given by $\frac{A/C - A^*/C}{A^*/C}$ and ΔG is the activation energy, is used, initially to determine the dependence of growth on supersaturation and then to determine the activation energies of the individual crystal faces. The growth rate function is also compared to available models, particularly those derived by Veesler and Boistelle (1994) and White and Bateman (1988).

For the birth and spread models, the free energy of critical nucleus formation on the crystal surface will be calculated used the models derived by Gilmer and Bennema (1972), Madsen and Boistelle (1979) and Hillig (1966). These equations are given as Equations 30, 31 and 32.

Gilmer and Bennema (1972)

$$GR = k_0 (\sigma + 1)^{1/6} \sigma^{2/3} exp\left(-\frac{\Delta G}{RT}\right) \quad (30)$$

Madsen and Boistelle (1979)

$$GR = k_0 (\sigma + 1)^{1/2} \sigma^{2/3} exp\left(-\frac{\Delta G}{RT}\right) \cdot exp\left(\frac{\sigma + 1}{3}\right) \quad (31)$$

Hillig (1966)

$$GR = k_0 (\sigma + 1)^{1/6} \sigma^{2/3} exp\left(-\frac{\Delta G}{RT}\right) \cdot exp\left(\frac{\sigma + 1}{3}\right) \quad (32)$$

The effects of adding 10 mmol of various organic compounds have been studied and reported in Chapter 3. The effect of adding 1 mmol of a selected organic compound on the growth rate of individual crystal faces has also been studied and the results are reported in this chapter. The organic compounds investigated were arabinitol and xylitol, which have been shown to inhibit selectively the growth of the basal face and prismatic faces respectively.

Also studied in this section is the effect ageing a liquor has on the precipitation rate. This was then investigated further to determine whether the use of an aged liquor promotes nucleation or increases growth rates.

5.2. Optical Microscopy

Most gibbsite crystal growth studies have been carried out in large crystallizers, where overall growth rates are reported (White and Bateman, 1988; Veesler and

Boistelle, 1994). The growth rates of individual gibbsite crystal faces have only been reported in a single study (King, 1973). This work was based on an *ex situ* microscopical technique and differentiation between the prismatic faces was not reported. Further work on the characterization of the gibbsite crystal surfaces during the growth process have also been carried using *ex-situ* techniques, principally electron microscopy (Brown, 1972b, Cornell *et al.*, 1996). *In situ* optical microscopy techniques provide the advantage of being able to obtain growth rates for individual crystal faces, as well as, directly observing the growing crystal face. Artefacts due to sample handling during the growth process, such as washing and drying are eliminated in this technique.

The various types of optical microscopes and *in situ* cells have been described in Chapter 4. The work described in this section was carried out using a static cell, which may be used in transmitted or reflected light modes (Figure 4.4).

5.2.1 Preliminary Experimental Results

Preliminary experiments were carried out by allowing a liquor (0.700 A/C, 200 C) to auto nucleate in the sample chamber of the static cell at 80°C. These results showed that the addition of seed is required for the observation of the growth of individual crystal faces. This is because the time taken for the production of suitable seed crystals by auto nucleation varied from 2 - 18 hours. Furthermore, the liquor concentrations will not be accurately known after seed crystals have formed.

A method of obtaining suitable seed crystals needed to be established. Relatively large single crystals of gibbsite are required for this study. Seed crystals can be obtained commercially (C31, Alcoa Chemical Division, Arkansas), which contain some single crystals and but are primarily large agglomerates, or can be produced in

the laboratory. Any seed that has been washed and dried will be unsuitable since these precedures cause the deactivation of the seed surface (Smith and Woods, 1993). A suitable method of seed preparation is described in the experimental section (Section 5.2.2). This method, however, leads to the production of very fragile crystals which cannot be isolated. Since the seed cannot be store in the aluminate liquor (this results in the formation of agglomerates which renders it unsuitable for the study of individual crystal faces), the seed has to be prepared freshly immediately prior to use.

Although the seed charge does not affect the growth rate of an individual crystal, the overall de-supersaturation rate of the solution is dependent on the amount of seed added and growth rate is a function of the liquor supersaturation. The seed charge added to the system therefore needs to be maintained at a constant level to ensure that the desupersaturation rate is reproduced from one experiment to another. Preliminary experiments showed that the addition of too much seed resulted in crystals settling on top of each other, whereas adding insufficient seed resulted in a rapid rate of autonucleation which severely decreased the available recording time for an experiment. With a low seed charge, difficulties were faced when attempting to locate a crystal. In either case the view of the crystals of interest is, or ultimately will be obscured by the presence of other crystals, due to either autonucleation or settling. It is this obscuring of crystals that determines the maximum length of a growth experiment. The addition of seed to the liquor was also conducted at the temperature of the experiment to prevent nucleation of crystals.

Attempts were also made to maintain the relative supersaturation by using the minimum amount of seed in the cell and minimising the recording time. However, due to the slow growth rates of gibbsite and also the resolution of the microscope ($\pm$ 0.5 μm), the time during which growth can be recorded needs to be maximised. It

is therefore necessary to optimize the system by balancing these opposing requirements.

The growth rate of a crystal face is obtained from the gradient of a plot of a length normal to the crystal face versus time. Errors in the growth rate were obtained by a least squares calculation on this plot.

5.2.2 Experimental

5.2.2.1 Seed Preparation

Synthetic liquor (0.650 A/C, 200 C) was prepared by dissolving aluminium wire in sodium hydroxide; it was filtered twice through a 0.2 μm membrane and allowed to stand for 16 hours in a water bath at 80°C. The suspended solids content in this solution, after ageing, was determined gravimetrically by filtration of a known amount through a 0.2 μm membrane, washing with hot deionised water and drying at 80°C for 30 minutes.

5.2.2.2 Liquor Preparation

All the liquors were prepared using sodium hydroxide and aluminium wire, filtered through a 0.2 μm membrane and heated to 80°C prior to use. The liquors were analysed by a modified Watts Utley titration method (Watts and Utley, 1953; 1956) to determine the alumina and caustic concentrations prior to and at the end of the experiments.

5.2.2.3 Experimental Set Up and Growth Rate Analysis

A known mass of seed suspension, maintained at 80°C, was added to a known mass of filtered liquor, also maintained at 80°C to obtain a final solid concentration of 50 ppm by weight. This was then transferred to the preheated cell (80°C) which was placed on the microscope for the observation of crystal growth.

The growth of gibbsite nuclei was recorded on a Nikon Labophot-2 optical microscope fitted with a camera. Images of the crystals were captured at set time intervals on 35 mm photographic film. These images were used to determine the growth rates. For the individual prismatic faces, the growth rates for a crystal face were calculated as the difference in the length normal to the crystal face per unit time. The crystals used for these calculations were such that they were viewed perpendicular to the basal face (see for example Figure 4.7). The final growth rates are reported as μm/hour.

To obtain the growth rate of the basal face, the crystals were viewed along the basal face (or perpendicular to a prismatic face) (see for example Figure 4.8), and the growth rates were calculated in a similar manner to that used for the individual prismatic faces. Although the exact prismatic face (i.e. {100} or {110}) may not be identified, the generic growth rate for prismatic faces may also be determined. To determine the length of this prismatic face, an extrapolation has to be made, as shown in Figure 5.1.

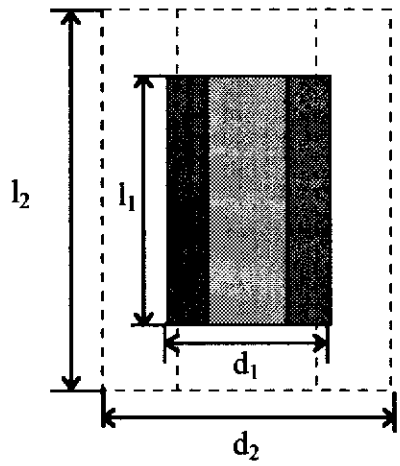

l_1 & l_2 are length of basal face at time (t) and

d_1 & d_2 are diameter of the crystal at time (t)

$$\text{Growth Rate of Basal Face} = \frac{l_2 - l_1}{t_2 - t_1}$$

To obtain the growth rate of the prismatic, the length of the prismatic(l_p) has to be extrapolated from the diameter of the crystal.

$$\cos\theta = \Delta l_p / \Delta d$$

$$\theta = 60^o$$

$$\text{Therefore } \Delta l_p = \Delta d \cdot \cos\theta$$

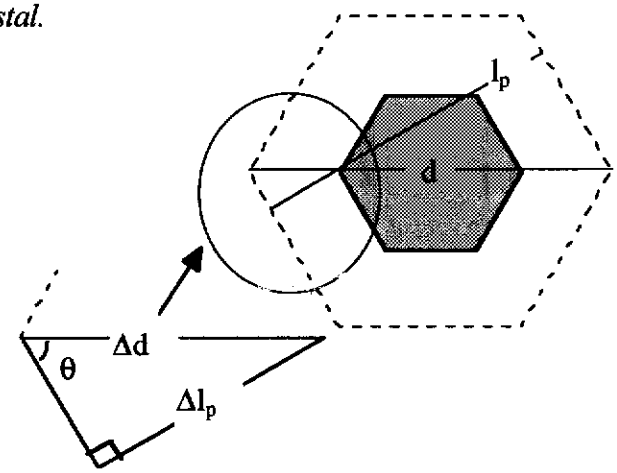

$$\text{Growth Rate of Prismatic Face} = \frac{\Delta d \cdot \cos\theta}{t_2 - t_1}$$

Figure 5.1 Measurements to Obtain the Growth Rates of the Basal Face and the Prismatic Face for Crystals Viewed Perpendicular and Parallel to [001] Respectively

5.2.2.4 The Effect of Supersaturation at Constant Temperature - Growth Mechanism

To determine the effect of supersaturation, the growth of the crystals were recorded under standard conditions (eg. 0.650 A/C, 200 C at 80°C) for two hours before changing the liquor to one with a different supersaturation value. The growth rates obtained are therefore relative to the standard conditions. This method was adopted because of the growth rate dispersion that was observed in Section 5.2.3.2. The experimental regime for determining the effects on supersaturation is given in Table 5.1. Initial experiments were conducted to ensure that the growth rates remained constant when changing from one standard to another (0.650 A/C→ 0.650 A/C) and to determine if the relative growth rate changes obtained by increasing the liquor concentration (0.550 A/C → 0.700 A/C) is the same as that obtained by decreasing the liquor (0.700 A/C → 0.550 A/C). The difference in supersaturation needs to be sufficiently large to obtain measurable differences in growth rates, and this has to be considered in the experimental design.

Table 5.1 Experimental Design: Effect of Liquor Composition on Growth Rates. (Values shown are the A/C values, at 200 C and their corresponding σ (as defined by Equation I) values at 80°C)

2nd Liquor Concentration A/C	Initial Liquor Concentration , A/C (σ)					
	0.500 (0.40)	0.550 (0.54)	0.600 (0.67)	0.650 (0.81)	0.700 (0.95)	0.750 (1.09)
0.500				√		
0.550					√	
0.600						
0.650				√		
0.700	√	√				
0.750			√	√		

5.2.2.4.1 Analysis of Results Obtained from the Effect of Relative Supersaturation on Growth Rates Experiments

According to simplified crystal growth theories, growth rate may be expressed as a function of supersaturation to the power of *n* (Equation 17, Chapter 1). A quadratic equation (or $n = 2$) is predicted if the crystal grows by a spiral growth mechanism, whereas if a linear relationship is obtained, this may be taken as an indication of the operation of a birth and spread mechanism (Mullin, 1994). Curve fitting software (Microsoft Excel, Version 5.0) will be used to compare the degree of fit to both of these mechanisms for the results obtained for growth rates as a function of relative supersaturation.

Liu *et al.*, (1997) showed that by plotting the $\ln\left(GR/\sigma^{5/6}\right)$ *versus* $1/\sigma$, the birth and spread growth rate equations, both for mononuclear and polynuclear processes, can be linearised, but not the growth rate equation for the spiral growth mechanism (Figure 5.1) The results obtained in the present work will be treated in a similar manner to determine the growth mechanism. If crystal growth is believed to follow the birth and spread mechanism, appropriate logarithmic plots of Equations 19 and 20 will be carried out in attempt to differentiate between the mononuclear and polynuclear mechanisms and the edge free energy will be calculated.

All the results plotted and discussed are the average growth rates obtained for several single crystals (at least 5).

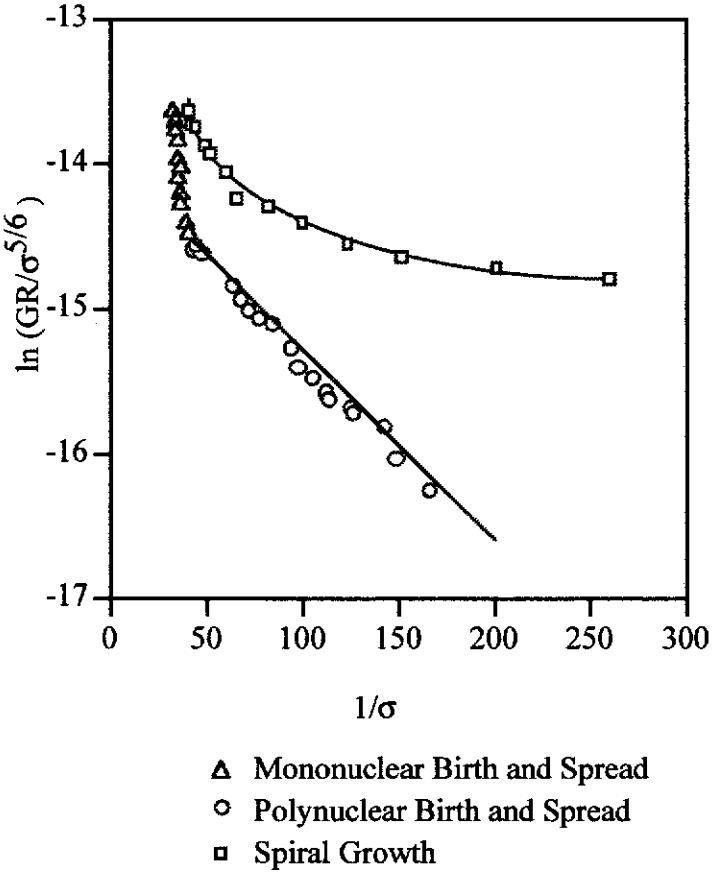

Figure 5.2 Plot of $\ln\left(GR/\sigma^{5/6}\right)$ *versus* $1/\sigma$, *showing Linearised Growth Rates as a Function of Supersaturation Equations for the Birth and Spread Model but not Spiral Growth Model (after Liu et al., 1997)*

5.2.2.5 The Effect of Temperature at Constant Supersaturation - Activation Energy Calculations

Growth experiments were carried out at 60, 70 and 80°C at a constant relative supersaturation of 0.81. These correspond to A/C values of 0.418, 0.530 and 0.650 at 200 C respectively. Like the experiments carried out to determine the effect of supersaturation on the growth rates, initial experiments was carried out at 80°C for two hours, before changing the liquor and the temperature to 70°C and 60°C

the laboratory. Any seed that has been washed and dried will be unsuitable since these precedures cause the deactivation of the seed surface (Smith and Woods, 1993). A suitable method of seed preparation is described in the experimental section (Section 5.2.2). This method, however, leads to the production of very fragile crystals which cannot be isolated. Since the seed cannot be store in the aluminate liquor (this results in the formation of agglomerates which renders it unsuitable for the study of individual crystal faces), the seed has to be prepared freshly immediately prior to use.

Although the seed charge does not affect the growth rate of an individual crystal, the overall de-supersaturation rate of the solution is dependent on the amount of seed added and growth rate is a function of the liquor supersaturation. The seed charge added to the system therefore needs to be maintained at a constant level to ensure that the desupersaturation rate is reproduced from one experiment to another. Preliminary experiments showed that the addition of too much seed resulted in crystals settling on top of each other, whereas adding insufficient seed resulted in a rapid rate of autonucleation which severely decreased the available recording time for an experiment. With a low seed charge, difficulties were faced when attempting to locate a crystal. In either case the view of the crystals of interest is, or ultimately will be obscured by the presence of other crystals, due to either autonucleation or settling. It is this obscuring of crystals that determines the maximum length of a growth experiment. The addition of seed to the liquor was also conducted at the temperature of the experiment to prevent nucleation of crystals.

Attempts were also made to maintain the relative supersaturation by using the minimum amount of seed in the cell and minimising the recording time. However, due to the slow growth rates of gibbsite and also the resolution of the microscope ($\pm$ 0.5 μm), the time during which growth can be recorded needs to be maximised. It

after 0, 30, 60, 120, 240, 360, 480 and 1440 minutes. The exit liquor was analysed for alumina and caustic concentrations.

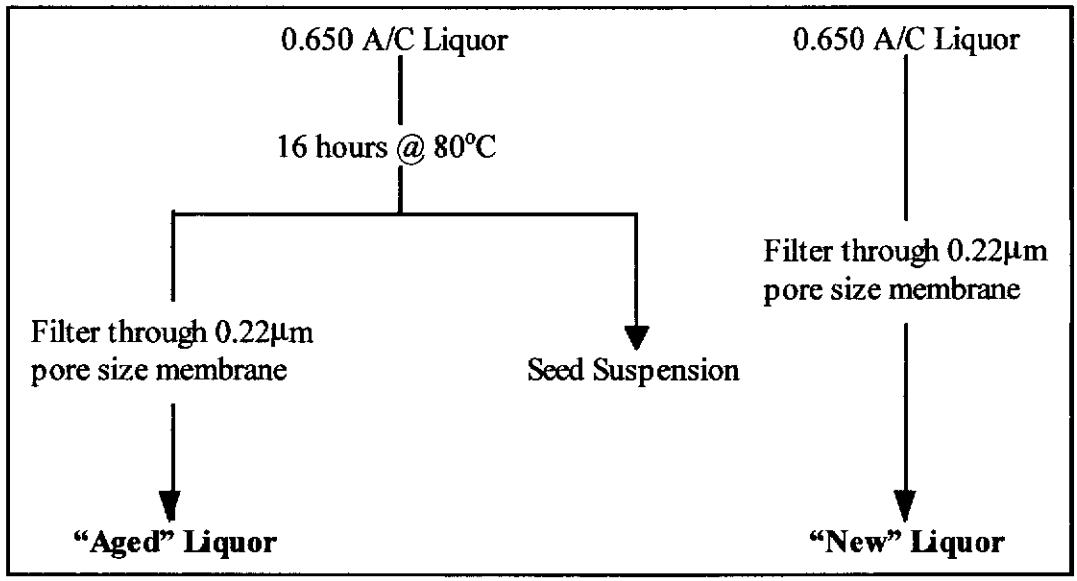

Figure 5.3 Schematic of Liquor Preparation to Examine the Effect of Liquor History

The effect of ageing a liquor on the growth rates of the individual crystal faces was also examined.

5.2.3 Results and Discussion

5.2.3.1 Growth Rate of Individual Crystal Faces

The growth of gibbsite crystals and the growth rates of individual crystal faces have been successfully measured by *in situ* optical microscopy. Typical results for the growth rates of the individual prismatic faces are given in Figure 5.4, which shows that the growth rates of the (100) and (110) faces are similar, and that the growth rates are constant with time. Liquor concentration measurements (0.650 A/C, 200 C at the beginning of the experiment and 0.649 A/C, 200 C at the end of the experiment)

showed that for the duration of the experiment, the relative supersaturation remained constant. From these experiments, it can be concluded that the growth rates are constant at a fixed supersaturation.

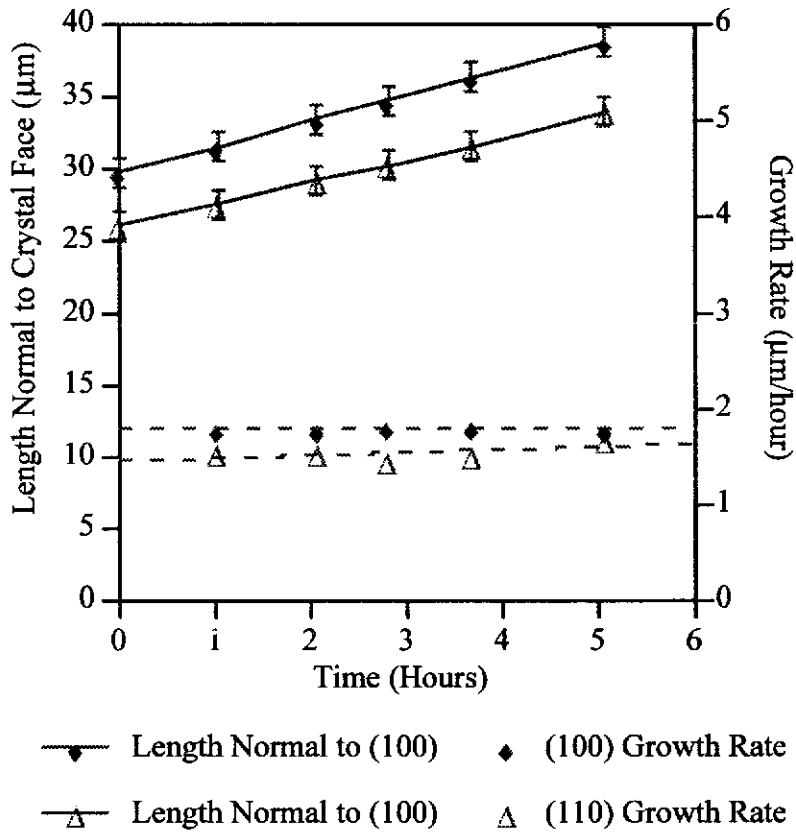

Figure 5.4 Growth Rate of Prismatic Faces

The similarities in the growth rates for the prismatic faces is linked to maintenance of habit of the crystals during the growth process. In the investigations on the growth rates of gibbsite crystals, it was found that the gibbsite single crystals may have three different shapes: diamond, hexagons and elongated hexagons (Figure 5.5). Morphologically, in the diamond crystals, the {110} faces have a larger surface area than the {100} faces, in the elongated hexagons the {100} faces have a larger surface area than the{110}; whereas in the hexagons, the two types of faces have similar surface areas per face. The difference in habit between the crystals implies that at

some stage, the {100} and {110} had different relative growth rates, a slower growth rate yielding a larger surface area. Experimentally, it was found that although there are no trends observed in the occurrence of a particular shape, a generalisation on their growth rates relative to each other can be made. Within the same experiments, the growth of diamond shaped crystals is the slowest while the growth of elongated hexagons is the fastest. Table 5.2 gives typical results obtained for growth rates of the prismatic faces from the different shape crystals. However, when attempting to quantify this trend, the differences between the growth rates of the (100) face and (110) face are too small to allow them to be distinguished such that the growth rate of (100) face is equal to that of (110) face, within experimental errors.

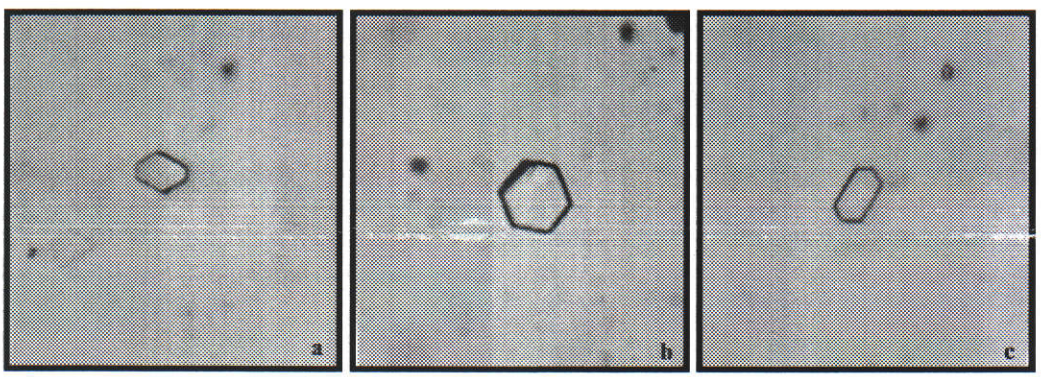

Figure 5.5 Three Crystal Habits of Gibbsite Single Crystals. (Full Scale = 120 μm)

a: "Diamond", b: "Hexagon", c: "Elongated Hexagon"

Table 5.2 Average Growth Rates of Prismatic Faces from Different Shape Gibbsite Crystals from One Experiment

Crystal Shape	Growth Rates (± 0.2 μm/hour)	
	(100) Face	(110) Face
Diamond	0.7	0.8
Hexagon	1.6	1.5
Elongated Hexagon	1.8	1.7

Experimentally, it is found that a hexagonal crystal grows to form a larger hexagon and a diamond shaped crystal grows to form a larger diamond shaped crystal, indicating that the relative growth rates of the prismatic faces does not change. The similarities in the growth rates of the prismatic faces is also expected due to the similarities in the atomic structure of the crystal faces (Figure 3. 10). Thus, the crystal habit is related to the phenomenon of growth rate dispersion (see Section 5.2.3.2), and may indicate, for example, different levels of defects or impurities in the different shaped crystals.

The growth rate of the basal face, compared to the prismatic faces, may be obtained if a crystal is placed on its side. However, for this to occur elongated hexagonal crystals are required, otherwise a crystal balanced on its side will be unstable. A comparison between the growth rates of the prismatic faces compared to that of the basal is given in Figure 5.6, showing the relative growth rate of the (001) face to be faster than the prismatic faces. Although the basal face has been reported to be the slowest growing face (Brown, 1972b), and morphological studies also indicate that it is the slowest growing face, the growth rate results shown in Figure 5.6 show the

opposite. This growth rate result is supported by the resulting crystal morphology, elongated hexagonal prisms, where the slowest growing faces are more prominent - in this case the prismatic faces.

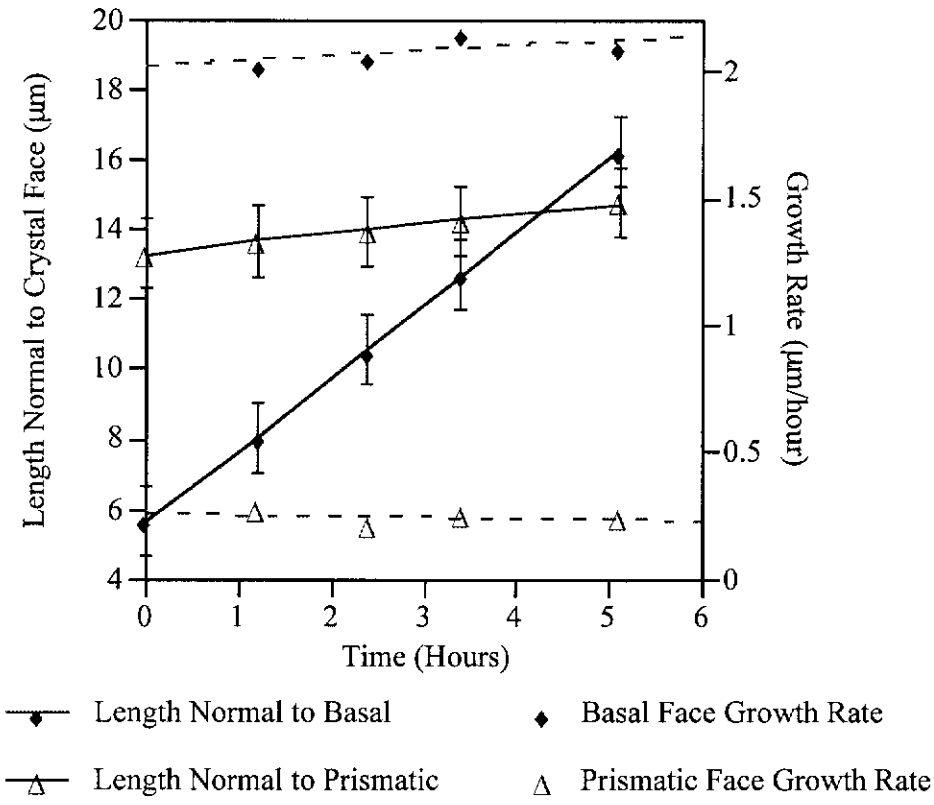

Figure 5.6 Comparison Between the Growth Rates of Basal Face and Prismatic Face

By observing the surface features of the crystal during the growth process, direct information may be obtained about the growth mechanism. Figure 5.7 shows growth on the basal face with the presence of nuclei (time = 56 minutes) on the initially smooth surface of a crystal and their subsequent growth with time (birth and spread model). Although it is not possible to observe the formation of the nuclei due to to the resolution of the microscope; the subsequent growth of these nuclei can be seen once they reach a critical size. This phenomenon is not observed on the prismatic faces (Figure 5.8), implying that the growth of the prismatic faces may not follow the birth and spread mechanism and/or the resolution of the microscope is insufficient to resolve the surface activity of the prismatic faces. Experiments carried out for up to 8 hours,

again showed the growth of the prismatic faces to be an enlargement in crystal size while the formation of nuclei on the crystal surface was not observed.

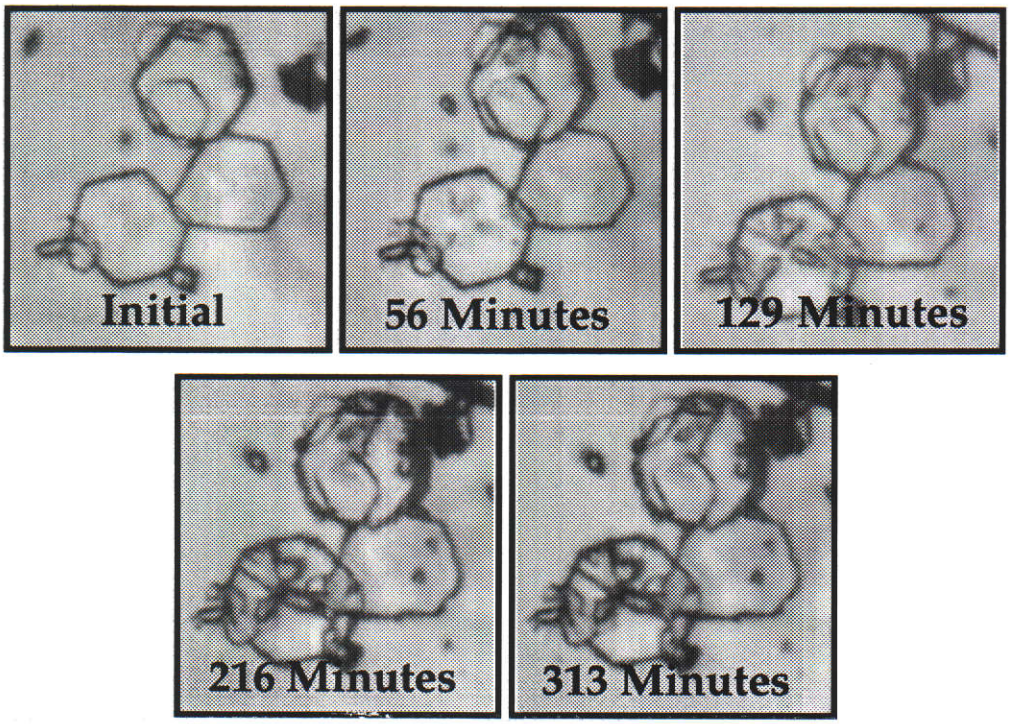

Figure 5.7 Birth and Spread of Nuclei on the Basal Face

(Full Scale = 120 μm)

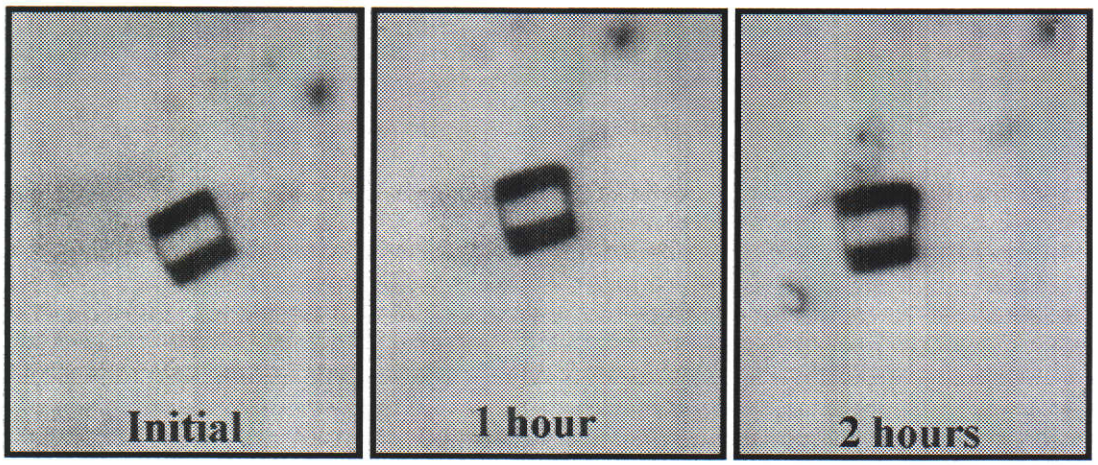

Figure 5.8 Growth on a Prismatic Face of Gibbsite Crystal

(Full Scale = 120 μm)

5.2.3.2 Growth Rate Dispersion

Under identical experimental conditions, differences in growth rates were observed for apparently identical crystals, the difference ranging from no growth to up to 10 μm/hour. The growth rates were found to vary not only from experiment to experiment, but from crystal to crystal within the same experiments as well.

The variations in the growth rate from one experiment to another is given in Figure 5.9, showing that the difference in growth rates from one experiment to another can be up to a factor of 10 for the prismatic faces.

It is unknown why some crystals grow at a faster rate. A possible explanation could be that during preparation of the the seed, variations in some factors may not have been considered such as fluctuation in the temperature during the ageing process or in preheating the seed suspension and the duration of ageing the liquor.

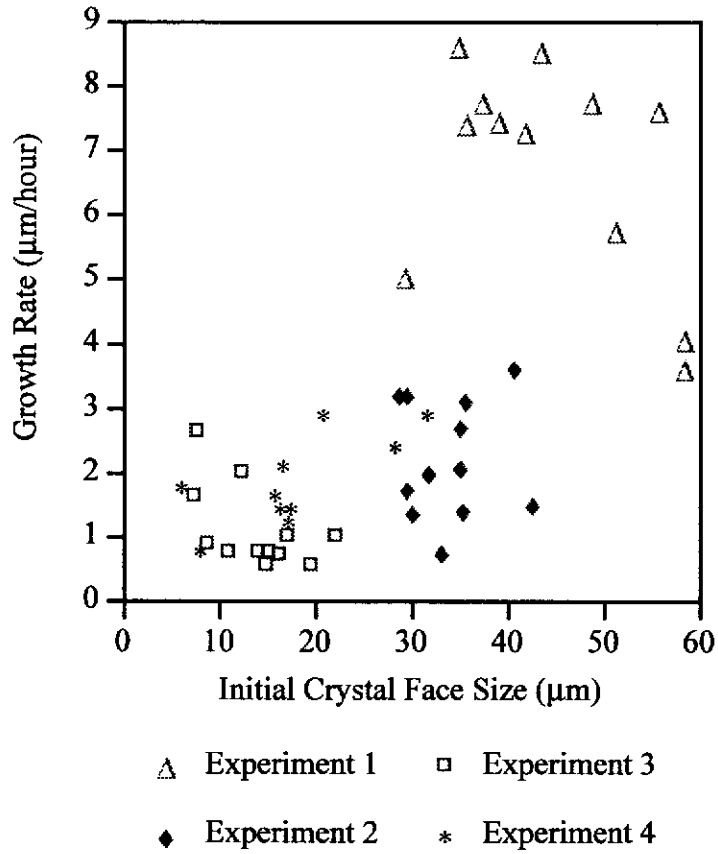

Figure 5.9 Variations in the Growth Rate of the (100) Face Between Experiments

Figure 5.10 shows the variation in the growth rates of the prismatic faces obtained for gibbsite crystals grown under apparently identical conditions. Although there appears to be a trend, where higher growth rates are obtained for larger crystals, the growth rate dependency on size is questionable since there is an insufficient number of crystals larger than 30 µm.

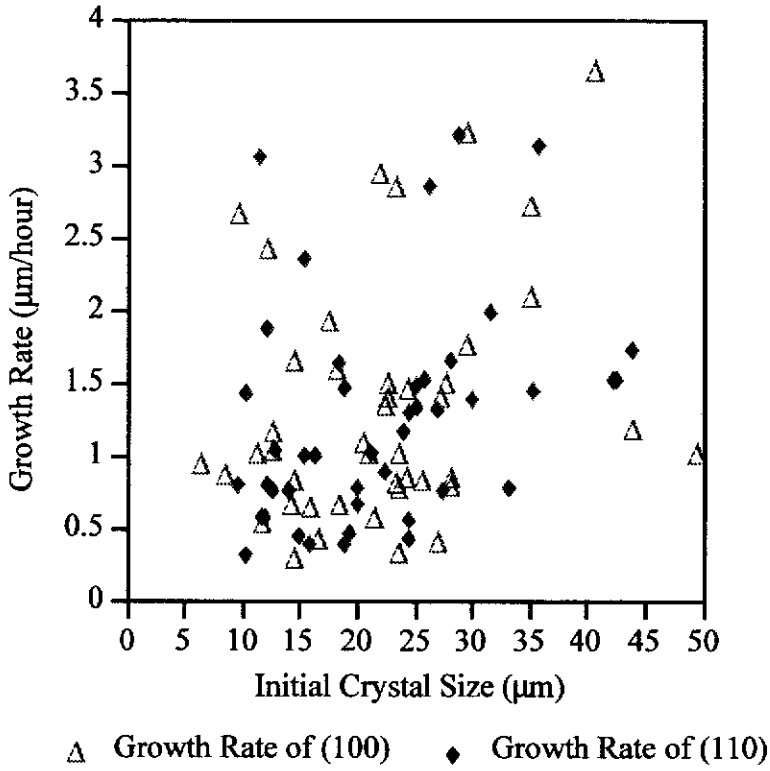

Figure 5.10 Growth Rate Dispersion of Gibbsite Crystals

Growth rate dispersion was also observed for the basal face (Figure 5.11). The constancy in the ratio of the prismatic to basal growth rates, as reported by King (1973), was not observed. The ratio of prismatic to basal growth rates was found to vary from one crystal to another, mostly in the range 1 - 1.2. The implication of relative growth rates (prismatic growth rate to basal growth rates) remaining the same is that the crystal habit does not change, as was generally observed visually (Figure 5.12a). In some cases, the ratio between the growth rates is as high as 2, when further elongation of the crystal occurs (Figure 5.12b) or as low as 0.8, when the basal face has the slowest growth rate resulting in a crystal which is more tabular.

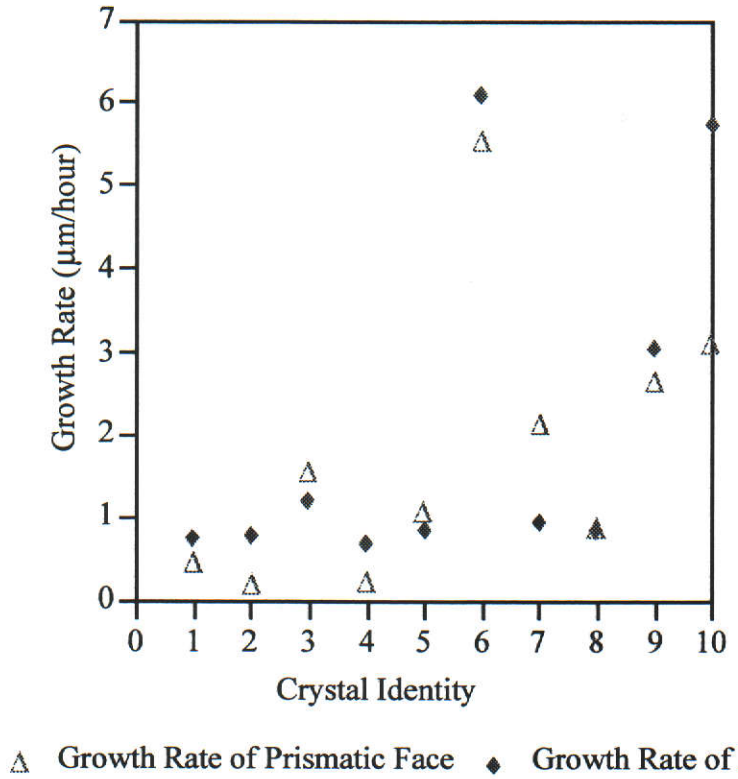

Figure 5.11 Varying Growth Rates of Basal and Prismatic Faces

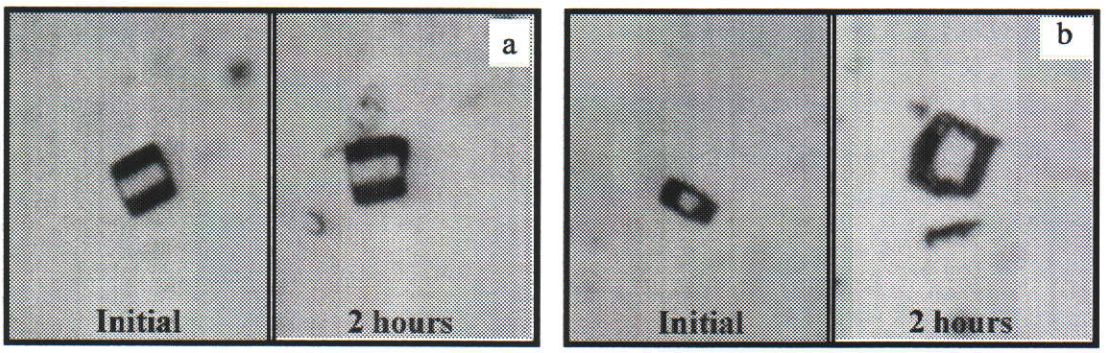

Figure 5.12 Effect of Different Relative Growth Rates on Crystal Habit a) The growth rate of the basal face is equal to the growth rates of the prismatic faces; b) The growth rate of the basal face is greater than growth the growth rate of the prismatic faces (Full Scale = 120 µm)

When averaging all the growth rates obtained for the standard condition, 0.650 A/C, 200 C, i.e. relative supersaturation of 0.81, at 80°C, a growth rate of 2 μm/hour was obtained for the prismatic faces. A growth rate of 1-2 μm/hour was reported by Misra and White (1971), which was an average of a large number of particle faces obtained from bulk experiments. The same comparison cannot be made for the basal face, due to the morphology of the crystal. (The morphology of the crystals used for the determination of the growth rate of the basal face is an elongated hexagonal prism, where the basal face grows fater that the prismatic faces. This is contrary to literature results (for example, Brown, 1972b) and to the general morphology of the gibbsite crystals where the basal face is the slowest growing face.

5.2.3.3 Effect of Supersaturation on Growth Rate

Initial results showed that whilst the phenomenon of growth rate dispersion is observed, giving different growth rates for different crystals under identical conditions, changing those conditions affects the different crystals by the same relative amounts. This implies that if a crystal face grows at 2 μm/hour at a relative supersaturation of 0.81 at 80°C, then this growth rate will be maintained if the liquor is replaced with one of identical composition, under the same conditions (Figure 5.13). Also, if the growth rate of a crystal face, growing at a rate of 2 μm/hour, increases by a factor of 2 due to an increase in supersaturation, the growth rate of a crystal growing at 1 μm/hour will also increase by a factor of 2 if subjected to the same changes (for example, see Figure 5.13). This allows the effect of supersaturation on growth rate to be studied in the presence of growth rate dispersion.

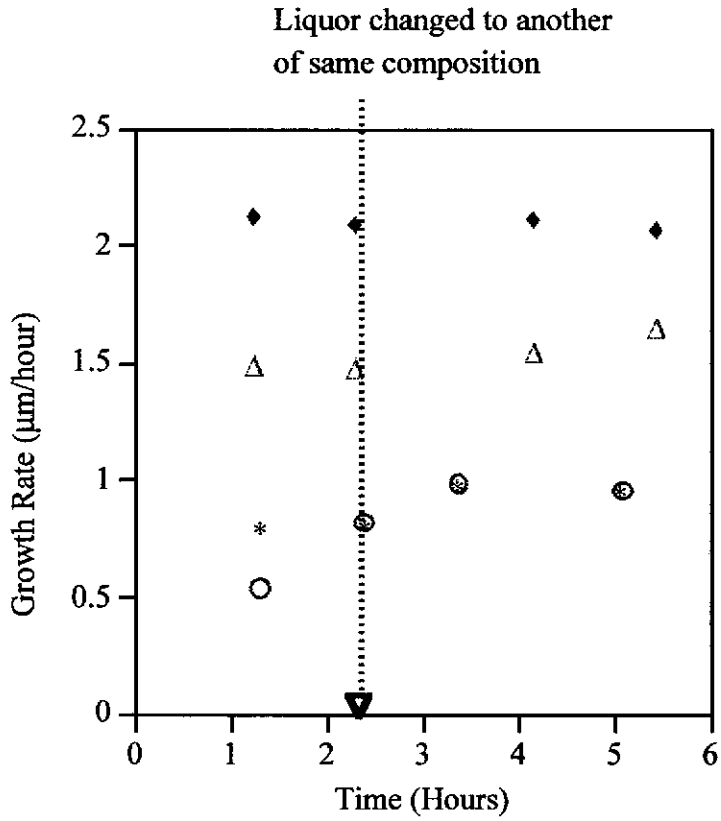

♦ Crystal 1, (100) Growth Rate * Crystal 2, (100) Growth Rate

Δ Crystal 1, (110) Growth Rate o Crystal 2, (110) Growth Rate

Figure 5.13 Growth Rates of Prismatic Faces Generally Remain Constant When the Liquor is Replaced with One of Identical Composition

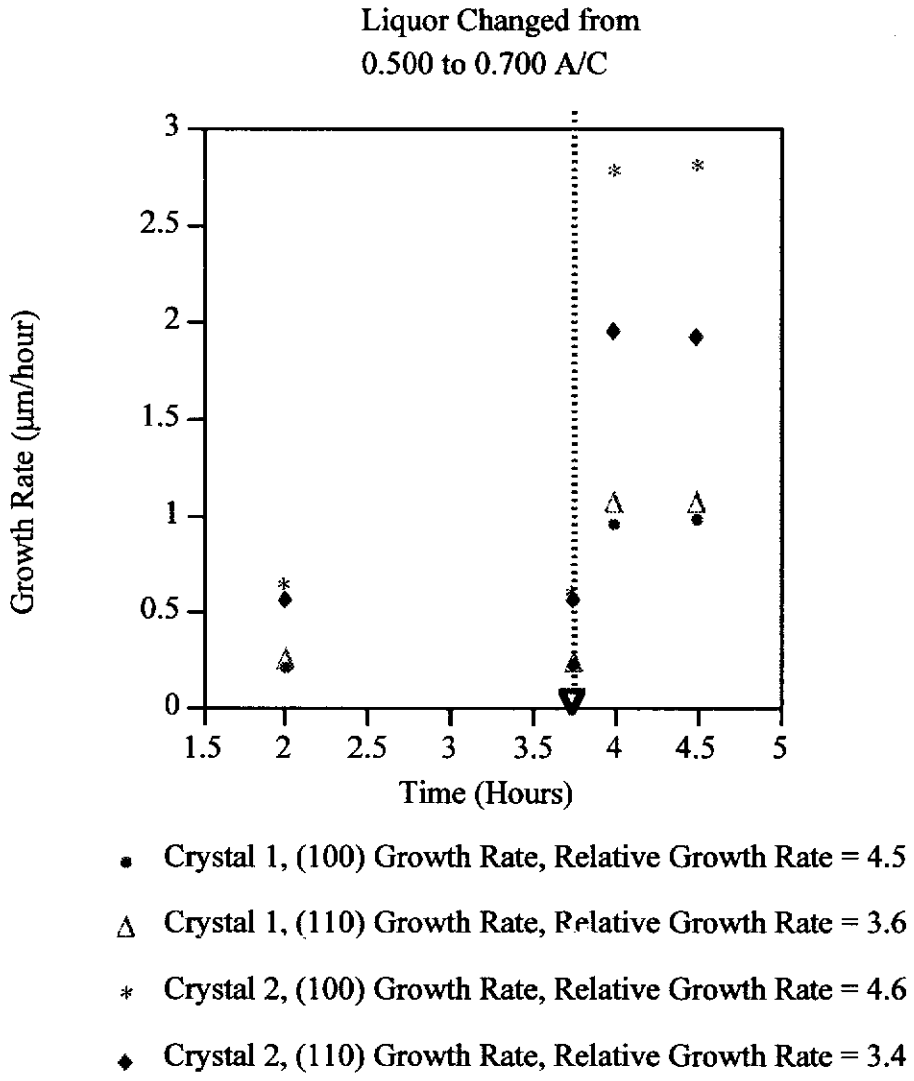

Figure 5.14 Although Growth Rates Varies from Crystal to Crystal, the Relative Growth Rate Remains Constant when Changing Liquors to One of Different Composition.

Although the growth rate changes by a fixed ratio in an experiment, this ratio depends on the initial and subsequent liquor concentrations. For example, starting a liquor of 0.500 A/C, 200 C and changing it to 0.700 A/C, 200 C gives a different relative growth rate than starting at 0.700 A/C and decreasing it to 0.500 A/C. This effect is more prominent on the basal face and can be explained by the higher relative supersaturation of the liquor providing more driving force for the formation of two dimensional nuclei and hence resulting in the crystals having a higher growth rate (due

to more active sites or surface areas) when compared to crystals starting at the lower supersaturation.

The results for the effect of relative supersaturation discussed in Sections 5.2.3.3.1 and 5.2.3.3.2 refer to growth rates obtained from experiments starting at the lower relative supersaturation, and changing it to one with a higher value.

The presence of chamfered faces has been discussed in Chapter 3. These faces can be identified on some seed crystals as shadows on the prismatic faces but the measurements of their growth rate was not possible. It is, however, worth noting that the development of these faces was more pronounced when low relative supersaturation liquors were used. This is in agreement with the morphological studies which showed these faces were only present when the crystals were grown slowly, or by using liquors with low relative supersaturation.

5.2.3.3.1 Basal Face

The effect of supersaturation on the growth rate (GR) of the basal face is shown in Figure 5.15. From curve fitting calculations, the data fit best to the exponential function $GR = 0.08\ e^{2.96\sigma}$ (correlation coefficient = 0.994). This however is not compatible with the theoretical kinetic models available, where growth rate is expressed as a function of relative supersaturation to the power of n (Equation 17). Analyses of the bulk growth rates reported by Veesler and Boistelle (1994) showed that their data may also be fitted to an exponential function, $GR = 0.52\ e^{4.89\sigma}$, however a better fit can be obtained with a quadratic function with these data.

The experimental results obtained for the growth rates may also be fitted to a linear trend, where GR = $2.565\sigma + 0.9479$ where correlation coefficient is 0.925 and GR = $1.5285\sigma^{1.988}$, with a correlation coefficient of 0.964. If the quadratic equation is considered to have a better fit than the linear equation, this implies that the basal face grows via a spiral growth mechanism, which is not consistent with visual observations.

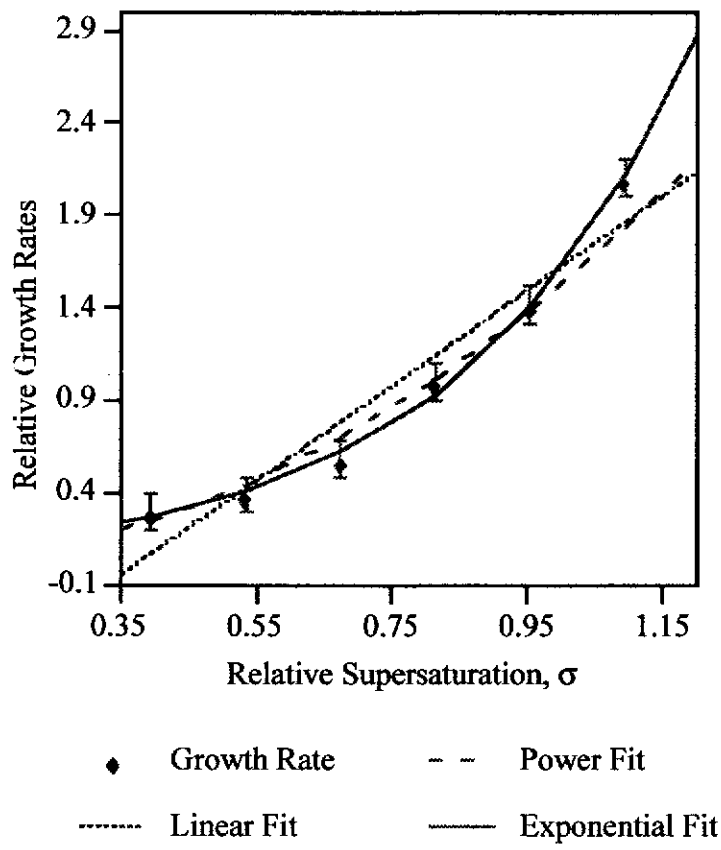

Figure 5.15 Growth Rate of Basal Face as a Function of Supersaturation: Fitting of Linear, Power and Exponential Functions

Figure 5.16 is a plot of $\ln\left(GR/\sigma^{5/6}\right)$ *versus* $1/\sigma$ showing a linear relationship above a relative supersaturation of 0.67 at 80°C. This implies that above this level of supersaturation, growth occurs by a birth and spread mechanism (see Section 5.2.2.4.1). Below a relative supersaturation of 0.67 at 80°C, from the curve of the plot, the spiral growth model describes the crystal growth mechanism. This is in agreement with visual observations. The development of nuclei and their subsequent growth were only observed at a relative supersaturation greater than a value of 0.67 at 80°C. Although spiral growth was not observed on the crystals, the existence of these cannot be dismissed because the resolution of the optical microscope may have been insufficient to resolve them.

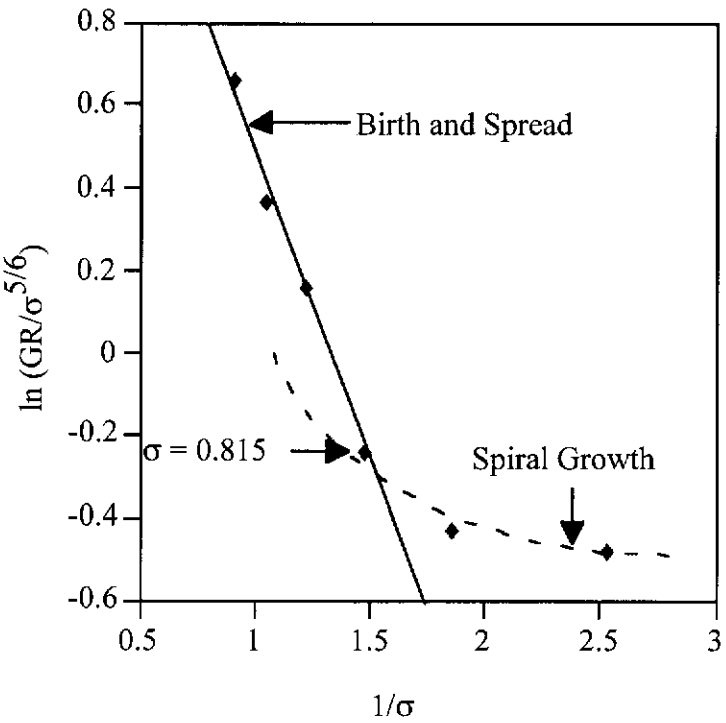

Figure 5.16 Plot of $\ln\left(GR/\sigma^{5/6}\right)$ *versus* $1/\sigma$ *for Basal Face*

The simultaneous formation of multiple nuclei before the complete spread of existing nuclei and the formation of nuclei on top of existing ones is possible for the birth and spread model (Mullin, 1994). To investigate if this phenomenon is occurring in this system, plots of $\ln\left(GR/(\sigma+1)^3\left(\ln(\sigma+1)\right)^{1/2}\right)$ for a mononuclear process and $\ln\left(GR/\sigma^{2/3}(\sigma+1)^{1/3}\left(\ln(\sigma+1)\right)^{1/6}\right)$ for a polynuclear process *versus* $1/\ln(\sigma+1)$ were carried out. These equations were given by Veesler and Boistelle (1994) to differentiate between mononuclear and polynuclear birth and spread mechanisms. Both these plots resulted in straight lines, indicating that the birth and spread model can be either a mononuclear or polynuclear process (Figure 5.16). Visual observations however, showed the formation of multiple nuclei but not the formation of nuclei on top of existing ones (Figure 5.6).

From the gradient of the plots, edge free energy values can be calculated. The edge free energy calculated for the mononuclear and polynuclear process are 4.3 ± 1.5 kJ/mole and 6.0 ± 1.5 kJ/mole, respectively.

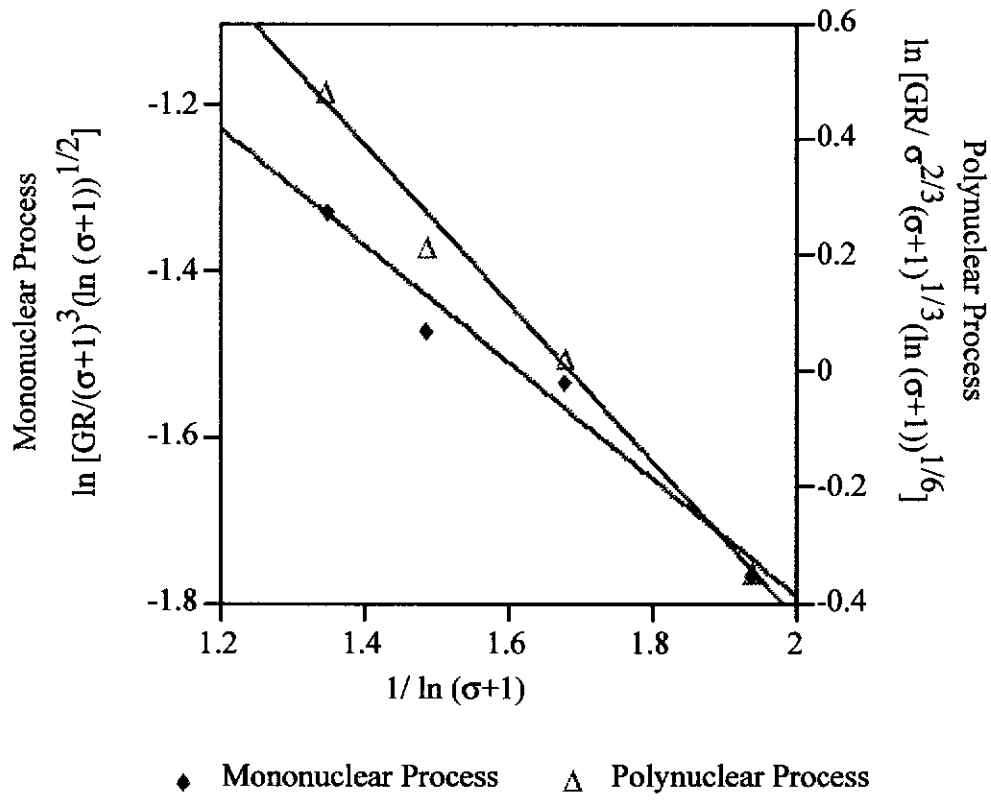

Figure 5.17 Natural Logarithmic Plots Showing Growth of the Basal Face may Occur by either Mononuclear or Polynuclear Birth and Spread Processes

5.2.3.3.2 Prismatic Faces

The prismatic faces of gibbsite are the {110} and the {100} faces. When considering the prismatic face (110), at first glance, the growth rates versus supersaturation curve may be fitted to either an exponential function ($GR = 0.127\ e^{2.725\sigma}$, correlation coefficient = 0.954) or a power fit ($GR = 1.864\sigma^{1.802}$, correlation coefficient = 0.880) (Figure 5.18), except for the point at a relative supersaturation of 1.09.

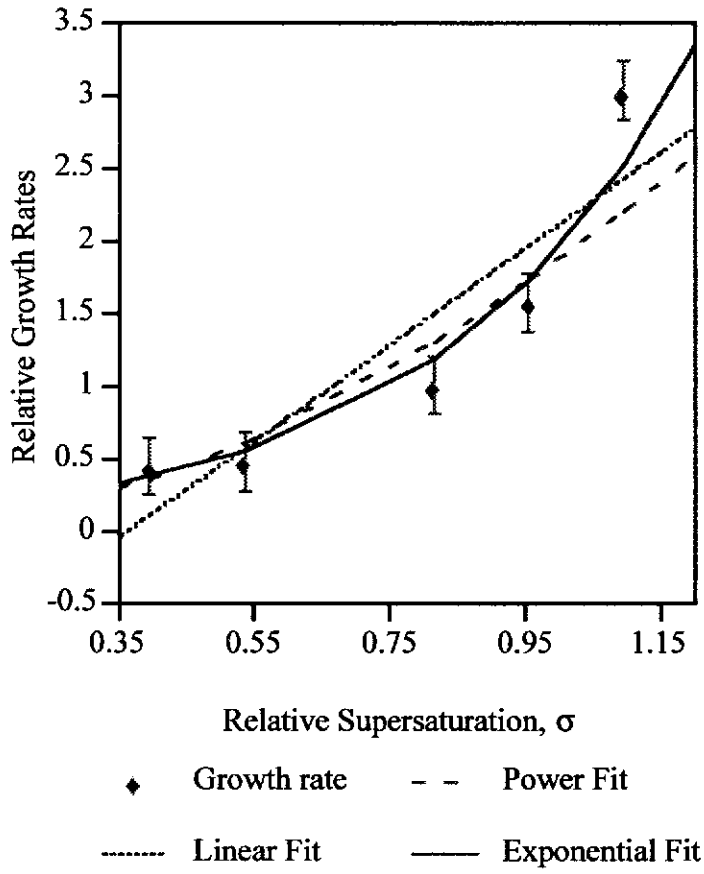

Figure 5.18 Growth Rate of (100) as a Function of Supersaturation

The results for the relative growth rates of the prismatic faces at a relative supersaturation of 1.09 were inspected and found to be exceptionally high. If the result from this level of relative supersaturation is ignored, then the data are consistent with the growth of the prismatic faces following a spiral growth (BCF) mechanism because of the non linear plot obtained $\ln\left(GR/\sigma^{5/6}\right)$ *versus* $1/\sigma$ (Figure 5.20 and Figure 5.21). At the highest level of supersaturation studied (σ = 1.09), spiral growth is considered not to be the primary mechanism operating, and the growth rates cannot be predicted by using the BCF model. Possible explanations for the higher than predicted growth rates for this level of relative supersaturation are discussed below.

The growth rate at a relative supersaturation of 1.09 at 80°C was found to be exceptionally high. The experiment at this level of relative supersaturation was repeated and yielded the same results. Figure 5.19 shows the plot of growth rate with time of the prismatic faces, initially showing the constant growth rate at a relative supersaturation of 0.81. Upon changing the liquor from one with a relative supersaturation of 0.81 to another with a relative supersaturation of 1.09 at 80°C at 1.67 hours (100 minutes), a time dependent (increasing) growth rate was recorded. A possible explanation for this is that at this level of supersaturation, roughening of the crystal occurs. With this, the presence of more new surfaces on the crystal faces results in faster than expected growth rates. Roughening was not observed for the basal face. However, since the growth of the basal face occurs via the birth and spread mechanism, the presence of the two dimensional nuclei on the surface and, hence the presence of new active sites, implies that no dramatic increase in growth rate will be observed on roughening.

The growth rate equations used previously have been simplified to exclude the surface area of the crystals, or the surface area has been assumed to be constant at an arbitary value of one. Equation 33 is the growth rate equation for the spiral growth model, incorporating the surface area term (A) for the spiral growth model.

$$GR = k_o A \sigma^2 \exp\left(\frac{-\Delta G}{RT}\right) \qquad (33)$$

The relative growth rate of the (100) face obtained for a relative supersaturation of 1.09 is 3.03 μm/hour, while the predicted growth rate at the same relative supersaturation is 2.01 μm/hour, implying that the surface area has increase by 50% during the roughening process.

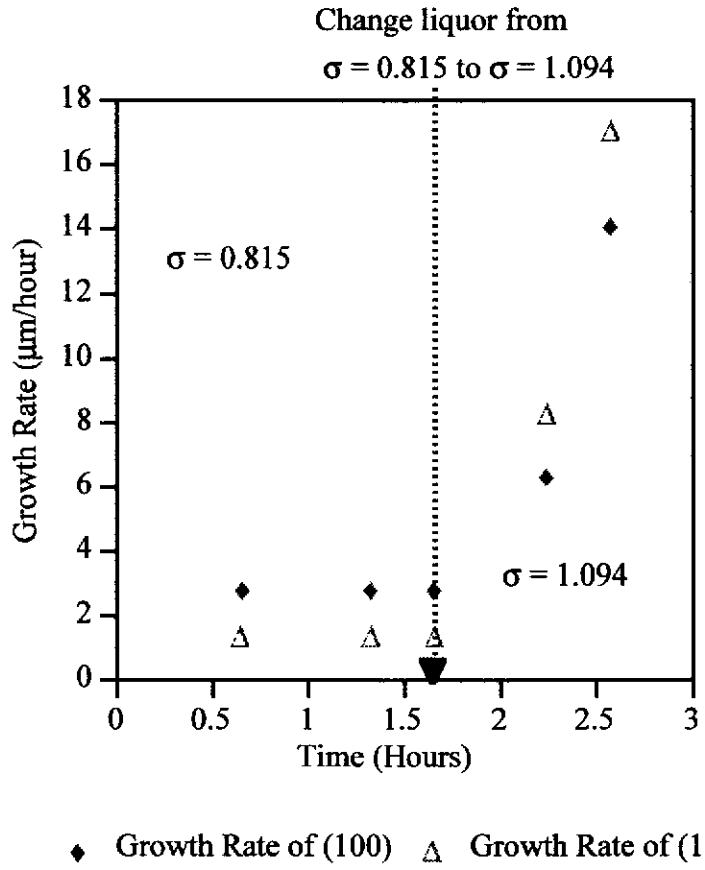

Figure 5.19 Increasing Growth Rate of Prismatic Faces at a "Constant" Relative Supersaturation of 1.09

Another possible explanation for the higher than predicted growth rate is the formation of a more ordered species in solution at the higher A/C value. The presence of another species apart from the tetrahedral aluminate unit $Al(OH)_4^-$ has been identified by Watling (1996). It is possible that this species has a more active role in the crystallization process when compared to the tetrahedral aluminate ion, hence a faster growth rate results. This implies that the terms used to describe supersaturation have to be redefined to incorporate these changes.

At present, the relative supersaturation is defined by Equation I. The proposed supersaturation term, incorporating the formation of new species is given below

(Equation 34). This implies that at higher A/C, the effective relative supersaturation is actually higher than that predicted using the former equation, due to the presence of a more active species. This results in a higher growth rate than predicted. It is currently not possible to test the hypothesis and quantify the function for the formation of new species due to insufficient data in the high A/C region. Furthermore, difficulties were encountered when attempting to generate these data due to excessive autonucleation for the liquors with greater than 0.750 A/C.

$$\sigma = \frac{A_{eff}/C - \left(A_{eff}/C\right)^*}{\left(A_{eff}/C\right)^*} \qquad (34)$$

where

A_{eff} = *Effective A*

$= \left(A_1 + A_2\right)$

A_1 = *Concentration of tetrahedral aluminate ions, expressed as g/L* Al_2O_3

A_2 = *Concentration of new species, expressed as g/L* Al_2O_3

$= f(A)$, $\Rightarrow 0$, *when* σ *decreases below 0.81 at* $C = 200$

Figure 5.20 and Figure 5.21 are plots of $\ln\left(GR/\sigma^{5/6}\right)$ *versus* $1/\sigma$ for the (100) face and (110) faces, respectively. The non linear plots indicate that the growth mechanism of the prismatic faces do not follow the either the mononuclear or polynuclear birth and spread models and growth occurs via a spiral growth mechanism.

Visually, the during the growth of the prismatic faces, the formation of two dimensional nuclei was not observed and the growth process was seen as elongation of the face, hence birth and spread was dismissed as the mechanism for growth. Furthermore, the existence of emergent spirals on the prismatic faces have been observed, indicative that they may be involved in their growth mechanism (Friej *et al.*, 1997).

On both plots (Figure 5.20 and Figure 5.21), a monotonic decay curve may be fitted though the data points, except for the point at 2.5, where the relative supersaturation is 0.40, however this is within experimental errors due to the larger errors associated with measuring very slow growth rates at the lower supersaturations.

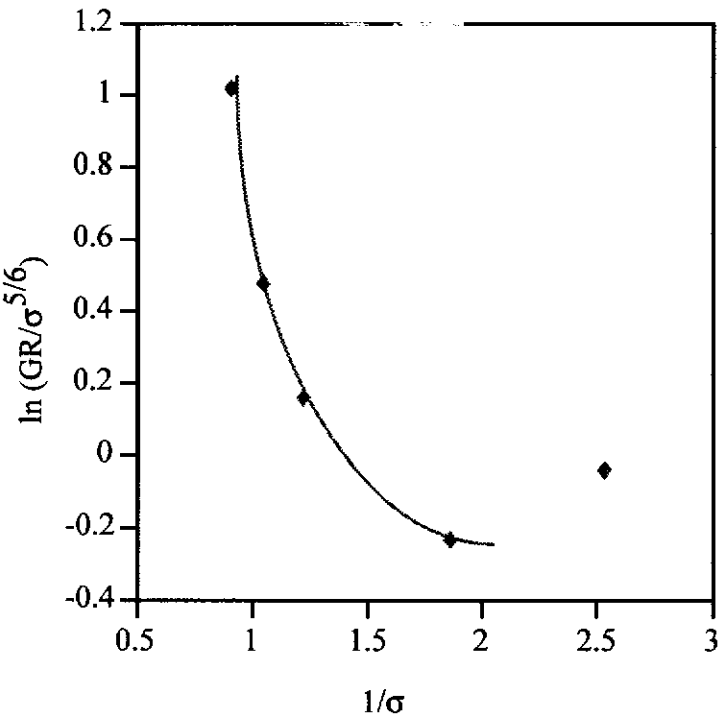

Figure 5.20 Plot of $\ln\left(GR/\sigma^{5/6}\right)$ *versus* $1/\sigma$ *for the (100) Face*

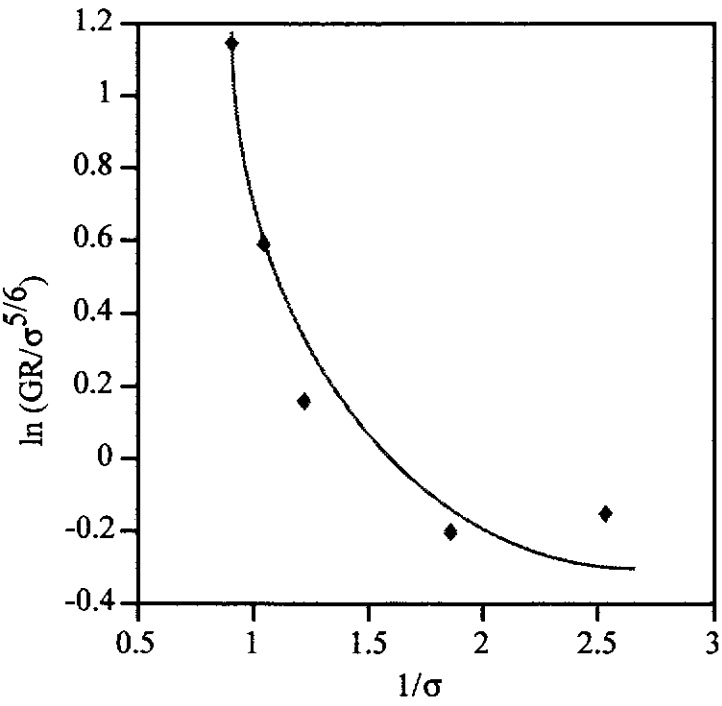

Figure 5.21 Plot of $\ln\left(GR/\sigma^{5/6}\right)$ *versus* $1/\sigma$ *for the (110) Face*

5.2.3.4 Activation Energies Calculated from Effect of Temperature at Constant Supersaturation Experiments

5.2.3.4.1 Activation of the Prismatic Faces

To calculate the activation energy of growth on the prismatic crystal face, the growth mechanism is assumed to be spiral growth and the generalised equation for spiral growth $GR = k_T\sigma^2$ where $k_T = k_0 \exp\left(-\Delta G/RT\right)$ is used. An Arrhenius plot $\ln k_T$ *versus* $1/T$ (Figure 5.22) gave straight lines from which the activation energies for the individual crystal faces and their corresponding kinetic coefficients were obtained from the gradient and intercepts, respectively. The errors were obtained from the errors in the gradient of the Arrhenius plot.

Table 5.3 gives the activation energies and kinetic coefficient calculated for the individual prismatic faces. These values are comparable to those reported in literature where an activation energy of 111 ± 24 kJ/mol was reported to be an average of several models (Veesler and Boistelle, 1994). The large value obtained for activation energies implies that growth occurs via a surface controlled mechanism.

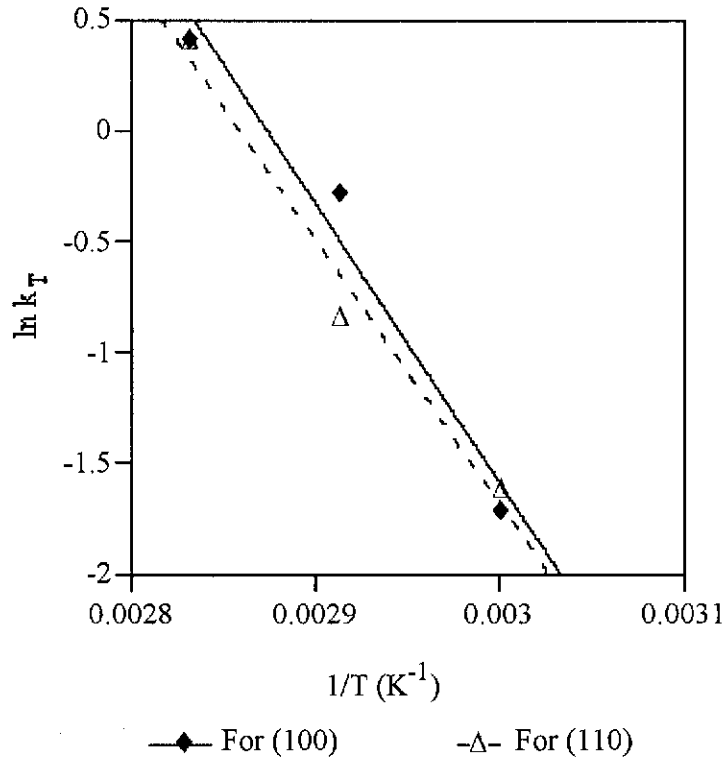

Figure 5.22 Arrhenius Plot to Determine Activation Energy and Kinetic Coefficient of Individual Prismatic Faces

Table 5.3 Activation Energy for Individual Crystal Faces of Gibbsite

Crystal Faces	Activation Energy, ΔG	Kinetic Coefficient, k_0
(100)	104.5 ± 19.5 kJ/mole	4.88×10^{15} μm/hour
(110)	99.5 ± 13.2 kJ/mole	7.41×10^{14} μm/hour

Using the activation energies and kinetic coefficient given in Table 5.3, the growth rates of the individual crystal faces of gibbsite at a relative supersaturation of 0.81 (0.650 A/C, 200 C) at 80°C are calculated and given in Table 5.4, showing the similarities in their growth rates. Figure 5.22 gives a comparison between the experimental growth rates as a function of supersaturation and those predicted using the activation energy and kinetic coefficient calculated from the effect of temperature at constant supersaturation experiments for the (100) face. Similar results were obtained for the (110) face.

Table 5.4 Calculated Growth Rates for Individual Crystal Faces

Crystal Face	Growth Rate (μm/hour)
(100)	1.13
(110)	0.92

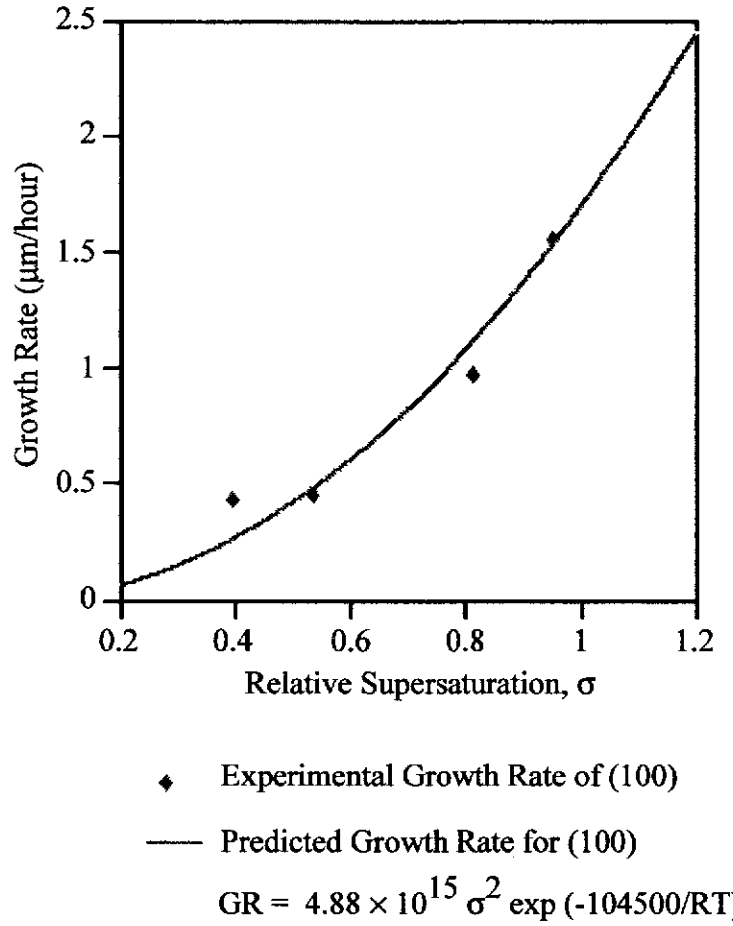

Figure 5.23 Comparison Between Experimental Results Obtained and Predicted Growth Rates for (100) Face

5.2.3.4.2 Activation Energy and Free Energy for Critical Nucleus Formation on the Basal Face

The crystals used for the determination of the growth rate of the basal face are placed such that they are viewed perpendicular to the [001] (see Figure 5.8). For this to occur, elongated hexagonal prisms are used. When determining the activation energy and kinetic coefficient for the basal face, data can be obtained simultaneously for a prismatic face of the crystal. However, in these cases, the exact identities of the prismatic face are unknown. The activation energy and kinetic coefficient obtained for these elongated hexagonal prisms are given in Table 5.5. Comparing the activation energy obtained here with those obtained for the individual prismatic faces shows

that they are same within experimental errors. This shows that although there is a variation in the morphology of the gibbsite crystals used, (elongated hexagonal prisms used for the basal face calculations and hexagonal plates used for the individual prismatic faces calculations) the morphology of the crystal does not affect the activation energy of the growth process.

Table 5.5 Activation Energy and Kinetic Coefficient for Prismatic Face

Activation Energy, ΔG	Kinetic Coefficient, k_0
86.9 ± 13.8 kJ/mol	1.17×10^{13} μm/hr

When attempting to calculate the activation energy for the basal face, the question arises as to which mechanism of growth to use. Results from previous experiments (Section 5.2.3.3.1) showed that a change in crystal growth mechanism occurs at a relative supersaturation of 0.67 at 80°C. It is unknown if this threshold is valid for all temperatures, hence more work in determining the relative supersaturation level at which the growth mechanism changes for the different temperatures is required. However, for the purpose of this work, both the spiral growth (BCF) model and the birth and spread models for a polynuclear process will be considered separately when calculating the activation energy and the kinetic coefficient. Only polynuclear processes will be considered here because visual observations indicate that this is the process operating.

Figure 5.24 shows the Arrhenius plot used in the calculation of the activation energy of the basal face, using the spiral growth model. The activation energy and kinetic coefficient obtained from this plot are tabulated in Table 5.6.

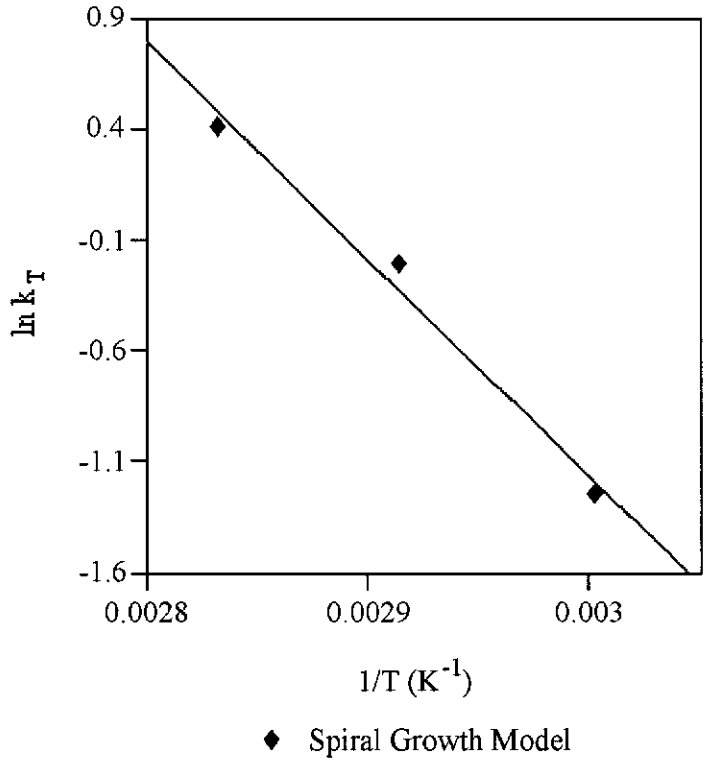

Figure 5.24 Arrhenius Plot to Determine Activation Energy and Kinetic Coefficient of Basal Face

Table 5. 1 Activation Energy for the Growth of the Basal Face

Model	Activation Energy, ΔG	Kinetic Coefficient k_0
Spiral Growth (BCF)	81.4 ± 10.7 kJ/mole	1.77×10^{12} μm/hr

Using the values for activation energy and kinetic coefficient obtained from the BCF model, a growth rate equation can be derived and the resulting growth rates predicted using this equation are compared with those obtained from the effect of supersaturation of growth rate experiments (Figure 5.25).

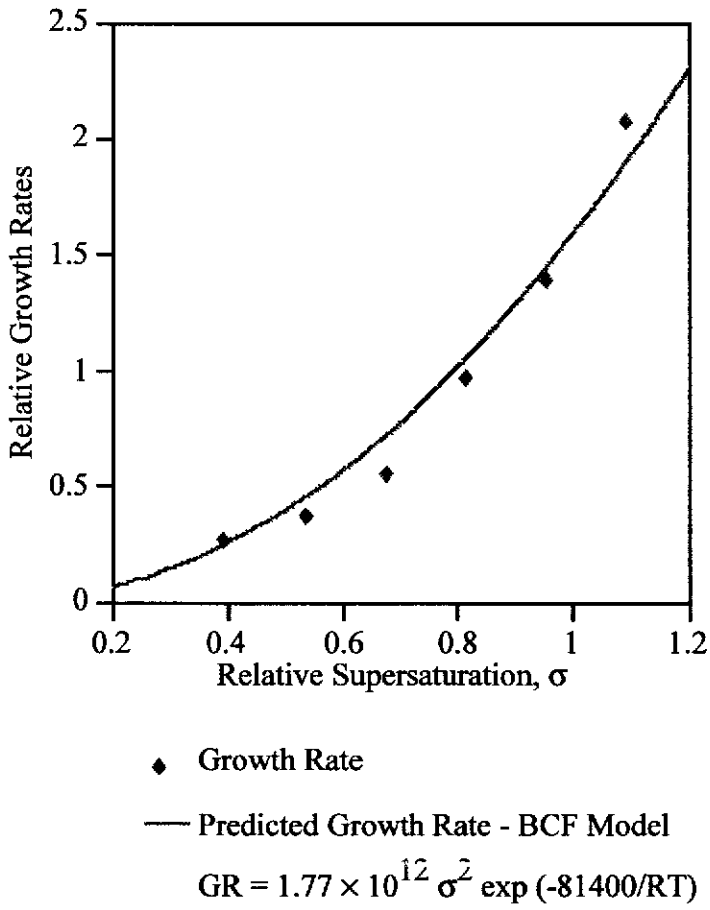

Figure 5.25 Comparison between Predicted (BCF Model) Growth Rates and Experimental Growth Rates of the Basal Face

When considering the birth and spread models, the free energy of critical nucleus formation (ΔG^*) may be calculated from the appropriate natural logarithmic plots of the models given by Gilmer and Bennema (1972), Madsen and Boistelle (1979) and Hillig (1966). These plots are given in Figure 5.26, and the ΔG^* and k_0 calculated are tabulated in Table 5.7.

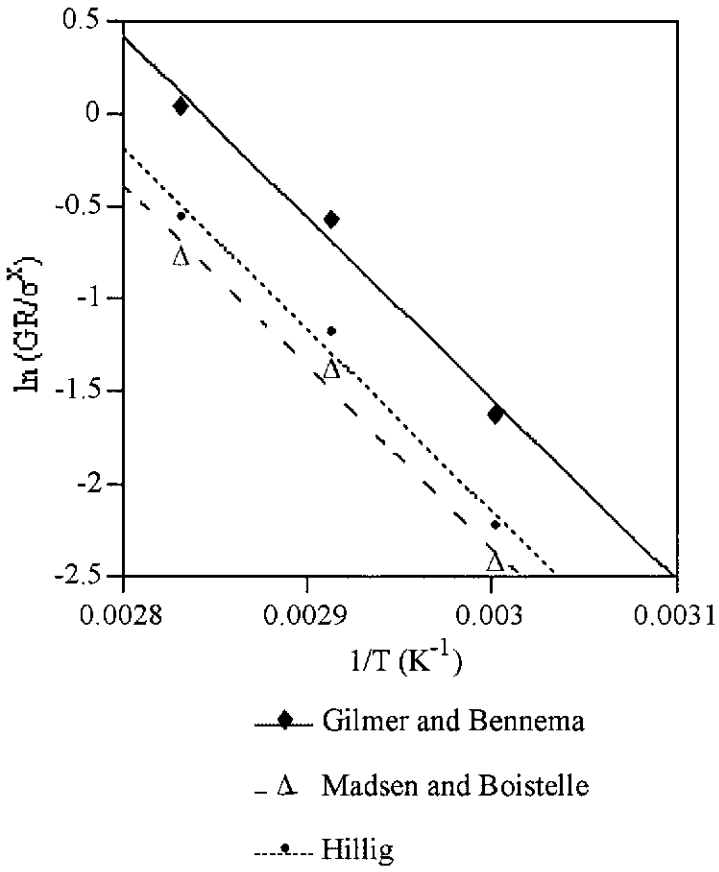

Figure 5.26 Natural Logarithmic Plots Used to Calculate ΔG for Polynuclear Birth and Spread*

Table 5.7 ΔG^* and K_0 Calculated Using Various Models for Polynuclear Birth and Spread.

Models	ΔG^* (kJ/mol)	k_0 (μm/hr)
Gilmer and Bennema (1972) $GR = k_0 (\sigma + 1)^{1/6} \sigma^{2/3} \exp\left(-\frac{\Delta G}{RT}\right)$	81.34 ± 10.7	1.22×10^{11}
Madsen and Boistelle (1979) $GR = k_0 (\sigma + 1)^{1/2} \sigma^{2/3} \exp\left(-\frac{\Delta G}{RT}\right) \cdot \exp\left(\frac{\sigma + 1}{3}\right)$	81.34 ± 10.7	5.45×10^{12}
Hillig (1966) $GR = k_0 (\sigma + 1)^{1/6} \sigma^{2/3} \exp\left(-\frac{\Delta G}{RT}\right) \cdot \exp\left(\frac{\sigma + 1}{3}\right)$	81.34 ± 10.7	6.65×10^{11}

Although these numbers for the free energy and kinetic coefficients look similar, differences are observed when attempting to use them to predict the growth rate dependence on supersaturations (Figure 5.27). However, when attempting to predict the effect of relative supersaturation on growth rates at 80°C using the birth and spread model, only the growth rates predicted for a relative supersaturation of 0.81 (the relative supersaturation at which experiments were carried out) and 0.95 matched those obtained experimentally.

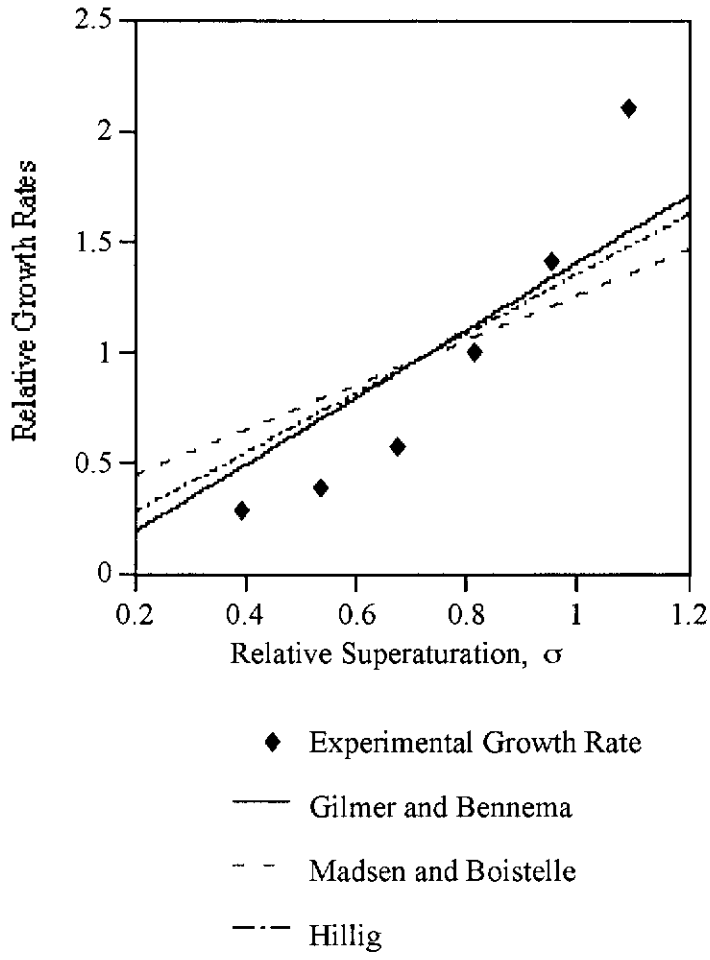

Figure 5.27 Comparison between Experimental Growth Rates and Predicted Growth Rate Using Various Polynuclear Birth and Spread Models

It is believed that the free energy for the critical nucleus formation obtained at 0.81 is the energy for the growth process which occurs as a combination of the birth and spread and spiral growth process. The activation energy at any supersaturation for the basal face can be calculated using given as Equation 35.

$$E_{total} = A \cdot \Delta G^{*}_{birth\ and\ spread} + B \cdot \Delta G_{spiral\ growth} \qquad (35)$$

where

ΔG^{*} = *Free energy for critical nucleus formation*

ΔG = *Activation energy for spiral growth process*

A = *Proportion of growth by birth and spread mechanism (decreasing with increasing* σ*)*

B = *Proportion of growth by spiral growth mechanism (increasing with increasing* σ*)*

Hence at $\sigma = 0.81$

$$81.34 = A \cdot \Delta G^{*}_{birth\ and\ spread} + B \cdot \Delta G_{spiral\ growth}$$

$A > B$, *since birth and spread is the dominant mechanism by which growth occurs*

5.2.3.5 Effect of Arabinitol on Growth Rate

Arabinitol has been found to inhibit the growth of the basal face preferentially and this results in the formation of gibbsite crystals with a hexagonal tablet shape (Section 3.3). The effects of arabinitol on the growth rate of individual crystal faces relative to standard conditions are given in Table 5.8, showing preferential inhibition of the basal face, followed by the (100) and (110) faces. The values given for the growth rates are typical values obtained for these experiments and are comparable to the findings from the bulk experiment where the presence of 1 mmol of arabinitol was found to reduce the yield of gibbsite to 52%.

The change in the relative growth rate of the basal face with respect to the prismatic faces implies that a change in morphology would be expected when growth occurs in the presence of a low concentration of arabinitol. Under standard conditions, the ratio of the growth rates of the basal face to the prismatic faces is one, while the same

ratio is 0.34 in the presence of arabinitol, predicting the formation of large hexagonal tablets. The morphology of the crystals formed consisted of large hexagonal tables, similar to those formed in the presence of 10 mmol of arabinitol in bulk experiments (see Figure 3.18). The differences in the relative growth rates of the prismatic faces resulted in the formation crystals where the (100) is more dominant. This change is not as pronounced as that observed between the prismatic and basal faces, due to the smaller difference between their relative growth rates.

Table 5.8 The Effect of Arabinitol on the Growth Rates(GR) of Individual Crystal Faces.

	Prismatic Faces		Crystal on its side	
	(100)	(110)	Basal	Prismatic
Standard	0.82	0.82	0.82	0.82
Arabinitol (10 mmol/L)	0.41	0.61	0.21	0.61
$\frac{GR_{Arabinitol}}{GR_{Standard}}$	0.50	0.75	0.25	0.75

5.2.3.6 The Effect of Other Impurities

The growth rate was found to increase with time under constant relative supersaturation in the presence of the silicon gaskets used in the *in situ* cell. This effect was not seen when EPDM was used. The materials used for the gaskets have been described in Section 4.2.2.1. It is thought that the increasing growth rates at constant supersaturation may have been caused by impurities leached from the gaskets used in the *in-situ* cell.

Because of the small volume of the *in-situ* cell, the liquor could only be analysed prior to the experiment and at the completion of the experiment. Measurements were therefore made on a parallel batch of liquor prepared and treated under identical conditions. Within the period of observation, microscopically, the growth rate was observed to increase while macroscopically, the relative supersaturation was decreasing. An increase in growth rate with time with decreasing relative supersaturation is unexpected according to classical crystallization theories, as growth rate is proportional to supersaturation.

Figure 5.28 is a typical graph of the growth rates obtained for different faces of a gibbsite crystal in the *in situ* cell (0.650 A/C, 200 C at 80°C) The trends observed were the same (initial induction time, or a period of slow growth, followed by an increase in growth rates), with the absolute values for these rates varying between crystals.

The results obtained demonstrate that while liquor supersaturation decreases with time, decreasing the crystallization driving force, the growth rate continued to increase (Figure 5.28). It is reasonable to expect that the growth rate will level off and ultimately decrease with time, but this was not observed experimentally due to excessive nucleation which obscured the view of the crystal being studied after approximately 10 hours, and hence preventing experiments from being carried out long enough to test this.

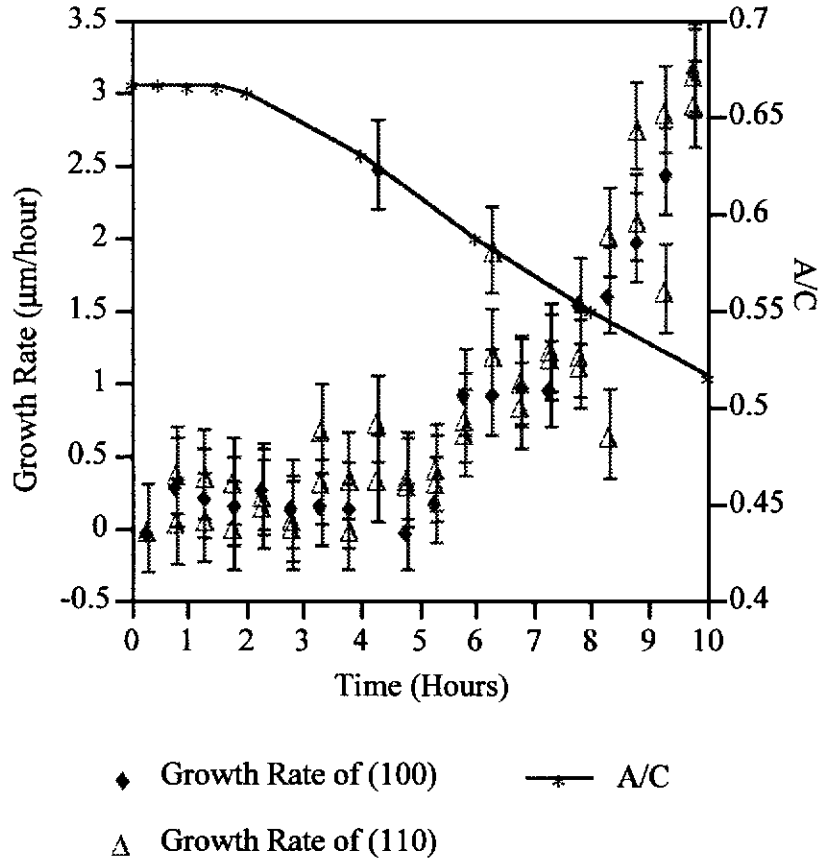

Figure 5.28 Effect of Leached Impurity on the Growth Rates of Gibbsite

Three factors may be responsible for the observed results. First, it is known that the seeded growth of gibbsite follows an induction period which is ascribed to the activation of the seed surface (Smith and Woods, 1993). It is possible that beyond that induction period, further activation continues, effectively increasing the growth rate despite the decrease in relative supersaturation. Secondly, it is possible that there are species which are involved in the rate limiting step of the growth process which are distinct from the dominant bulk species. The former could be increasing in concentration with time despite the overall decrease in liquor concentration, thus providing a greater driving force. Since this phenomenon was not observed in the pure system, and the seeds used were prepared in the same manner, these reasons cannot be used to explain the increasing growth rate. The theory of liquor restructuring was investigated further and will be discussed in the next section.

Finally, it is also possible that one or more species exist in the liquor that act as an inhibitor to crystallization. This was confirmed with macroscopic studies, where the presence of silicon gaskets was found to decrease precipitation yield by approximately 50%. If these inhibitors were surface active, during the course of crystallization, their concentration in solution would decrease, and hence a corresponding increase in the growth rate of gibbsite would be expected, as observed in this case. Similar behaviour could be induced by the presence of impurity ions such as Ca^{2+}, which is known to cause an initial period of apparent seed inactivity if present in the liquor (Cornell *et al.*, 1996).

5.2.3.7 Effect of Liquor Preparation on Precipitation Rates

The results of the investigation into the effect of liquor history on bulk precipitation rates in seeded systems are shown in Figure 5.29, which is typical of three independent experiments. In this section of the work, crystal growth and secondary nucleation are not differentiated, and only the total amount of gibbsite precipitated was measured as a change in A/C ratio. The results show that the "new" liquor has an induction time of approximately 120 minutes, followed by a period of precipitation. Ilievski et al. (1989) have shown induction time to have an inverse relationship to A/C, in that with a higher A/C a shorter induction time is observed. In these experiments, although the "aged" liquor started with a lower A/C, no induction time was observed. Since the seed used in both these cases is "active", the induction time observed in the "new" liquor may be ascribed to some liquor restructuring in the presence of gibbsite crystals; for example, an increase in the concentration of one or more species involved in the rate limiting crystallization steps. After approximately 200 minutes, the rate at which A/C decreases in the new liquor is greater than that of the aged liquor. This could be due to the higher amounts of fine nuclei or seed present in the liquor, caused by autonucleation during the induction time.

These experiments demonstrate that an increase in precipitation rate results from ageing a liquor. Complementary experiments were carried out to determine the effect of ageing on the growth rate of individual crystal faces. Although crystal growth was observed, difficulties were encountered when attempting to determine the growth rates of the crystals due to the formation of excessive nuclei which obscured the view of the crystals in the *in situ* cell in the first hour of the experiment.

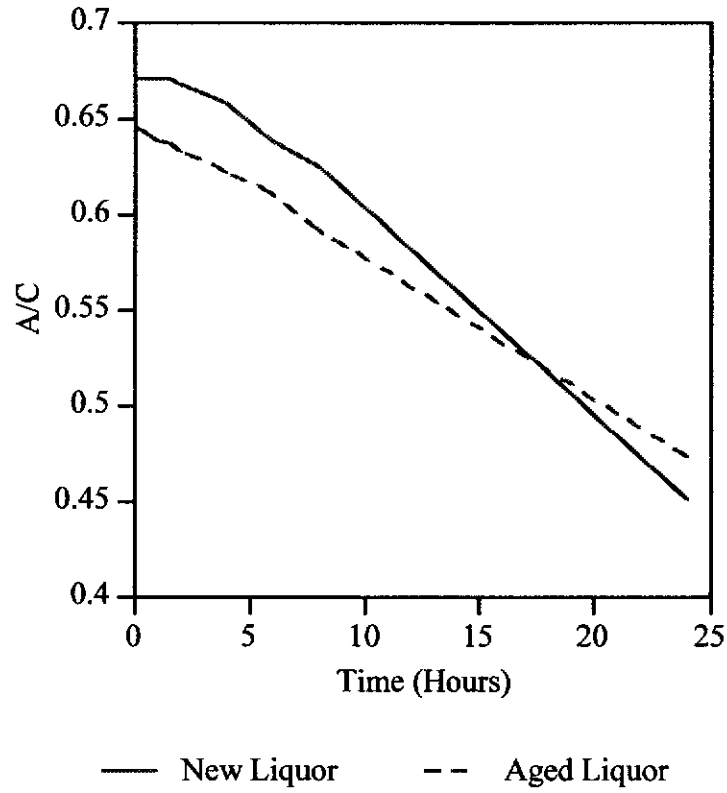

Figure 5.29 Effect of Ageing Liquor on the Rate of Change of A/C in the Presence of Seed

5.3. Overall Growth Rates Determined Using Rapid Dynamic Light Scattering (DLS)

In previously reported work (Smith and Woods, 1993 and Rossiter *et al*, 1996), using solution concentration and turbidity measurements, the end of the induction time is marked by a rapid decrease in concentration and increased turbidity. These measurements give no indication of whether these changes are due to secondary nucleation or growth, or a combination of both. Although the turbidity measurements gave an indication of the onset of secondary nucleation, data on particle number and size were obtained by sub-sampling. Rapid DLS developed by Tsukamoto (Tohoku University, Sendai, Japan) provides a technique for *in situ* measurement of particle size and number simultaneously. In rapid DLS, with the gibbsite system, the end of the induction time is identified by a sudden increase in particle numbers as a result of secondary nucleation.

The technique of DLS is based on the variations with time in the intensity of light scattered by particles in suspension. Information on the numbers and the diameters of these particles may be obtained by monitoring the intensity of the scattering light and the short term fluctuation in it, respectively. Commercially available DLS systems have been used successfully to analyse a wide range of materials (Nicoli and Elings, 1988) but have only been used for crystallization studies infrequently because the time taken for a measurement is generally long compared to reactions occurring in the precipitating system. This section of the work demonstrates the use of the newly developed technique of rapid DLS for the study of crystal growth and secondary nucleation.

5.3.1 Dynamic Light Scattering Theory

Dynamic light scattering utilises a laser beam to probe a small volume of suspended particles. As the particles undergo Brownian motion, interference between the scattered waves produces a fluctuation in intensity with time at the detector (Equation 36) (Nicoli and Elings, 1988). The rate at which the intensity fluctuates is related to the rate of diffusion of the suspended particles: the smaller the diameter the faster the diffusivity and the more rapid the "flicker" of light. This fluctuation can be quantitatively related to the distribution of particle diffusivities by obtaining its second order auto-correlation function (Equation 37), and information on the particle diameter may be obtained from the diffusion coefficient (D), by using the Einstein-Stokes equation (38) (Nicoli and Elings, 1988).

$$G_2 = \langle I(t).I(t + \Delta t) \rangle \tag{36}$$

$$\begin{aligned} Autocorrelation &= G_2 / \langle I \rangle^2 \\ g_2 &= 1 + exp\left(-2q^2 D\Delta t\right) \end{aligned} \tag{37}$$

$$D = kT/6\pi\eta r \tag{38}$$

G_2 = *Intensity light fluctuation*
$I(t)$ = *Intensity of light at time t*
q = *Difference between initial wave vector and final wave vector*
D = *Diffusion coefficient*
k = *Boltzman constant*
η = *Viscosity of solution*
r = *Radius of particle*
T = *Absolute temperature*

The method used to calculate relative particle numbers is based on the theory of static light scattering (Equation 39).

$$I_s = \frac{1}{\lambda^4 L^2} \times \left(\partial n / \partial C_g\right)^2 \times \frac{kT}{\left(\partial P / \partial C_g\right)} \times C_g \; P(X) I_o \tag{39}$$

where

k = *Boltzman constant*
T = *Temperature*
I_s = *Intensity of scattered light*
I_o = *Intensity of source*
λ = *Wavelength of laser light*
L = *Distance between detector and laser*
n = *Refractive index of particle*
C_g = *Molar weight concentration of particles*
P = *Pressure of penetration of solution*
$P(X)$ = *Intraparticle structure factor*

If we assume that $\left(\partial n / \partial C_g\right)^2$ is the same for all particles is solution, then

$$I_s \propto \frac{kT}{\left(\partial P / \partial C_g\right)} \times C_g P(X) \tag{40}$$

Thermodynamically, P may be expressed as

$$\begin{aligned} P &= C^* kT \\ &= \frac{C_g}{M} \times RT \end{aligned} \tag{41}$$

where C^* = *Number of particles per unit volume*
M = *Mass of particles*
R = *Gas constant*

Using an approximation of $\partial P / \partial C_g \approx P / C_g$, and $M \propto r^3$, where r is the radius of the particle, then

$$C^* \propto \frac{I_s}{P(X) r^6} \tag{42}$$

The intraparticle structure factor takes into account the shape of the particles. For a solid sphere, the structure factor is defined by Equation 43.

$$P(X) = \left[\frac{3}{X^3} \times \left(\sin X - X \cos X \right) \right]^2 \tag{43}$$

$$\text{where } X = r \times \frac{4\pi n}{l} \times \sin \frac{\theta}{2}$$

A summary of the theory of DLS is given in Figure 5.30.

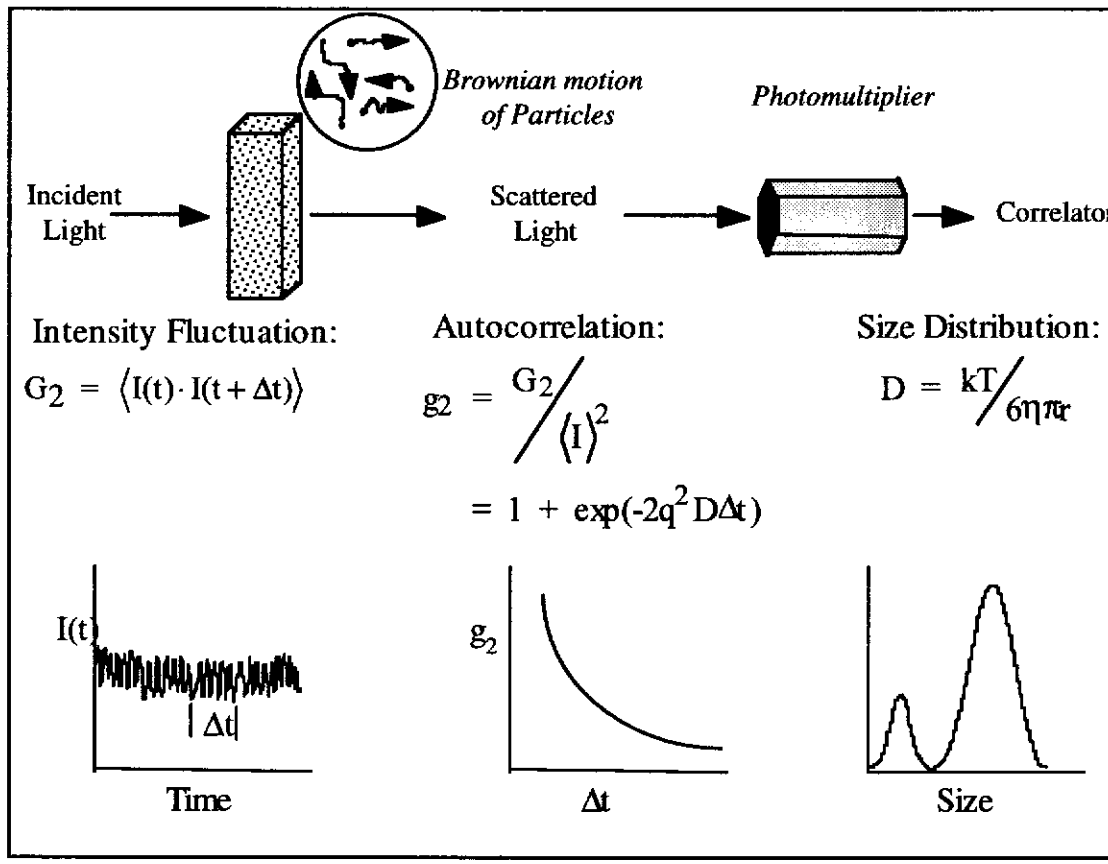

Figure 5.30 Dynamic Light Scattering Theory

5.3.2 Preliminary Experimental Results

Preliminary experiments performed to determine the amount of seed required, showed that the particle numbers from 50 μL of seed suspension (2 g/L) was not enough to obtain a good signal, while 100 μL resulted in short induction time. For these reasons, to determine the growth rates as a function of supersaturation, the amount of seed chosen for each experiment was chosen to be 75 μL.

The effect of liquor preparative history was also examined. The liquor must be preheated to 80°C prior to the addition of the seed suspension to avoid nucleation, however, if aged at 80°C for 16-24 hours, nucleation was observed rather than growth. This implies that for growth rate experiments the liquors have to be heated

prior to use to prevent nucleation, and for no longer than 1 hour to prevent solution restructuring. The effect of ageing liquors on induction time will be discussed in greater detail later (Section 5.3.4.4).

Preliminary experiments also indicate that agitation is required to prevent sample scaling and settling of the larger particles. However, the sample must not be agitated during DLS measurements as this would result in scattering from particles due to agitation rather than Brownian motion.

5.3.3 Experimental

5.3.3.1 Solution Preparation

All the sodium aluminate solutions used were prepared by dissolving aluminium wire in aqueous sodium hydroxide solution. The solutions were filtered through a 0.45 μm membrane to remove undissolved material and heated to 80°C, then refiltered through a 0.1 μm membrane before the addition of seed.

5.3.3.2 Seed Preparation

The seed was prepared by ageing a supersaturated sodium aluminate solution (A/C 0.850, C 200), at 90°C for 30 minutes. The seed was washed with hot deionised water, and then dispersed in water (2 g/L). For each experiment, the seed was added as a suspension to the hot aluminate solution at 80°C.

The seed was characterised using DLS to determine the particle size and SEM to determine the morphology of the crystal.

5.3.3.3 Growth Rate Determination

The effects of supersaturation on the growth rate and induction time were examined at constant seed charge (75 μL of seed suspension). All the experiments were carried out at 80°C.

A measurement was taken every 10 seconds to obtain the average particle size and relative particle numbers. The measurement routine is given in Figure 5.31, and this was repeated for 2 hours.

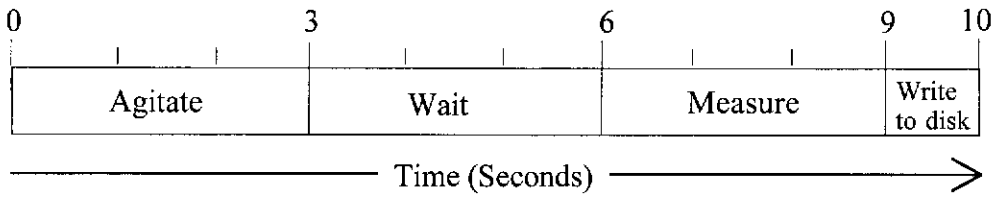

Figure 5.31 Measurement Routine for DLS

All DLS experiments were carried out in a clean room, hence precautions were taken to exclude dust from the experiments, ensuring that the onset of secondary nucleation is due to the presence of seed added to the system and not other external factors.

5.3.4 Results and Discussion

5.3.4.1 Seed Characterisation

The seed prepared by the method described above consisted mainly of single hexagonal crystals with particle radii of 200 nm. This seed was identified to be gibbsite by its X-ray diffraction pattern.

5.3.4.2 Identification of Crystal Growth and Secondary Nucleation by Rapid Dynamic Light Scattering

Accurate information on particle numbers and sizes has been obtained simultaneously, from *in situ* experiments. These could not be obtained by the use of a conventional DLS systems because the duration of such measurement (2 - 3 minutes) is too long; these have been successfully measured here using rapid DLS (complete measurement in less than 3 seconds).

Typical results showing secondary nucleation and crystal growth in a crystallizing system are given in Figure 5.32 and Figure 5.33, respectively. In the case of secondary nucleation (Figure 5.32), an induction time was observed, followed by a rapid rise in particle number with a simultaneous decrease in average particle size, which can be ascribed to the formation of new particles. The decrease in average particle size is due to the appearance of large numbers of small newly formed nuclei. The duration of the induction time is less than the values reported in the literature (Smith and Woods, 1993, Rossiter *et al.*, 1996). This is understandable, because the length of a measured induction time is a function of the sensitivity of the instrument used (Rossiter *et al.*, 1996).

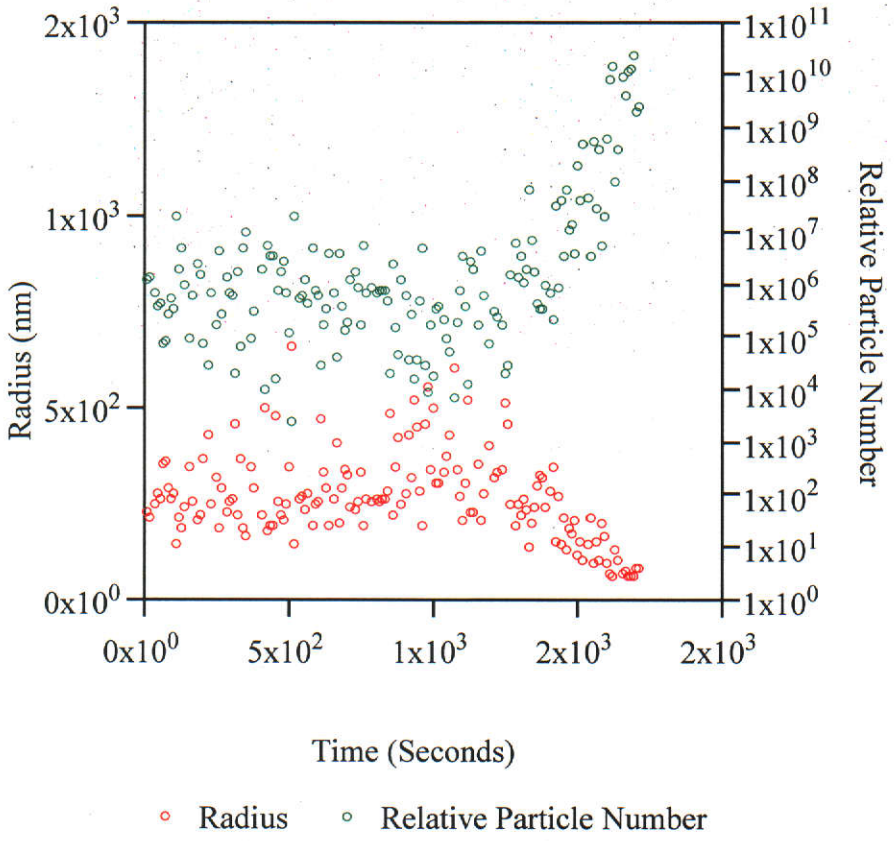

Figure 5.32 Secondary Nucleation Shown by an Increase in Relative Particle Number with Decreasing Average Particle Size

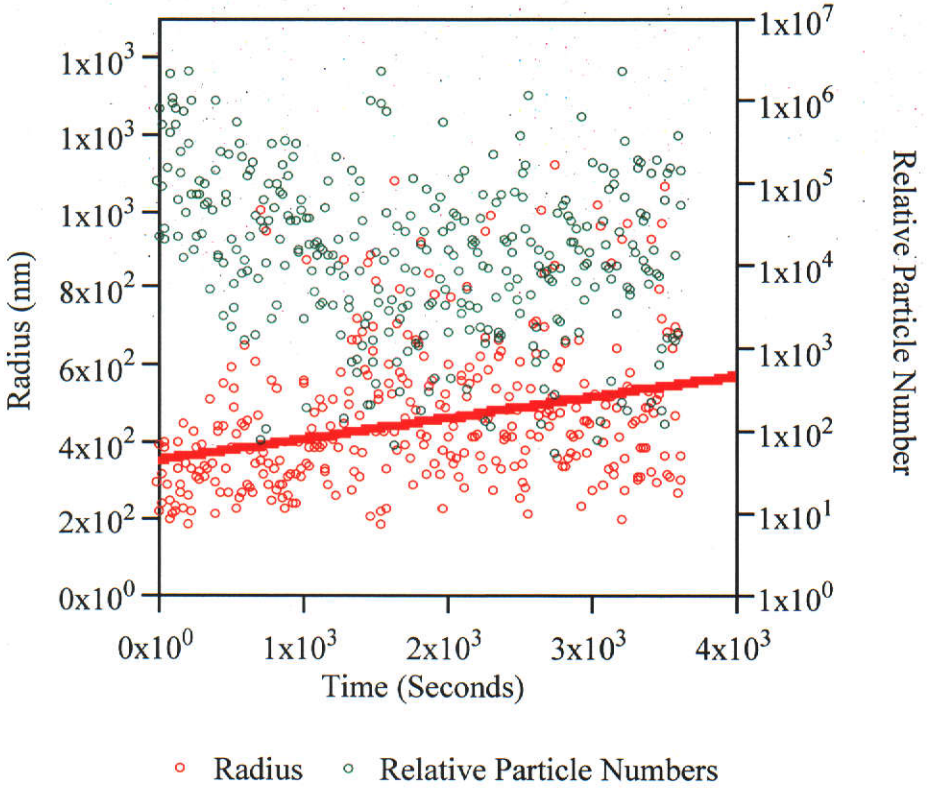

Figure 5.33 Crystal Growth Denoted by an Increase in Average Particle Size while Relative Particle Numbers Remains Constant

5.3.4.3 The Effect of Supersaturation on Growth Rates

The variation in growth rate as a function of supersaturation is shown in Figure 5.34. From general crystal growth theory, the growth rate (GR) may be expressed as a function of relative supersaturation (σ), $GR = k\sigma^n$. A growth order of $n = 1$ is indicative of a birth and spread mechanism, and a growth order of $n = 2$, a quadratic relationship, indicates that a spiral growth mechanism is controlling the kinetics. By applying curve fitting software to the available growth rates obtained from DLS measurements, the linear relationship, $GR = 0.721\sigma - 0.282$ gave a correlation coefficient of 0.980, while $GR = 0.050\sigma^{2.697}$ resulted in a correlation coefficient of 0.982. It is therefore not possible to distinguish between the crystal growth models

on this basis because of the small range of supersaturation available for the study of gibbsite crystal growth. It is also not possible to extend the supersaturation range, since it is physically impossible to prepare aluminate solutions with higher relative supersaturation values and the growth rates at lower levels are too slow to permit experiments to be carried out in reasonable times.

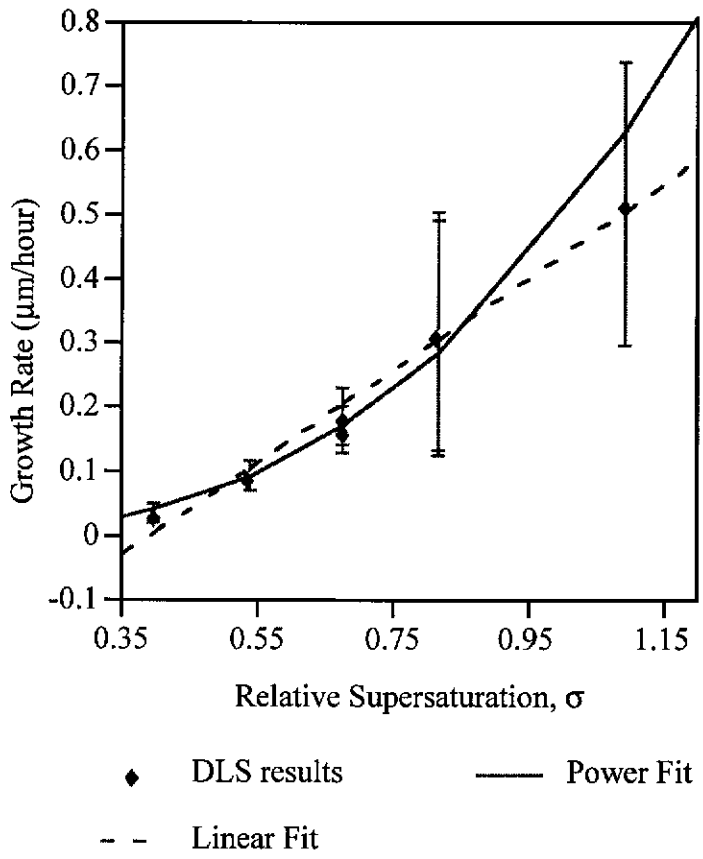

Figure 5.34 Growth Rate as a Function of Relative Supersaturation

The growth rates obtained from DLS measurements were then compared to supersaturation dependencies as predicted by the models developed by White and Bateman (1988) and Veesler and Boistelle (1994) (Figure 5.35). Although the literature results obtained from gibbsite models were up to a factor of 10 higher, the trends observed were similar to those obtained from the DLS measurements. The different order of magnitude in the growth rates may be due to the fact that the

growth rates obtained in this section of the work were those of growth during the induction period rather than after, as quoted in the literature (White and Bateman, 1988, Veesler and Boistelle, 1994). Smith and Woods (1988) have reported that slow growth occurs during this period, but the rate has not previously been measured.

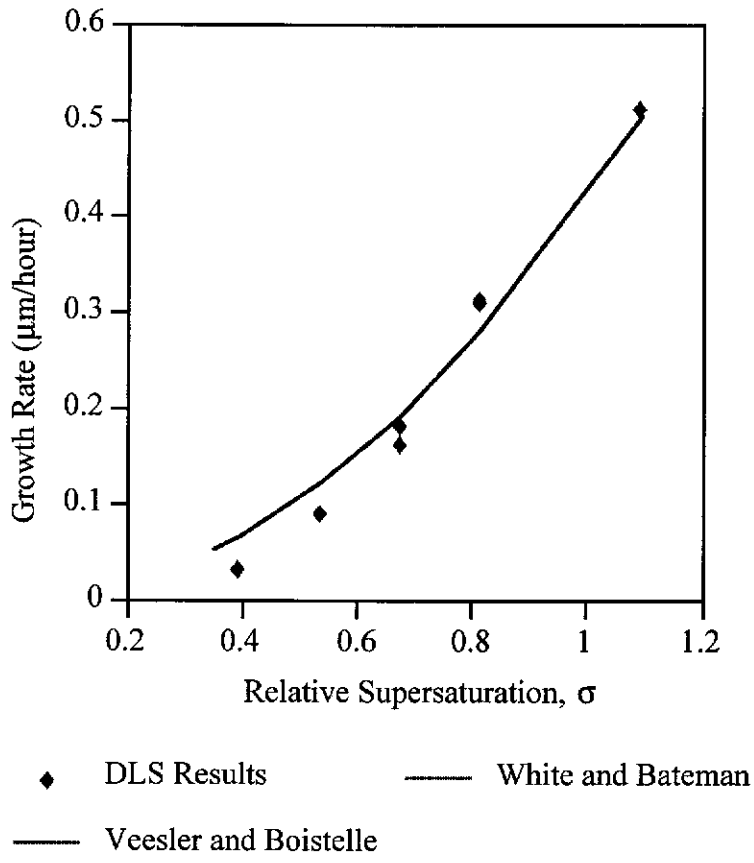

Figure 5.35 Growth Rate as a Function of Supersaturation - Veesler and Boistelle Model and White and Bateman's Model

Note: The curves predicted by the models of Veesler and Boistelle, and White and Bateman overlay each other

Comparison between the experimental data and those predicted using the models developed by White and Bateman (1988) and Veesler and Boistelle (1994) as given in Figure 5.35, show that growth is likely to occur via a spiral growth mechanism. However, to examine if growth occurs via a birth and spread mechanism or a spiral growth mechanism, $\ln\left(GR/\sigma^{5/6}\right)$ *versus* $1/\sigma$ is plotted (Figure 5.36) (see Section 5.2.2.4.1). This shows a linear relationship which implies that growth occurs by a birth and spread mechanism.

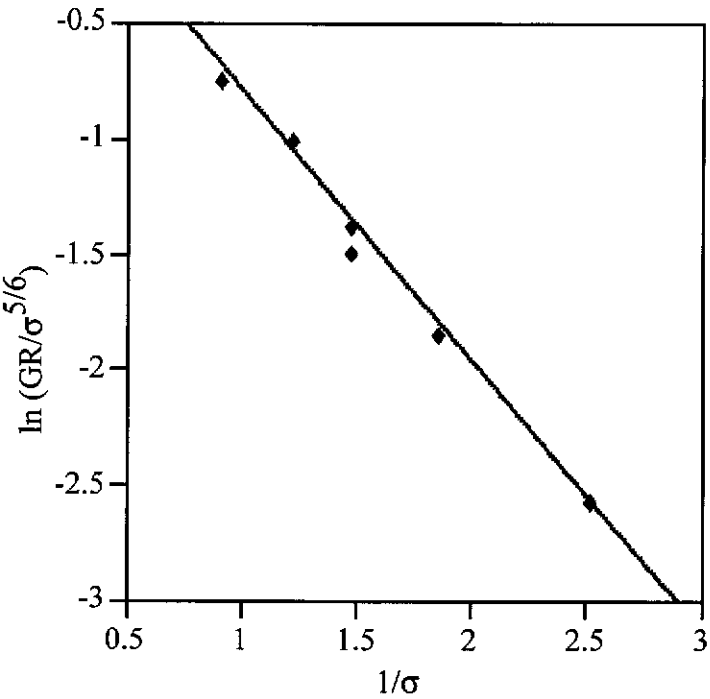

Figure 5.36 Plot of $\ln\left(GR/\sigma^{5/6}\right)$ *versus* $1/\sigma$ *Showing a Linear Relationship Indicative of Birth and Spread Growth Mechanism.*

To examine if the birth and spread mechanism is plausible, it is usual to calculate the edge free energy (ϕ) for the system. Several models exist that can be used calculating the edge free energy. The equations used here are those given in Chapter 1 for the mononuclear process (Equation 19) and the polynuclear process (Equation 20).

The appropriate logarithmic plots were used (Figure 5.37) to determine if growth is occurring via a mononuclear or polynuclear birth and spread mechanism. As shown in Figure 5.37, the results appear to fit the polynuclear model (correlation coefficient = 0.984) better than the mononuclear model (correlation coefficient = 0.936), implying that growth probably occurs via a polynuclear birth and spread process.

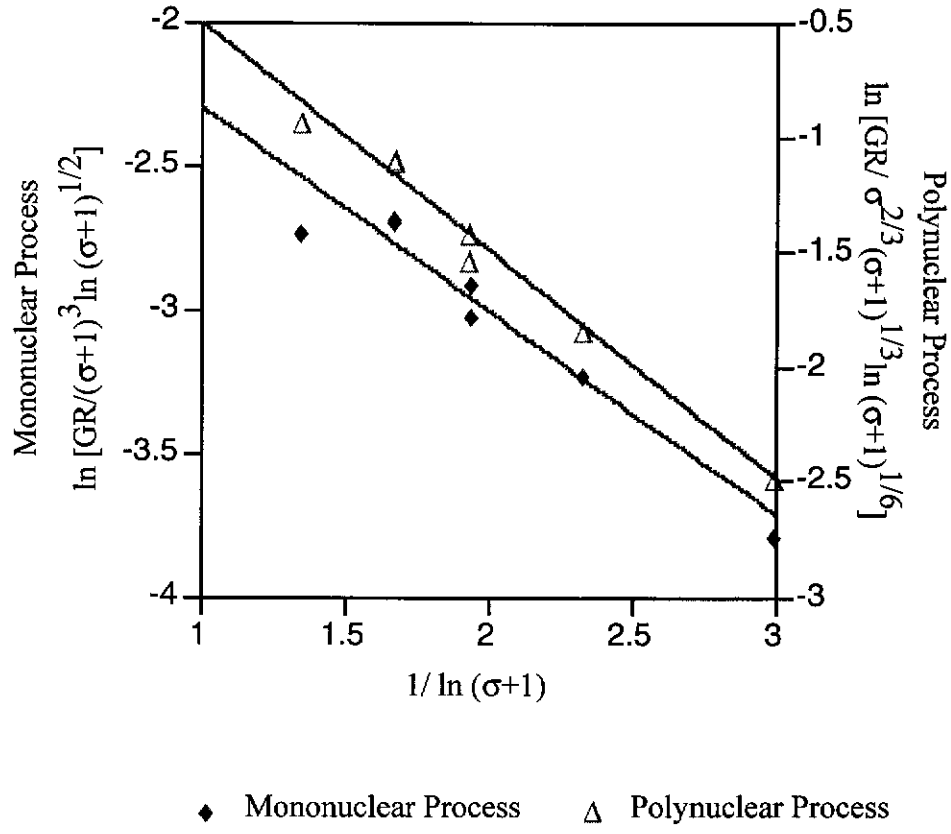

Figure 5.37 Logarithmic Plots Used to Determine Edge Free Energy

In the calculation of edge free energy, by fitting the experimental dependence of growth rate on supersaturation to Equations 19 and 20, values of 4.3 ± 1.5 kJ/mole and 6.1 ± 1.3 kJ/mole were obtained for the mononuclear and the polynuclear processes respectively. The edge free energy calculated was two orders of magnitude higher than the value of 0.02 kJ/mole reported by Veesler and Boistelle (1994), and comparable with values reported for other ionic solids such as sodium chloride (0.1 kJ/mole), potassium chloride (2.2 kJ/mole) and potassium bromide (2.7 kJ/mole) (Gindt and Kern, 1968), as well as values obtained from the *in situ* optical microscopy experiments (4.3 ± 1.5 kJ/mole and 6.0 ± 1.5 kJ/mole for mononuclear and polynuclear processes respectively). The higher value, compared to that obtained by Veesler and Boistelle may be because the growth rate obtained here is for growth during the induction period, the time during which seed surfaces are reactivating (Smith and Woods, 1993). The energy required for the formation of a two dimensional nucleus will therefore be greater for the deactivated seed surface compared to seed surface during the growth phase, when active sites for growth are more abundant.

Another reason for favouring the birth and spread model is that complementary *in situ* optical microscopy experiments have revealed the development of two dimensional nuclei on the basal face followed by the spread of these during the growth process (Section 5.2.3.3).

It is therefore believed that overall growth of gibbsite during the induction time follows the birth and spread model for the following reasons:

- The edge free energy calculated is comparable to those obtained from *in situ* optical microscopy experiments, where birth and spread mechanism was visually observed; as well as being comparable to the values obtained for the edge free

energy of other ionic solids. The larger value obtained is expected for gibbsite, which is slow growing.

- Complementary microscopy experiments showed the development of surface features on the basal face and the subsequent growth of these layers, indicative of the birth and spread model.

- The seed crystal size in these experiments was of the order of 500 nm in diameter, an order of 100 time less than normal industrial seed crystal size. It is reasonable to expect that seed crystals of this size may be near perfect, and hence have low dislocation densities and thus a low source for step formation.

5.4. Summary

The growth of gibbsite has been successfully observed and its rate obtained by *in situ* techniques for a range of temperatures and supersaturations. Microscopical work showed the existence of growth rate dispersion in the gibbsite system, while the existence size dependency growth rate is still questionable.

When considering the growth of individual faces of the gibbsite crystals, only the growth of the individual prismatic faces and basal face can be observed and measured. The growth rate of the basal face was found to follow the spiral growth mechanism at a low supersaturation but a birth and spread mechanism at a higher supersaturation. This was confirmed visually with the emergence of nuclei on the basal face and their spread at higher supersaturations. Although spiral growth was not observed, this mechanism cannot be dismissed because it may not have been observed due to lack of resolution on the optical microscope. Logarithmic plots of Equations 19 and 20 suggest that growth may occur via mononuclear or polynuclear birth and spread.

However, images obtained showed that growth occur via a polynuclear process. Although nuclei do not form before the complete spread of existing ones, multiple nuclei may be found on the basal face of single gibbsite crystals.

In the calculation of the energetics for growth on the basal face, both the BCF and birth and spread models were considered. When comparing the experimental growth rates as a function of relative supersaturation with the growth rates predicted using either the BCF or birth and spread models, a better match was obtained with the BCF model. This however does not agree with visual observations, where the birth of nucei and their subsequent spread indicates that the growth process occurs via the birth and spread mechanism.

The prismatic face have a second order growth dependence on supersaturation, which suggests that these faces grow via a spiral growth mechanism. This is reinforced by the visual images in which two dimensional nucleus is not observed. Differentiation between the growth rates of the prismatic faces cannot be made due to insufficient resolution on the optical microscope. However, it is expected that the growth rates of the prismatic faces will be similar to each other, due to the similar atomic structures of their faces. The calculated activation energies also showed the similarities between the prismatic faces. The growth rate equations for the individual prismatic faces are given below as Equations 44 and 45.

$$GR_{(100)} = 4.88 \times 10^{15}\ \sigma^2\ exp\left(\frac{-104500}{RT}\right) \tag{44}$$

$$GR_{(110)} = 7.41 \times 10^{14}\ \sigma^2\ exp\left(\frac{-99500}{RT}\right) \tag{45}$$

The addition of arabinitol, however, showed that although the atomic structures of the prismatic faces are similar, they are sufficiently different to result in preferential inhibition of the (100) face over the (110). Arabinitol was also found to preferentially inhibit the basal face over both the prismatic faces.

Dynamic light scattering experiments showed that growth during the induction time exists, but at a rate approximately 10 times less than in the "normal" growth regime. Growth during this time is believed to follow the birth and spread mechanism and the edge free energy calculated for the gibbsite system indicates that it could be a mononuclear or polynuclear process that is occurring. The values obtained for the edge free energy are comparable with those obtained from *in situ* microscopy work as well as those reported in the literature for other inorganic solids. The edge free energy obtained for the polynuclear birth and spread model is 6.0 ± 1.5kJ/mole.

Chapter 6

Conclusions and Recommendations

1. Conclusions and Recommendations

Aluminium trihydroxide may take the form of bayerite, gibbsite or nordstrandite. The formation of bayerite is favoured at room temperature, while the formation of gibbsite is favoured at higher temperatures (above 50°C and below 100°C) when precipitated from alkali aluminate solutions. The formation of some nordstrandite was observed only when ageing sodium aluminate solutions at 70°C. The resulting morphology of bayerite was dependent on the method of preparation and ranged from single crystals to triangular prisms showing radial growth characteristics. These were quite unlike the somatoids described in the literature. Somatoid shaped bayerite may be formed by ageing amalgamated aluminium in water at room temperature while nordstrandite is formed by ageing amalgamated aluminium in aqueous ethylenediamine. The role of cations such as the sodium ion, or the role of pH in the stabilization of the gibbsite structure is raised, since ageing amalgamated aluminium in water at 80°C resulted in the formation of pseudo-boehmite, rather than gibbsite.

The morphology of gibbsite consists of hexagonal and diamond shaped crystals. The crystal faces have been identified to be {001} basal and {100} and {110} prismatic forming the edges of the crystal. Chamfered faces were also identified in some crystals and these were identified to be {112} and {101}. In the case of diamond shaped crystals, the relative area of the {100} faces is smaller than that of the {110} faces.

Synthetic gibbsite crystals may be precipitated from sodium, lithium or potassium aluminate solutions at temperatures above 50°C. The morphology of these crystals does not depend on the method of preparation, but on the type of alkali aluminate solutions employed. From sodium aluminate solutions, the morphology of gibbsite consisted of agglomerates of hexagonal and diamond shaped crystals with chamfered faces, while single crystals of elongated hexagonal prism were formed from potassium and caesium aluminate, with longer crystals formed from caesium aluminate. From lithium aluminate solution however, the formation of a lithium aluminium hydroxide compound resulted. The morphology of these crystals was that of thin hexagonal plates.

Calculations of defect energies for replacing each of the six distinct hydrogen sites individually with lithium, sodium, potassium and caesium were performed. The results from the isolated defect energy calculations showed that there was a linear relationship between the energy required for the cation substitution with the ionic radius, with lithium being the most favourable. The negative energy of substitution value obtained for lithium incorporation implies that all the lithium will be incorporated in the crystal, as was found experimentally with the formation of lithium aluminium hydroxide species. The degree of cation incorporation was determined experimentally and found to be inversely related to the defect energies.

The experimentally determined morphologies were compared with the predicted morphologies in the absence of cation incorporation. The morphology of the crystals obtained from ageing sodium aluminate matches the predicted equilibrium morphology, suggesting that the crystals with chamfered faces have low sodium incorporation. Sodium analyses on the different gibbsite crystals proved to be difficult due to the low levels of cation incorporated, as well as the mobility of the ion in the electron beam of the scanning electron microscope used for microanalysis.

In the study of metal incorporation, the most stable defect site for sodium was found to be different to that for potassium and caesium, and the adoption of different sites at large defect concentrations is expected to produce different morphologies. To be able to determine quantitatively the effects of different metal ions on gibbsite morphology, calculations on defects at the surface sites and how these affect the incoming gibbsite layers are required.

The addition of certain organic compounds can selectively inhibit the growth of individual gibbsite crystal faces. The importance of adjacent hydroxyl groups and stereochemistry for the poisoning ability of the organic molecule was confirmed. The presence of other functional groups in the organic compounds studied does not affect their selectivity, but can affect the yield. Inhibition of the growth of prismatic faces resulted in the production of elongated hexagonal prisms, while inhibition of growth of the basal face resulted in the formation of hexagonal tablets. A reduction in the

degree of agglomeration was also shown in the presence of some organic compounds, especially those resulting in the formation of elongated crystals. The selective inhibition between the individual prismatic faces, ie. between (100) and (110) was not detected by changes in the morphology; however, selective inhibition was observed in the study of relative growth rates of individual crystal faces. The stereochemical attributes of the organic compounds which determines its selectivity for specific faces have not been identified, and calculations on docking organic compounds on the gibbsite crystal surface should be performed.

The growth rates of individual crystal faces were determined *in situ* and found to vary from crystal to crystal for identical conditions. The question of size dependent growth remains unanswered due the difficulties in producing sufficient numbers of single crystals above 30 μm.

The growth rate of the basal face was found to be a function of the square of supersaturation below a relative supersaturation of 0.81, an indication of a spiral growth mechanism, and a function of supersaturation to the power of $5/6$, indicative of a birth and spread mechanism, above this level. Visually, the formation of nuclei and their subsequent growth were observed above this level of supersaturation. Logarithmic plots for mononuclear and polynuclear birth and spread growth models showed that the growth of gibbsite can be interpreted as following either the mononuclear birth and spread model, or the polynuclear birth and spread model.

Visual observations however, showed the formation of multiple nuclei on the basal face.

The free energy for the formation of a critical nucleus on the crystal surface (basal plane) has been calculated to be 81 kJ/mole, and the edge free energy for a polynuclear process has been calculated to be 6 kJ/mole. A comparison between the growth rates predicted using the free energy for critical nucleus formation in the birth and spread model with the experimental growth rates as a function of relative supersaturation showed a match only for a relative supersaturation of 0.81 (the point at which the data were fitted). When considering spiral growth for the basal face, the activation energy was calculated to also be 81 kJ/mole and the predicted growth rates using this model fitted well with those obtained experimentally. It is however known that the growth mechanism of the basal face above a relative supersaturation of 0.81 is not via spiral growth but birth and spread mechanism (visual observations). A possible explanation for this discrepancy is that in the energy calculation, it is assumed that either the birth and spread or spiral growth is the main mechanism operating at all temperatures. The effect of supersaturation at different constant temperatures also needs to be studied. As mentioned previously, the growth mechanism of the basal face changes from a spiral growth to birth and spread mechanism at a relative supersaturation of 0.81 at 80°C. It is unknown whether this supersaturation threshold is valid for all temperatures. Further experimental work is required to determine the threshold for each temperature before this energy for the basal face can accurately be determined.

The growth rates of the prismatic faces were found to be a function of supersaturation squared, indicative of a spiral growth mechanism. However, above a relative supersaturation of 1.09, it is believed that the barrier for kinetic roughening has been exceeded, resulting in a higher growth rate. It is also possible that at this level the formation of significant levels of a more ordered solution species, which has a more active role in the growth process, has occurred, and hence the definition of relative supersaturation needs to be reconsidered.

A precise definition of supersaturation in Bayer liquors has not yet been satisfactorily defined. Inadequacies in the definition of relative supersaturation may also account for the discrepancy observed for the basal face, where the growth rates dependence on relative supersaturation infers a spiral growth mechanism and the visual observations show a birth and spread mechanism.

The activation energies and kinetic coefficients were also determined for the individual prismatic crystal faces. The activation energies for the prismatic faces are 104 kJ/mole for the (100) face and 99 kJ/mole for the (110) face. This magnitude of activation energy is normally associated with a surface reaction being the overall rate controlling step in the reaction sequence.

The relative growth rates obtained for the effect of supersaturation and those used to determine the activation energies were carried out with a specific experimental regime designed to overcome the problem associated with growth rate dispersion. In the case of the effect of supersaturation, the growth rates were obtained for a liquor at a lower supersaturation before changing it to one with a higher value. The results for reversing the order were shown not to be the same, and this phenomenon should be investigated. Similarly, in the determination of activation energies, relative growth rates were obtained at a constant supersaturation with decreasing temperatures. It is not known if similar results would be obtained with a series of experiments where growth rates of the same single crystal are measured in a sequence of increasing temperatures, with the liquor being changed at each stage to maintain constant supersaturation.

Dynamic light scattering measurements detected and monitored crystal growth as an increase in particle size while particle numbers remained constant, and secondary nucleation as a decrease in average particle size while particle numbers increased. Using this technique, growth rates as a function of supersaturation were determined during the induction time, and were showed to follow the birth and spread model for crystal growth. The growth rates obtained here were ten times less than those obtained in the normal growth regime.

References

References

1. A.C.T.E.D Chemicals in Australia, (1997) http://www.acted.au

2. Armstrong, L. (1993) *Third International Alumina Quality Workshop*, Hunter Valley, NSW Australia, 282 -292

3. Baker, B.R., and Pearson, R.M. (1974) *Journal of Catalysis* **33,** 265

4. Bennema, P. (1994) in Handbook of Crystal Growth, Vol 1, D. T. J Hurle (ed), North Holland, Amsterdam

5. Bird, R. D., Vance, H. R., and Fuhrman, C. (1983) *Light Metals,* 65

6. Bosman, H. J. (1970) *Acta Crystallographica B* **26(5)**, 649

7. Brown, E. R., Headley, A., Geenaway, A. M. and Magnus, K. L. (1986) *Journal Geol. Soc. Jamaica - Proceedings of Bauxite Symposium VI*, 158

8. Brown, N. (1972a) *Journal. Crystal Growth,* **16**, 163

9. Brown, N. (1972b) *Journal. Crystal Growth,* **12**, 39

10. Brown, N. (1975) *Journal of Crystal Growth*, **29**, 309

11. Burton, W. K., Cabrera, N., and Frank, F. C. (1951) *Philosophical Transactions*, **A243**, 299

12. Chaubal, M. V. (1990) *Light Metals,* 85

13. Chernov, A. A. (1990) in *Industrial Crystallization 90*, A. Mersmann (ed) 343

14. Cornell, R. M., Vernon, C. F. and Pannett, D. S. (1996) *Proceedings from Fourth International Alumina Quality Workshop*, June 1996, 97

15. Danilatos, G. D. (1988) *Adv. Elctron. Elctron Phys*, **71**, 109

16. Davey, R. J., and Mullin, J. W. (1976) *Kristall und Technik*, **11**, 229

17. Davey, R. J., Polywka, L. W., and Magini, S. J. (1991) *Advances in Industrial Crystallization*, J. Garside, R.J. Davey and A.G. Jones (eds.), Butterworth-Heinemann, Oxford, 150

18. Debney, D. M., (1993) *Australiasian Mining and Metallurgy - The Sir Maurice Mawby Memorial Volume*. Second Edition, Wookcock, J.T and Hamilton, J.K (Editors), **1**, 758

19. Deer, W.A., Howie, R.A., and Zussman, J. (1977) *An Introduction to Rock Forming Minerals.* Longman Group Ltd, London. 436

20. Dick, B.G., and Overhauser A. W. (1958) *Phys Rev*, **112**, 90

21. Eremin, N.I., Cherepanova, M.I., and Makasakova, M.A. (1980) *Tsevetn Metall.*, **3**, 55

22. Frank, F. C. (1949) *Discussions of the Faraday Society*. **5**, 48

23. Fricke, R. and Jocker, K. (1947) *Z. Naturfursch.* **26**, 244

24. Fricke, R. and Wüllhorst, B. (1932) *Z. Anorg. Allg. Chem.* **205**, 127

25. Friej, S., Reyhani, M. M. and Parkinson, G. M (1997) *9th Internation Conference on Scanning Tunnelling Microscopy*, Hamburg, Germany, July 20-25, 1997

26. Gale, J.D. (1992-5) *General Utility Lattice Program (GULP)* (Royal Institution/Imperial College)

27. Garside J. and Davey, R. J. (1980) *Chemical Engineering Communications*, **4**, 393

28. Garside, J. and Larson, M. A. (1978) *Journal of Crystal Growth,* **43**, 869

29. Gerson, A. R. Counter, J. A. and Cookson, D. J. (1996) *Journal Crystal Growth,* **160**, 346

30. Gibbs, J. W. (1928) *Collected Works*, Longman, New York

31. Gilmer, G.H. and Benemma P. (1972) *Journal of Applied Physics*, **43**, 1347

32. Gindt, R. and Kern, R. (1968) *Besichteder Bunsengellschaft,* **72(3)**, 459

33. Gnyra, B, Jooste, R. F. and Brown, N. (1974) *Journal of Crystal Growth*, **21**, 141

34. Gouma, J. and Bhasin, A. (1993) *Australiasian Mining and Metallurgy - The Sir Maurice Mawby Memorial Volume.* Second Edition, Wookcock, J.T and Hamilton, J.K (Editors), **1**, 763

35. Grant, G.H. and Richards, W.G. (1995) *Computational Chemistry*, Oxford University Press Inc., New York

36. Grocott, S. C. (1988) Bayer Liquor Impurities: *Light Metals*, 833

37. Grocott, S. C. and Rosenberg, S. P. (1988) *Proceedings from First International Alumina Quality Workshop*, September 1988, 271

38. Guthrie, J. D., The, P. J. and Imbrogno, W. D. (1984) *Light Metals*, 127

39. Halfon, A. and Kaliaguine, S. (1976) *Canadian Journal. of Chemical. Engineering,* **54**, 160-167

40. Hartman, P. (1958) *Acta Crystallographica*, **11**, 459

41. Hartman, P. and Perdok, W. G. (1955) *Acta Crystallographica*, **8**, 49

42. Hauschild, U. (1963) *Z. Anorg. Allg. Chem.,* **324**, 15

43. Hillig, W.B. (1966) *Acta Met.,* **14**, 1868

44. Hinde, R. A. and Marantelli, D. M. (1993) *Australiasian Mining and Metallurgy - The Sir Maurice Mawby Memorial Volume.* Second Edition, Wookcock, J.T and Hamilton, J.K (Editors), 1, 756

45. Hirsch, P. B., Howie, A., Nicholson, R.B., Pashley, D.W., and Whelan, M.J. (1971) *Electron Microscopy of Thin Crystals.* Butterworths, London

46. Ilievski, D., Zheng, S. G. and White E. T. (1989) *Chemeca '89*, 1012-1019

47. Jackson, R. A. and Catlow, C. R. A. (1988) *Molec. Simul.*, **1**, 207.

48. King, W. R. (1973) *Light Metals,* 551-562

49. Kossel, W. (1934) *Annalen der Physik*, **21**, 457-480

50. Lawrence, P. J., and Parker, S. C. (1990) Computer Modelling of Oxide Surfaces and Interfaces, in Computer modelling of fluids, polymers and solids. C. R. A, Catlow *et al.,* (eds), Kluwer, Amstredam.

51. Lectard, A. and Nicolas, F. (1983) *Light Metals,* 123-142

52. Lever, G. (1978). *Light Metals*, 71

53. Lippen, B.C. (1961) Thesis, Tech. Univ. Delft

54. Liu, X.Y., Maiwa, K and Tsukamoto, K. (1997) *Journal of Chemical Physics*, **106**, 1870

55. Mackrodt, W. C., Davey, R. J., Black, S. N. and Docherty, R. (1987) *J Crystal Growth*, **80**, 441

56. Madsen, L. H. E. and Boistelle, R. J. (1979) *Journal of Crystal Growth,* **46**, 681

57. McCabe, W. L. (1929) *Industrial and Engineering Chemistry*, **21**, 129

58. McCoy, B. N. and Dewey, J. L. (1982) *Light Metals,* 173

59. Minerals Council of Australia, (1997) http://www.minerals.org.au/

60. Misra, C. and White, E. T. (1971a) *Chemical Engineering Progress Symposium Series*, **67**, *110*, 53

61. Misra, C. and White, E. T. (1971b) *Journal. Crystal Growth,* **8**, 172

62. Moretto, K. E. and Power, G. P. (1990) *Second International Alumina Quality Workshop*, 154-165

63. Mott, N. F. and Littleton, M. J. (1938) *Trans. Faraday Soc.*, **34**, 485

64. Mullin, J. W. (1994) *Crystallization,* Butterworth-Heinemann

65. Newchurch, F. N., Galloway, T. J.and Moretto, K. E., (1993 *Australiasian Mining and Metallurgy - The Sir Maurice Mawby Memorial Volume.* Second Edition, Wookcock, J.T and Hamilton, J.K (Editors), **1**, 768

66. Ni, L. P. and Romanov, L. G. (1975) *Kazakhstan S.S.R. Academy of Sciences Institute of Metals Beneficiation.*

67. Nicoli, D. F. and Elings, V. B. (1988) in *NASA, Lewis Research Center, NASA Laser Light Scattering Advanced Technology Development Workshop*, 153

68. Noyes, A. A. and Whitney, W. P. (1897) *Journal of the American Chemical Society*, **19**, 930-934

69. O'Hara, M. and Reid, R. C. (1973) *Modelling Crystal Growth Rates from Solution*, Prentice-Hall, Englewood Cliffs.

70. Ohkawa, J., Tsuneizumi, T. and Hirao, T. (1985) *Light Metals,* 345

71. Overbey, T. L. and Scott, C. E. (1978) *Light Metals,* 163

72. Papée, D., Tertian, R. and Biais, R. (1958) *Bull. Soc. Chim. Fr.* 1301

73. Parkinson, G. (1996). *Fourth Alumina Quality Workshop*

74. Pearson, T.G. (1955*) The Chemical Background to the Aluminium Industry (Monograph #3)*, Royal Institute of Chemistry, London

75. Popowitz-Biro, R. M., Weissbuch, I., Jacquemain, D., Leveiller, F., Leiserowitz, L. and Lahav, M. (1991) *Advances in Industrial Crystallization* (Symposium Proceedings), J. Garside, R. J. Davey and A. G. Jones (eds), Butterworth-Heinemann, Oxford, 3

76. Power, G. P. (1991) *Extractive Metallurgy Conference*, 1

77. Ristic, R.I., Sheerwood, J.N. and Shripathi, T. (1991) In *Advances in Industrial Crystallization* (Symposium Proceedings), J. Garside, R. J. Davey and A. G. Jones (eds), Butterworth-Heinemann, Oxford, 77

78. Rohl, A. L. and Gay, D. H. (1995) *Mineral Mag.,* **59(397),** 607

79. Rosenberg S.P. and Healy, S.J. (1996) *Proceedings from Fourth International Alumina Quality Workshop*, June 1996, 301

80. Rosenberg, S. P. (1993) Private Communications

81. Rossiter, D.S., Ilievski, D., Smith, P.G. and Parkinson G.M. (1996) *Trans IChemE*, **74(A)** 828

82. Rothbauer, R., Zingan, F. and O'Daniel, H. (1967) *Z. Kristallogr.*, **125**, 317

83. Saalfeld, H. and Jarchow, O. (1968) *Neues. Jahrb. Mineral. Abh.*, **109**, 185

84. Saalfeld, H. and Wedde, M. (1974) *Z. Kristallogr.*, **139(1-2)**, 129

85. Satapathy, B.K. and Vidyasagar, P. (1990) *Light Metals,* 105

86. Sato, C., Yamada, Y., Shibue, Y., Sakamoto, A. and Arakawa, N. (1982*) Light Metals*, 119

87. Schmäh, H. (1946) *Z. Naturforscher.*, 1, 322

88. Sipos, P., Turinek, M. L., Watling, H. R., Toth, I., May, P. M. and Hefner, G. T. (1997) *Annual Symposium on Coordination Chemistry, Kecskemet, Hungary*

89. Skiba, G.R. (1993) *Australiasian Mining and Metallurgy - The Sir Maurice Mawby Memorial Volume.* Second Edition, Wookcock, J.T and Hamilton, J.K (Editors), **1**, 766

90. Smith, P. G. (1994) Private Communications

91. Smith, P.G. and Woods, G. (1993) *Light Metals*, 113

92. The, P.J. (1980) *Light Metals*, 119

93. Thomas, S. and Sherwood, P. M. A. (1992) *Analytical Chemistry*, **64(21)**, 2488

94. Torkar, K. and Bergmann, O., (1960) *Monatsch. Chem.*, **91**, 400

95. Tsukamoto, K (1983) *Journal of Crystal Growth*, **61**, 199

96. Tsukamoto, K (1985) *Journal of Crystal Growth*, **71**, 183

97. Tucker, D. M. Greenaway, A. M. and Douglas C. G. C. (1986) *Journal Geol. Soc. Jamaica - Proceedings of Bauxite Symposium VI*, 145

98. van der Eerden, J.P. (1993) in *Handbook of Crystal Growth*, Vol 1, D. T. J. Hurle (ed) North-Holland, Amsterdam, 307

99. van der Eerden, J.P., Bennema, P. and Cherepanova, T. A. (1978) *Progress in Crystal Growth and Characterization*, **1**, 219

100. van der Heijden A. E. D. M. and van Rosmalen, G. M. (1994) in *Handbook of Crystal Growth*, Vol 2a, D. T. J. Hurle (ed) North-Holland, Amsterdam, 315

101. van Nordstand, R. A., Hettinger, W. P. and Keith, C. D. (1956) *Nature*, **177**, 713

102. Veesler, S. and Boistelle, R. (1993). *Journal. Crystal Growth*, **130**, 411

103. Veesler, S. and Boistelle, R. (1994). *Journal. Crystal Growth*, **142**, 177

104. Warren, H. and Armstrong, L. (1994) *Sixth AusIMM Extractive Metallutgy Conference*, 333

105. Watling, H.R. (1996) *Fourth International Alumina Quality Workshop*, June 1996, 164-171

106. Watts., H.L. and Utley, D.W. (1953) *Analytical Chemistry*, **45**, 2248

107. Watts., H.L. and Utley, D.W. (1956). *Analytical Chemistry*, **25**, 864

108. Wefers, K (1965) *Erzmetall.* 459-463

109. Wefers, K. (1962) *Die Naturwissenschaftern*, 1

110. Wefers, K. and Misra, C. (1987) *Oxides and Hydroxides of Aluminium, Alcoa Technical Paper No. 19, Revised.*

111. White, E.T. and Bateman, S.H. (1988) *Light Metals,* 157

112. Wojcik, M. and Pyzalski, M. (1990) *Light Metals,* 161

113. Wulff, G. (1901) *Z. Krystallogr.*, **34**, 449

Appendix

Appendix

Parts of this thesis have been presented as the following:

M.Lee, P.G. Smith, F.J. Lincoln and G.M. Parkinson, "Characterisation of Gibbsite and Bayerite by Microscopy", IC'94 - Royal Australian Chemical Institute, July, 1994. Poster Presentation

M.Lee, P.G. Smith, F.J. Lincoln, G.M. Parkinson and M.M. Reyhani, "Characterisation of Aluminium Trihydroxide Precipitated from Caustic Solutions", Pacifichem 95, Hawaii, December, 1995. Poster Presentation

M. Lee, G.M. Parkinson, F.J. Lincoln and P.G. Smith, "Microscopic and Macroscopic Observations of Variabilities in The Growth Rates of Gibbsite Crystals" , 1996, 217-226, 4th International Alumina Quality Workshop, Darwin, Australia.

M. Lee, K Tsukamoto, G.M. Parkinson andF.J. Lincoln, "The Application Of Rapid Dynamic Light Scattering To The Study Of The Secondary Nucleation Of Gibbsite", Japan Conference on Crystal Growth 27 (NCCG -27), 1996, Shiaga Prrefecture, Japan

M. Lee, G.M. Parkinson, J.D. Gale, A.L. Rohl, F.J. Lincoln and P.G. Smith, "The Influence of Metal Ion Inclusion on the Morphology of Gibbsite, 1996, Trans IChemE, 739-743

M.Lee, P.G. Smith, F.J. Lincoln, G.M. Parkinson and M.M. Reyhani, "*Characterisation of Aluminium Trihydroxide Precipitated from Caustic Solutions*", in *ACS Symposium Series 667: Separation and Purification by Crystallization*, G. D. Botsaris and K. Toyokura (eds), (1997) 123-133

M. Lee and G.M. Parkinson, "*Growth Rates of Gibbsite Single Crystals Determined Using In Situ Optical Microscopy*", 12th International Conference on Crystal Growth, Jerusalem, Isreal, July 26-31, 1998 Accepted

M. Lee and G.M. Parkinson, "*Mechanisms and Kinetics of Growth of Individual Crystal Faces of Gibbsite*", 5th International Alumina Quality Workshop, Bunbury, Australia. Submitted